POLITECNICO DI TORINO

Department of Electronics and Telecommunications Master's Degree in Electronic Engineering



Master's Degree Thesis

Smart Electromagnetic Skins for communication and localization systems

Supervisors

Prof. Paola Pirinoli Prof. Giuseppe Vecchi

Dott. Michele Beccaria

Candidate Carlotta Sabato

Acknowledgements

First of all, I would like to thank those who made it possible for me to achieve this goal.

I would like to express my heartfelt gratitude to my supervisor, Prof. Paola Pirinoli, for her constant kindness, availability and support since the very beginning.

I am also truly grateful to Dr. Michele Beccaria for his help, patience and valuable advice whenever I needed assistance.

I would like to express my appreciation to Prof. Giusepe Vecchi for his participation as co-supervisor and for his interest in the topic of this thesis.

Finally, I would like to extend my deepest thanks to everyone who has supported me throughout this academic and personal journey. I am truly thankful to my family,my boyfriend, my friends and my colleagues at the Politecnico di Torino, who have stood by me, offering guidance, comfort or simply their presence whenever I needed it most.

Abstract

Smart Electromagnetic Skins (SESs) are emerging as key enabling technologies for the evolution of wireless communication systems toward 5G, 6G, and beyond, where conventional links are strongly affected by high path loss and limited coverage. SESs are thin engineered structures designed to manipulate the propagation of electromagnetic waves, typically by redirecting incident fields through anomalous reflection. They are discretized into a large number of unit cells, whose geometry determines the overall electromagnetic response of the surface. In particular, passive SES, based on resonant metallic patches printed on a dielectric substrate above a ground plane, represent an attractive solution due to their simplicity, low cost, and ease of integration.

This thesis focuses on the design and analysis of a passive SES operating at 60 GHz for indoor communication scenarios. The first part of the work is devoted to the study of the unit cell, based on a square patch geometry, and to the investigation of different dielectric materials used as substrates. A detailed electromagnetic characterization of the unit cell has been carried out through full-wave simulations, analyzing its reflection properties as a function of the geometrical parameters and frequency of operation. This analysis has made possible to compare several dielectric materials and identify the most suitable choice for operation at millimeter-wave frequencies.

Based on the unit cell design, complete SES structures were designed by defining the required phase distribution across the surface to compensate that of the incident field. This procedure allowed defining the arrangement of the unit cells, enabling the realization of a passive SES tailored for operation at 60 GHz in indoor scenarios.

In the final part of the study, multiple SES configurations were designed for a simplified indoor environment. For each SES, the required phase distribution and the corresponding unit cell parameters were determined according to specified angles of incidence and pointing direction. The complete surfaces were then simulated using CST Microwave Studio. The results confirmed that the designed SESs successfully directed the mm-Wave signal toward the shadowed area, demonstrating the effectiveness of the proposed design approach.

Despite its passive and relatively simple configuration, the designed SES proves to be an effective tool for enhancing signal coverage in indoor environments, reducing blind spots and improving communication reliability. These findings highlight the potential of passive SESs as practical and efficient solutions for future wireless networks operating at millimeter-wave frequencies.

Table of Contents

| \mathbf{L}^{i} | st o | f Tables | III |
|---------------------------|------|--|-----|
| ${f L}_{f i}$ | st o | f Figures | IV |
| 1 | Int | roduction | 1 |
| | 1.1 | Smart Electromagnetic Environment | 2 |
| | 1.2 | Introduction to Smart Electromagnetic Skins | 3 |
| | | 1.2.1 Advantages and Disadvantages | 3 |
| | 1.3 | State of art | |
| | 1.4 | Thesis Outline | 9 |
| 2 | Un | it Cell design | 11 |
| | 2.1 | Square Patches | 12 |
| | 2.2 | Substrate Material Selection | 13 |
| | | 2.2.1 Analysis for normal incidence | 15 |
| | | 2.2.2 Analysis for oblique incidence | 19 |
| 3 | Des | sign of Smart Electromagnetic Skins | 27 |
| | 3.1 | Required Phase Distribution | 28 |
| | | 3.1.1 Field on the Reflectarray Elements and Scattered Field | 29 |
| | 3.2 | Mapping the Required Phase to Patch Dimensions | 31 |
| | 3.3 | Full-Wave Simulation and Validation | 32 |
| | | 3.3.1 10x10 SES design | 33 |
| | | 3.3.2 24x24 SES design | |
| | | 3 3 3 Results | 41 |

| 4 | Rea | alistic Indoor Scenario | 44 |
|--------------|------------------|-------------------------------------|----|
| | 4.1 | Reference Scenario | 45 |
| | 4.2 | Modeling and Simulation of the SESs | 48 |
| | | 4.2.1 SES 1 | 49 |
| | | 4.2.2 SES 2 | 52 |
| | | 4.2.3 SES 3 | 55 |
| | | 4.2.4 SES 4 | 59 |
| | | 4.2.5 SES 5 | 62 |
| | | 4.2.6 SES 6 | 65 |
| | | 4.2.7 SES 7 | 68 |
| | | 4.2.8 SES 8 | 71 |
| | 4.3 | Frequency Response of SESs | 74 |
| | 4.4 | Conclusions of the SESs Analysis | 79 |
| 5 | Coı | nclusions | 80 |
| ${f A}$ | \mathbf{M}^{A} | ATLAB Code for SES Design | 82 |
| В | Ge | neration of DXF file | 87 |
| | B.1 | Function dxfRectangle | 88 |
| | B.2 | Function dxfHeader | 90 |
| | В.3 | Function dxfClose | 91 |
| \mathbf{B} | iblio | ography | 92 |

List of Tables

| 2.2.1 Comparison between FR4 and Rogers RO3003 substrates | 13 |
|--|----|
| 4.1.1 Angles of arrival and departure (azimuth, elevation) the configuration | |
| SESs | 47 |

List of Figures

| 1.0.1 | Smart Electromagnetic Environment [1] | 2 |
|--------|--|----|
| 1.3.1 | System architecture [14] | 6 |
| 1.3.2 | Layout of the periodic structure [16] | 7 |
| 1.3.3 | Layout of the dual-layer SES [18] | 8 |
| 2.0.1 | Infinite array | 12 |
| 2.2.1 | Unit cell using a square patch | 14 |
| 2.2.2 | 2.2.2 Phase response of the unit cell under normal incidence at 58 | |
| | GHz for different substrate thicknesses | 15 |
| 2.2.3 | Phase response of the unit cell under normal incidence at 60 | |
| | GHz for different substrate thicknesses | 16 |
| 2.2.4 | Phase response of the unit cell under normal incidence at 62 | |
| | GHz for different substrate thicknesses | 16 |
| 2.2.5 | Magnitude of the reflection coefficient of the unit cell under | |
| | normal incidence at $58~\mathrm{GHz}$ for different substrate thicknesses. | 17 |
| 2.2.6 | Magnitude of the reflection coefficient of the unit cell under | |
| | normal incidence at 60 GHz for different substrate thicknesses. | 17 |
| 2.2.7 | Magnitude of the reflection coefficient of the unit cell under | |
| | normal incidence at $62~\mathrm{GHz}$ for different substrate thicknesses. | 18 |
| 2.2.8 | Phase response of the unit cell under oblique incidence at | |
| | 58 GHz for 0.51mm substrate thicknesses | 20 |
| 2.2.9 | Phase response of the unit cell under oblique incidence at | |
| | 60 GHz for 0.51mm substrate thicknesses | 20 |
| 2.2.10 | OPhase response of the unit cell under oblique incidence at | |
| | 62 GHz for 0.51mm substrate thicknesses | 21 |

| 2.2.11 | 1 Magnitude of the reflection coefficient of the unit cell under | |
|--------|--|----|
| | oblique incidence at 58 GHz for $0.51\mathrm{mm}$ substrate thicknesses. | 21 |
| 2.2.12 | 2Magnitude of the reflection coefficient of the unit cell under | |
| | oblique incidence at 60 GHz for $0.51\mathrm{mm}$ substrate thicknesses. | 22 |
| 2.2.13 | 3Magnitude of the reflection coefficient of the unit cell under | |
| | oblique incidence at 62 GHz for $0.51\mathrm{mm}$ substrate thicknesses. | 22 |
| 2.2.14 | 4Phase response of the unit cell under oblique incidence at | |
| | 58 GHz for 0.76mm substrate thicknesses | 23 |
| 2.2.15 | 5Phase response of the unit cell under oblique incidence at | |
| | 60 GHz for 0.76mm substrate thicknesses | 23 |
| 2.2.16 | 3Phase response of the unit cell under oblique incidence at | |
| | 62 GHz for 0.76mm substrate thicknesses | 24 |
| 2.2.17 | 7Magnitude of the reflection coefficient of the unit cell under | |
| | oblique incidence at 58 GHz for 0.76mm substrate thicknesses. | 24 |
| 2.2.18 | 8Magnitude of the reflection coefficient of the unit cell under | |
| | oblique incidence at 60 GHz for $0.76\mathrm{mm}$ substrate thicknesses. | 25 |
| 2.2.19 | Magnitude of the reflection coefficient of the unit cell under | |
| | oblique incidence at 62 GHz for $0.76\mathrm{mm}$ substrate thicknesses. | 25 |
| 3.1.1 | Coordinate system used for the analysis of the required | |
| | phase distribution [27] | 28 |
| 3.3.1 | Phase curve used for the design | 34 |
| 3.3.2 | Required phase distribution | 34 |
| 3.3.3 | Patch width distribution | 35 |
| 3.3.4 | SES layout 10x10 | 35 |
| 3.3.5 | 3D far-field pattern at 60 GHz for the 10×10 SES | 36 |
| 3.3.6 | Phase curve used for the design | 37 |
| 3.3.7 | Required phase distribution | 38 |
| 3.3.8 | Patch width distribution | 38 |
| 3.3.9 | SES layout 24x24 | 39 |

| 3.3.10Farfield results at 58 GHz: Cartesian cut (left) and | 3D pat- |
|---|---------------|
| tern (right) | 39 |
| 3.3.11Farfield results at 58.5 GHz: Cartesian cut (left) | and 3D |
| pattern (right) | 39 |
| $3.3.12 \mathrm{Farfield}$ results at 59 GHz: Cartesian cut (left) and | 3D pat- |
| tern (right) | 40 |
| 3.3.13Farfield results at 59.5 GHz: Cartesian cut (left) | and 3D |
| pattern (right) | 40 |
| $3.3.14 \mathrm{Farfield}$ results at 60 GHz: Cartesian cut (left) and | 3D pat- |
| tern (right) | 40 |
| 3.3.15Farfield results at 60.5 GHz: Cartesian cut (left) | and 3D |
| pattern (right) | 40 |
| $3.3.16 Farfield \ results$ at 61 GHz: Cartesian cut (left) and | 3D pat- |
| tern (right) | 4 |
| 3.3.17Farfield results at 61.5 GHz: Cartesian cut (left) | and 3D |
| pattern (right) | 42 |
| $3.3.18 \mathrm{Farfield}$ results at 62 GHz: Cartesian cut (left) and | 3D pat- |
| tern (right) | 4 |
| $3.3.19 \mathrm{Comparison}$ of the reflected field patterns at $58 \mathrm{GHz}$ | :,59GHz, |
| 60GHz, 61GHz and 62GHz. The curves confirm to | hat side |
| lobes increase in magnitude and number as frequ | ency in- |
| creases, with almost comparable levels observed at | 62GHz . 42 |
| 4.1.1 Realistic indoor environment with multiple SESs . | 45 |
| 4.1.2 "W" SESs Configuration | 46 |
| 4.1.3 Spillover power for the "W" SESs configuration | 47 |
| 4.1.4 Angle Convention used for the Azimuth and Elevat | ion angles 48 |
| 4.2.1 Phase curve used for the SES 1 design | 49 |
| 4.2.2 SES 1 Required phase distribution | 50 |
| 4.2.3 SES 1 Patch width distribution | |
| 4.2.4 SES 1 layout | |

| 4.2.5 3D far-field radiation pattern (left) and RCS map (right) of |
|---|
| SES1 |
| 4.2.6 2D RCS cuts of SES 1 far-field response |
| 4.2.7 Phase curve used for the SES 2 design |
| 4.2.8 SES 2 Required phase distribution |
| 4.2.9 SES 2 Patch width distribution |
| 4.2.10SES 2 layout |
| 4.2.113D far-field radiation pattern (left) and RCS map (right) of |
| SES2 |
| 4.2.122D RCS cuts of SES 2 far-field response |
| 4.2.13Phase curve used for the SES 3 design |
| 4.2.14SES 3 Required phase distribution |
| 4.2.15SES 3 Patch width distribution |
| 4.2.16SES 3 layout |
| $4.2.173\mathrm{D}$ far-field radiation pattern (left) and RCS map (right) of |
| SES3 |
| 4.2.182D RCS cuts of SES 3 far-field response |
| 4.2.19Phase curve used for the SES 4 design |
| 4.2.20SES 4 Required phase distribution |
| 4.2.21SES 4 Patch width distribution |
| 4.2.22SES 4 layout |
| 4.2.233D far-field radiation pattern (left) and RCS map (right) of |
| SES4 |
| 4.2.242D RCS cuts of SES 4 far-field response |
| 4.2.25Phase curve used for the SES 5 design |
| 4.2.26SES 5 Required phase distribution |
| 4.2.27SES 5 Patch width distribution |
| 4.2.28SES 5 layout |
| 4.2.293D far-field radiation pattern (left) and RCS map (right) of |
| SES5 |

| 4.2.302D RCS cuts of SES 5 far-field response |
|--|
| 4.2.31Phase curve used for the SES 6 design |
| 4.2.32SES 6 Required phase distribution |
| 4.2.33SES 6 Patch width distribution |
| 4.2.34SES 6 layout |
| 4.2.353D far-field radiation pattern (left) and RCS map (right) of |
| SES6 |
| 4.2.362D RCS cuts of SES 6 far-field response |
| 4.2.37Phase curve used for the SES 7 design |
| 4.2.38SES 7 Required phase distribution |
| 4.2.39SES 7 Patch width distribution |
| 4.2.40SES 7 layout |
| 4.2.413D far-field radiation pattern (left) and RCS map (right) of |
| SES7 |
| 4.2.422D RCS cuts of SES 7 far-field response |
| 4.2.43Phase curve used for the SES 8 design |
| 4.2.44SES 8 Required phase distribution |
| 4.2.45SES 8 Patch width distribution |
| 4.2.46SES 8 layout |
| 4.2.473D far-field radiation pattern (left) and RCS map (right) of |
| SES8 |
| 4.2.482D RCS cuts of SES 8 far-field response |
| 4.3.1 RCS cut of SES1 for multiple frequencies around the design |
| value of 60GHz |
| 4.3.2 RCS cut of SES2 for multiple frequencies around the design |
| value of 60GHz |
| 4.3.3 RCS cut of SES3 for multiple frequencies around the design |
| value of 60GHz |
| 4.3.4 RCS cut of SES4 for multiple frequencies around the design |
| value of 60GHz |

| 4.3.5 | RCS cut of SES5 for multiple frequencies around the design | |
|-------|--|----|
| | value of 60GHz | 77 |
| 4.3.6 | RCS cut of SES6 for multiple frequencies around the design | |
| | value of 60GHz | 77 |
| 4.3.7 | RCS cut of SES7 for multiple frequencies around the design | |
| | value of 60GHz | 78 |
| 4.3.8 | RCS cut of SES8 for multiple frequencies around the design | |
| | value of 60GHz | 78 |

Chapter 1

Introduction

The use of millimeter-wave(mmWave) frequency bands, such as 28,29 and 100GHz, is considered one of the key enabling technologies for fifth-generation (5G) mobile networks, as well as for future generations beyond 5G and 6G.

The wider bandwidth available in the mmWave spectrum allows for higher data rates and lower latency compared to previous generations operating at sub-6GHz frequencies.

However, mmWave propagation is characterized by higher path loss and greater penetration losses, making the signals more susceptible to blockage by physical obstacles. Elements such as buildings, walls, furniture, or glass panels, depending on whether the environment is outdoor or indoor, can create coverage gaps known as blind zones.

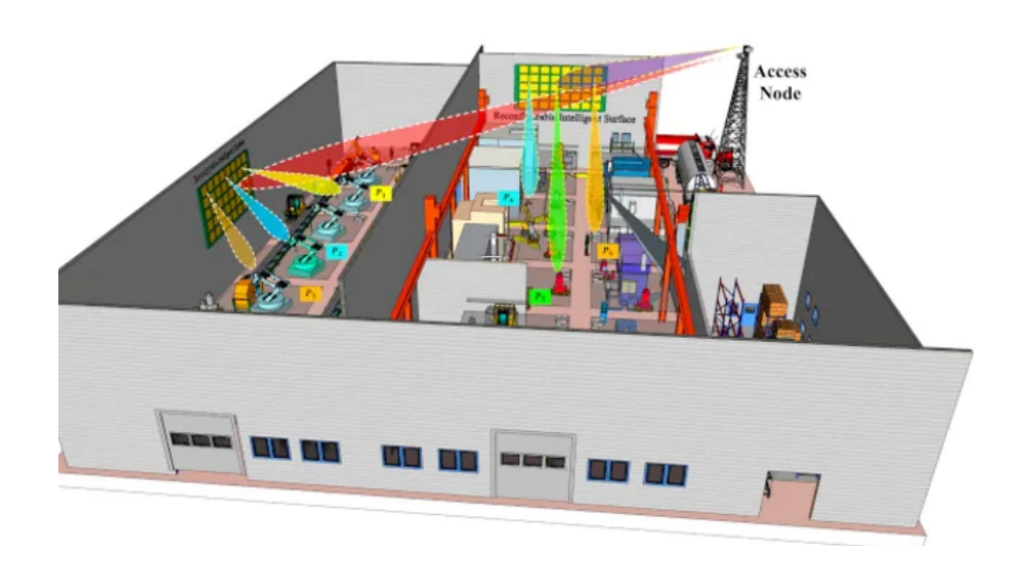


Figure 1.0.1: Smart Electromagnetic Environment [1]

1.1 Smart Electromagnetic Environment

To mitigate the coverage limitations of mmWave communications, the simplest solution would be to increase the number of base stations (BSs). While effective, this strategy inevitably leads to higher deployment costs, greater power consumption and an overall rise in electromagnetic field (EMF) exposure. An alternative and more sustainable approach is offered by the concept of the Smart Electromagnetic Environment (SEE). This perspective shifts the role of the environment from being merely a passive element, alongside base stations and mobile devices, to becoming an active resource that introduces a new degree of freedom (DoF) for enhancing network performance and improving overall Quality of Service (QoS) [2], where information is transmitted not by generating new signals but by intelligently reusing existing ones whenever possible.[3]. In this approach, the traditional network of mmWave BSs is supported by a mix of complementary technologies, including Integrated Access and Backhaul (IAB) nodes, smart repeaters, Reconfigurable Intelligent Surfaces (RISs), and passive Smart Electromagnetic Skins (SESs).[4]

1.2 Introduction to Smart Electromagnetic Skins

SESs have emerged as versatile solution to address critical challenges in next-generation SEE scenarios. Their exceptional capability for wave manipulation is achieved through the precise control of local electromagnetic properties, enabled by tailored design of their structure([5],[4],[6]).

Two main approaches can be adopted for their implementation. The first consists of completely passive (static) surfaces, designed to redirect the incident field toward a fixed direction or to provide a predefined coverage pattern. The second involves reconfigurable (dynamic) configurations, generally referred to as reconfigurable intelligent surfaces, in which the beam shape or direction can be modified in real time by adjusting the surface's electromagnetic response through the integration of tunable elements. Depending on the design they can:

- Redirect an incoming signal toward a desired direction (beam steering);
- Focus the energy in a specific area (beam focusing);
- Modify polarization to match the receiving system;
- Scatter or suppress unwanted interference.
- Improve the QoS of the network

1.2.1 Advantages and Disadvantages

In short, SESs are artificially engineered surfaces, consisting of periodic/aperiodic arrangements of specifically designed resonant size ($\approx \frac{\lambda}{2}$) or sub-wavelength ($\approx \frac{\lambda}{10}$) unit cells(UCs).

In case in which resonant size UCs are used, SES are comparable to reflectarrays, and the procedure adopted for their design is essentially the same.

These features make them a more advantageous solution compared to increasing the number of BS. Key advantages includes:

- Cost efficiency: manufacturing and deployment costs are significantly lower compared to active network infrastructure since they are in most of the case made of a Printed Circuit Board(PCB)
- Scalability: SESs can be installed incrementally as coverage needs evolve.
- Aesthetic integration: flat, lightweight panels can be seamlessly integrated into building surfaces.
- Energy efficiency: passive or semi-passive operation greatly reduces power requirements.

On the other hand RISs have attracted significant attention due to their reconfigurability, enabled by tunable components such as varactor diodes [7], liquid crystals [8], graphene [9], or p-i-n diode switches [10]. Compared to their simpler static counterparts, RISs present some limitations. In particular, each unit cell typically has a

finite number of discrete states (e.g., 2^N for an N-bit design), which can reduce beamforming performance and generate unwanted spurious beams. While increasing the number of states by adding more diodes or interfacing varactors with DAC(digital to analog converter) can improve performance, it also leads to higher power consumption and more complex, costly control networks. Additionally, the increased architectural complexity makes RISs more sensitive to manufacturing tolerances and the non ideal behavior of embedded tunable loads, potentially causing significant deviations from their nominal or simulated performance. [11]

1.3 State of art

In recent years, significant research has been devoted to understanding how RISs and SESs can be effectively deployed in realistic environments, both indoor and outdoor. For outdoor applications, the main challenge lies in integrating these surfaces into complex urban settings, where buildings, streets, and other obstacles create multiple reflections and propagation paths that need to be managed.

Early implementations of SESs and RISs typically considered them as flat panels mounted on building facades. While this configuration is relatively straightforward for indoor scenarios, it becomes more complex outdoors due to constraints such as architectural regulations, historical preservation, window placement, or misalignment between buildings and base stations.

In [12] the authors address The optimal planning of electromagnetic skins installed on the building facades to enhance the received signal strength, and thus the wireless coverage and the QoS in large-scale urban areas, is addressed. More specifically, a novel instance of the System-by-Design (SbD) paradigm is proposed toward the implementation of a SEE where low-cost passive static reflective skins are deployed to enhance the level of the power received within selected Regions of Interest (RoIs). Thanks to the ad hoc customization of the SbD functional blocks, which includes the exploitation of a Digital Twin (DT) for the accurate yet fast assessment of the wireless coverage condition, effective solutions are yielded. Numerical results, dealing with real-world test beds, are shown to assess the capabilities, the potentialities, and the current limi-

tations of the proposed SES planning strategy.

In [13], the authors explored a purely passive solution to enable beam scanning without relying on active components. Their innovative SES design allows the reflected beam direction to be steered simply by mechanically rotating the surface around its supporting pole. This approach demonstrates the feasibility of low-complexity implementations but remains limited in terms of flexibility and dynamic adaptability.

A more advanced solution was presented in [14], where a reflect-array of 224 reconfigurable patches was designed for 60 GHz Wi-Fi signals. Each patch is equipped with electronically controlled relay switches, which can be turned on or off depending on the switch state. The system architecture is shown in Fig. 1.3.1.

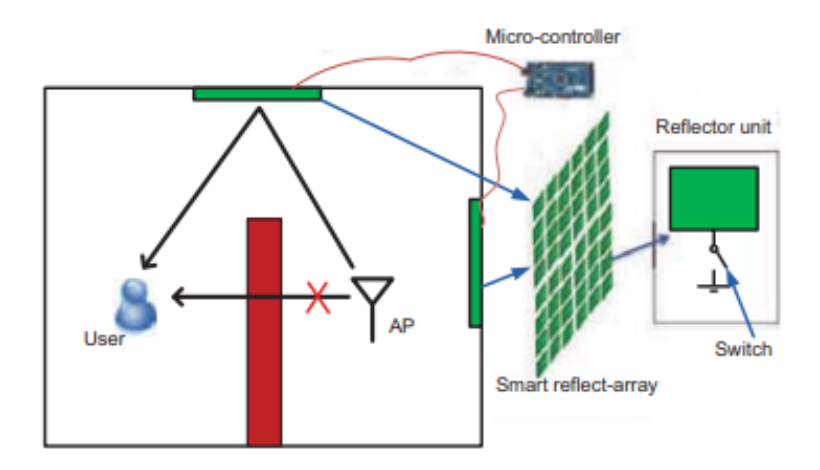


Figure 1.3.1: System architecture [14]

To operate the array, the authors proposed a beam-searching algorithm in which the Access Point (AP) and the reflectarray cooperate to identify the beam direction that maximizes the signal quality at the user side. The main drawback of this implementation lies in the hardware: only two phase states (binary control) are supported, which inevitably reduces the achievable signal-to-noise ratio (SNR). [15]

A different approach is found in [16], where the SES design relies on the well-known Intersection Approach for near-field beam shaping. This is particularly important because, in the considered scenario, users are located within the Fresnel region of the SES rather than in the far-field. The design goal is to generate a prescribed shaped beam in the near-field area, supporting two orthogonal linear polarizations. To this

end, the synthesis results are implemented in a reflective SES composed of coplanar dipole elements (Fig. 1.3.2), which enable independent control of both polarizations using only a single dielectric layer.

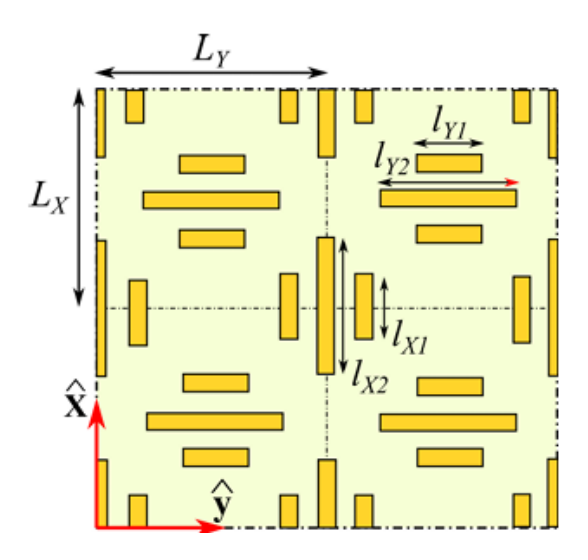


Figure 1.3.2: Layout of the periodic structure [16]

In the last few years, significant progress has been made toward the development of optically-transparent and modular SES. In [17] the authors proposed a high-resolution fabrication procedure that allows precise control of the electromagnetic properties while maintaining optical transparency. The modular design enables flexible integration in various scenarios, making these SES adaptable to different wireless communication environments. This work demonstrates the potential of combining transparency, modularity, and high electromagnetic performance in next-generation SES devices.

Recent studies have reported the first large-scale indoor validation of the SES concept, using static-passive panels to enhance coverage in 5GHz Wi-Fi networks [18]. The SES were installed on walls respecting architectural constraints, with the goal of capturing maximum energy from the access point and directing it towards the RoI.

The panels consisted of dual-layer unit cells, as shown in Fig.1.3.3 with metallic patches on FR-4 PCBs, designed to achieve a smooth, controllable reflection phase. Both simulations and experiments showed a significant improvement in coverage: the average received power increased by approximately 2.6dB, with peaks up to 9.6dB. Intermediate-sized SES provided the best trade-off between performance and architectural limitations, reducing the uncovered RoI area by up to 70%. The resulting electromagnetic

field distribution confirmed the SES's ability to form a controlled directive beam, improving propagation in complex indoor environments.

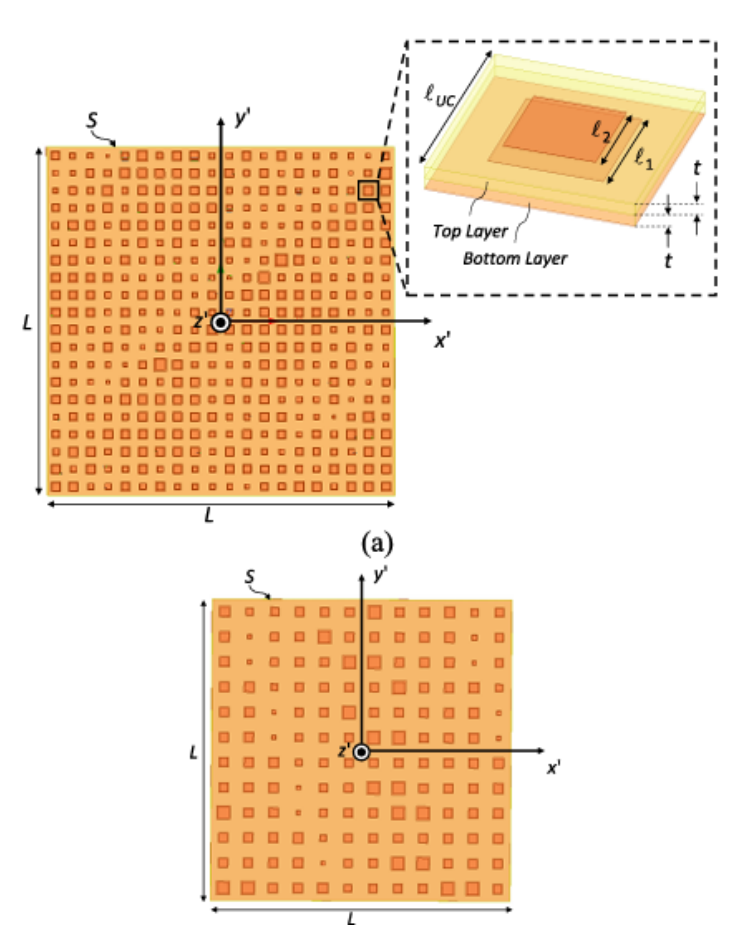


Figure 1.3.3: Layout of the dual-layer SES [18]

Building on the concept of static-passive SES for indoor coverage, Oliveri et al. [19] investigated the potential of static passive electromagnetic skins for NLOS specular wireless links. They derived analytical expressions for the total path attenuation and showed that, under proper design conditions, SESs can outperform conventional metallic reflectors of the same aperture by modifying the phase response of the reflected field. Their simulations highlight the dependence of link performance on panel size, incidence angle, and reflection geometry, demonstrating that SESs can provide significant gains in NLOS scenarios without requiring any active control or power supply. This study confirms the potential of passive EM skins as efficient solutions for enhancing wireless coverage in more complex propagation environments.

In addition to improving coverage and link quality, smart electromagnetic skins are

increasingly being investigated for their potential in Integrated Sensing and Communication (ISAC) systems. In this context, SES can serve not only as passive reflectors for communication signals but also as tools for passive localization of users or objects, exploiting the modifications they induce on the propagation environment. In particular, the recent work [20] demonstrates that smart surfaces can be leveraged to localize mobile users without relying on traditional power-hungry methods such as GPS or deploying additional infrastructure. By exploiting the controlled reflective properties of the surface elements, this approach enables opportunistic passive localization, accurately estimating user positions through trained learning models applied to the signal reflections induced by smart electromagnetic surfaces. Extensive simulations and experimental results report positioning errors as low as 5% relative to the field size, while even a low-complexity implementation on a limited embedded system achieves errors in the 11% range with minimal energy overhead (+2.7% compared to a classical RIS). This approach highlights the dual functionality of smart surfaces: they can improve wireless coverage while simultaneously providing sensing and localization capabilities, representing a crucial step toward practical ISAC-enabled smart environments.

1.4 Thesis Outline

The aim of this thesis is to investigate the use of smart electromagnetic skins for enhancing communication and localization performance at millimeter-wave frequencies, with particular focus on the 60 GHz band. Applications operating at 60 GHz are used to achieve ultra-high-speed and high-capacity wireless connectivity, especially in dense environments or for short-range links. The 60 GHz band provides a much larger bandwidth compared to traditional frequencies, but with a more limited range due to atmospheric absorption, and typically requires a direct LoS connection.

The work combines both design and simulation activities to evaluate how passive engineered surfaces can be employed to reshape the propagation environment and mitigate coverage issues in indoor scenarios.

The study is organized into four main parts:

- Chapter 1 introduces the concept of smart electromagnetic skins, reviewing their operating principles and surveying the most relevant state-of-the-art works.
- Chapter 2 focuses on the design and electromagnetic characterization of the unit cell, including the selection of a suitable dielectric substrate and the analysis of its impact on the reflection properties.
- Chapter 3 describes the design of the complete SES surface, detailing the procedure to map the desired phase distribution onto the array and to determine the corresponding patch dimensions.
- Chapter 4 presents the design of an indoor environment where multiple SESs are deployed to overcome a coverage gap caused by the presence of a separating wall between two rooms. The study evaluates how the controlled reflection and redirection of the mm-Wave signals can extend coverage into blind regions.
- Chapter 5 presents a summary of the key results of the thesis and highlights possible avenues for future research in the area of smart electromagnetic skins.

Chapter 2

Unit Cell design

The focus of this work is on the design of passive smart electromagnetic skins based on resonant unit cells. A SES can be regarded as a planar structure composed of a quasi periodic array of radiating elements such as metallic patches, which are designed to provide a specific phase response. By properly tailoring the phase distribution across the array, the reflected wavefront can be controlled to form a focused beam in a desired, non specular, directions when illuminated by the field radiated an external source. The simplest solution consist in realizing the smart skin with a single layer PCB. The dielectric material plays a crucial role since its electromagnetic properties, in particular the relative permittivity, the loss tangent and the thickness [23], directly affect the resonance behaviour of the patches and consequently the overall design and performance of the SES.

The design process begins with the characterization of the single SES elements, whose reflection phase and amplitude responses must be carefully studied [24]. Once the unit cell have been characterized, the elements can be combined into an array with the desired aperture size and phase distribution, ultimately enabling the realization of the entire SES. The characterization of the unit cell requires extracting the so-called S-curve, which relates the phase of the reflection coefficient to the variation of the UC physical parameters, under either orthogonal or oblique plane-wave illumination. A common and effective approach for this purpose is the adoption of the infinite array model based on Floquet's theorem. This method allows the analysis to be restricted to a single UC, periodically replicated to form an infinite array. The approximation

provides a reliable estimation of the actual electromagnetic response of the structure, since it inherently accounts for the mutual coupling between adjacent elements.

In practice, Floquet theory is implemented in full-wave electromagnetic solvers such as CST Studio Suite by means of Floquet ports and periodic boundary conditions.

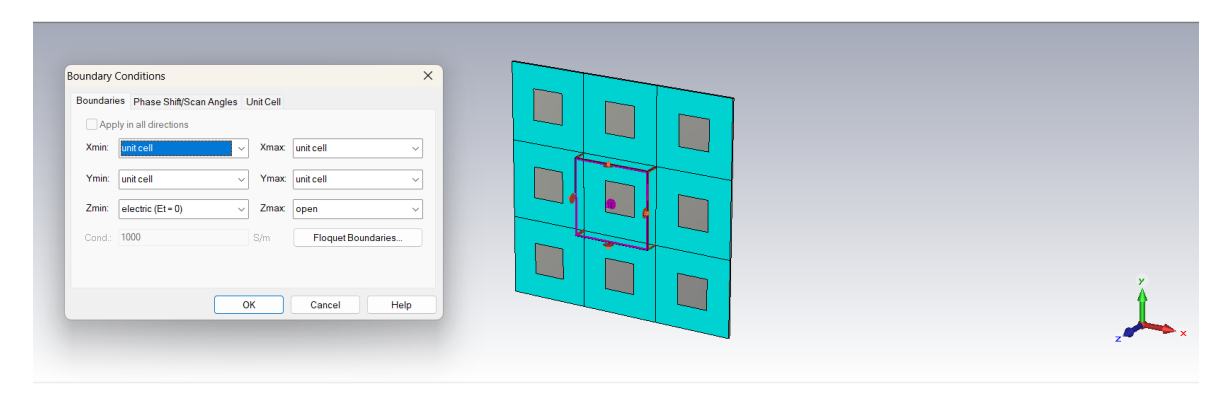


Figure 2.0.1: Infinite array

2.1 Square Patches

A simplest solution for the UC consists in employing patch elements and controlling the unit cell behaviour varying one of more of its geometrical parameters. Among the different geometries, the square configuration is particularly suitable, since by properly tuning its side length it is possible to control the phase delay of the reflected wave. In theory, a single resonance would allow the entire 360° phase cycle to be covered. In practice, however, the maximum achievable phase range is more limited due to several

constraints, such as the finite separation between adjacent cells, the thickness of the

dielectric substrate, and the intrinsic properties of the material.

The relationship between the patch size and the induced phase shift is highly non-linear: a steep variation occurs in the vicinity of the resonant dimension, whereas a much smoother dependence is observed at the edges of the design range. This peculiar behaviour gives rise to the characteristic phase—size response curve, often referred to as the S-curve, which clearly highlights the transition between the slow and fast variation regions. This curve is a fundamental design tool, since it provides the mapping between the physical geometry of the resonant element and the electromagnetic phase response, and it is later exploited in the synthesis of the entire surface to impose the desired

phase distribution.

2.2 Substrate Material Selection

As already mentioned, the dielectric substrate is a key component in the SESs design, as its electrical and physical properties directly influences the behaviour of the resonant unit cells.

Among the possible substrate, low cost materials such as FR4 are not suitable for mmWave applications due to their high losses and poor dielectric stability. For this reason in this work the adopted materials is Rogers RO3003, a laminate specifically used for high frequencies applications that guaranteed a good stability of the dielectric constant over a various range of temperatures and frequencies [25], as demonstrated, for example, in recent designs of mmWave antennas on RO3003 [26].

Table 2.2.1: Comparison between FR4 and Rogers RO3003 substrates

| Property | FR4 | Rogers RO3003 |
|--|--------------------|--------------------------------------|
| Dielectric constant ϵ_r | 4.2–4.8 (variable) | 3.0 (stable) |
| Dissipation factor $\tan \delta$ @10 GHz | 0.02-0.025 | 0.0010 |
| Losses at mmWave frequencies | High | Very low |
| Thickness availability | Standard PCB sizes | Multiple options (e.g. 0.13–1.52 mm) |
| Suitability for mmWave | Poor | Excellent |

According to the manufacturer datasheet, the Rogers RO3003 laminate is available in a set of standard thicknesses, namely:

- 0.005'' (0.13 mm) $\pm 0.0005''$
- 0.010'' (0.25 mm) $\pm 0.0007''$
- 0.020'' (0.51 mm) $\pm 0.0010''$
- 0.030'' (0.76 mm) $\pm 0.0015''$
- 0.060'' (1.52 mm) $\pm 0.0030''$

The first step of the UC characterization therefore has consisted in its analysis considering these thickness values, so as to evaluate the effect of the substrate height on the resonance behaviour and the corresponding reflection phase response.

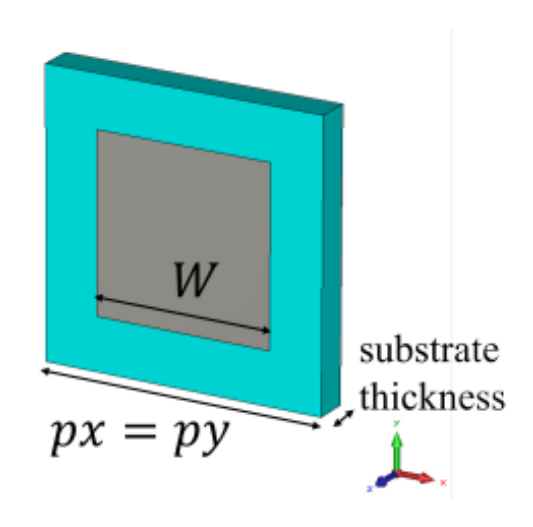


Figure 2.2.1: Unit cell using a square patch

The main parameters adopted in the simulations are summarized below.

Parameters used for the characterization

• Design Frequencies: 58GHz, 60GHz, 62GHz

• Unit Cell size: $\approx \frac{\lambda}{2} @ f_0 = 60 GHz$

Substrate Properties

• Dielectric constant: $\epsilon_r = 3$

• Dissipation factor: $tan\delta = 0.0010$

• Thickness: Variable

Patch Properties

• Patch width W: Variable

• Metal thickness: 0mm (PEC)

2.2.1 Analysis for normal incidence

In the first stage of the analysis, the standard substrate thicknesses of Rogers RO3003 were investigated, with the exception of the $1.52\,\mathrm{mm}$ laminate, which was not considered due to its excessive thickness. For each of the selected thicknesses, the reflection coefficient was extracted in terms of both magnitude and phase in order to study how the unit cell response varies as a function of the patch width W. The analysis was performed at 58, 60, and $62~\mathrm{GHz}$, assuming normal incidence of the plane wave, while the patch width W was swept from $0.2\,\mathrm{mm}$ to $2.4\,\mathrm{mm}$ to obtain the characteristic phase and magnitude curves of the unit cell.

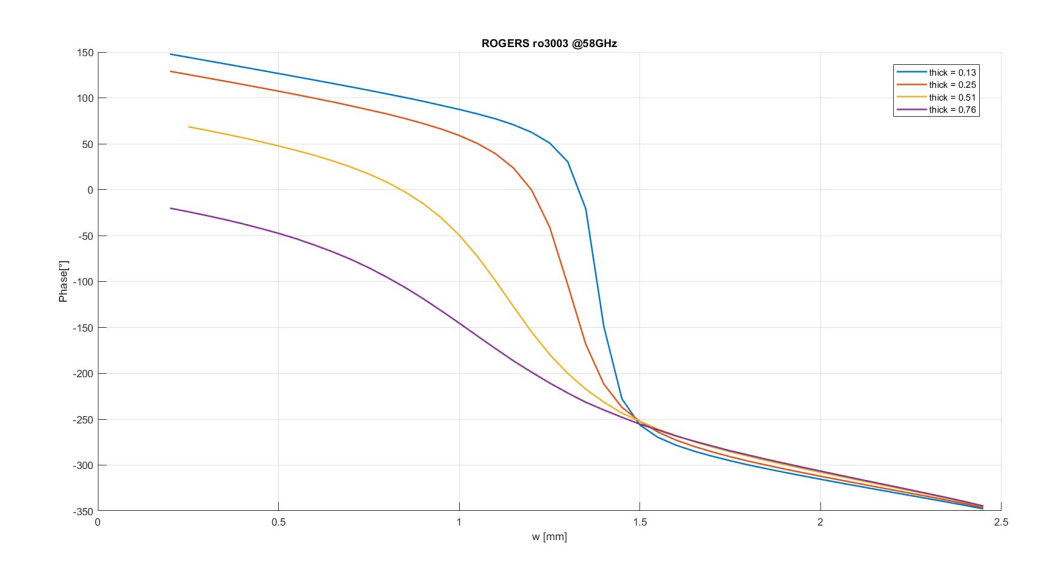


Figure 2.2.2: Phase response of the unit cell under normal incidence at 58 GHz for different substrate thicknesses.

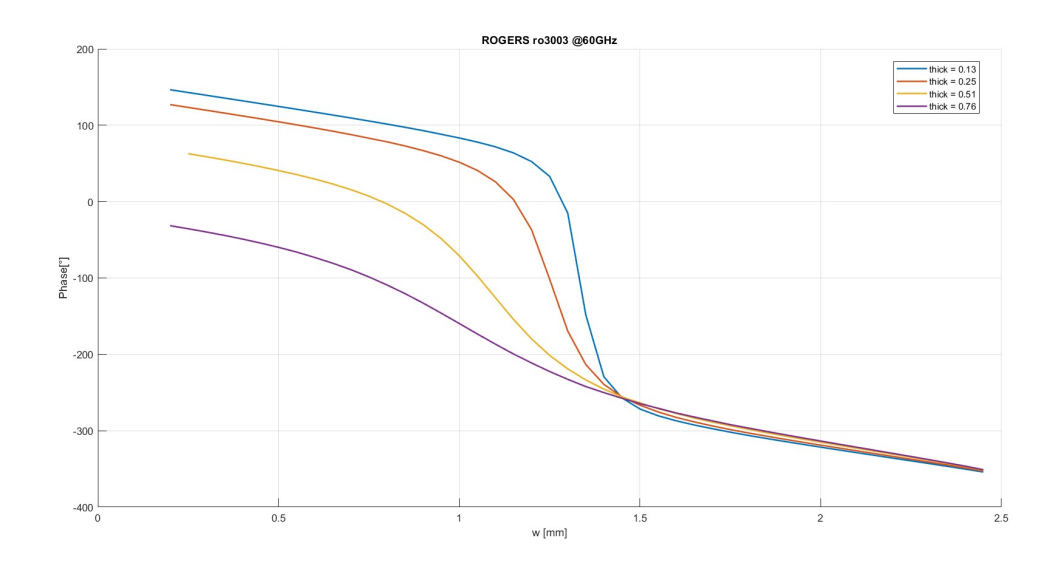


Figure 2.2.3: Phase response of the unit cell under normal incidence at 60 GHz for different substrate thicknesses.

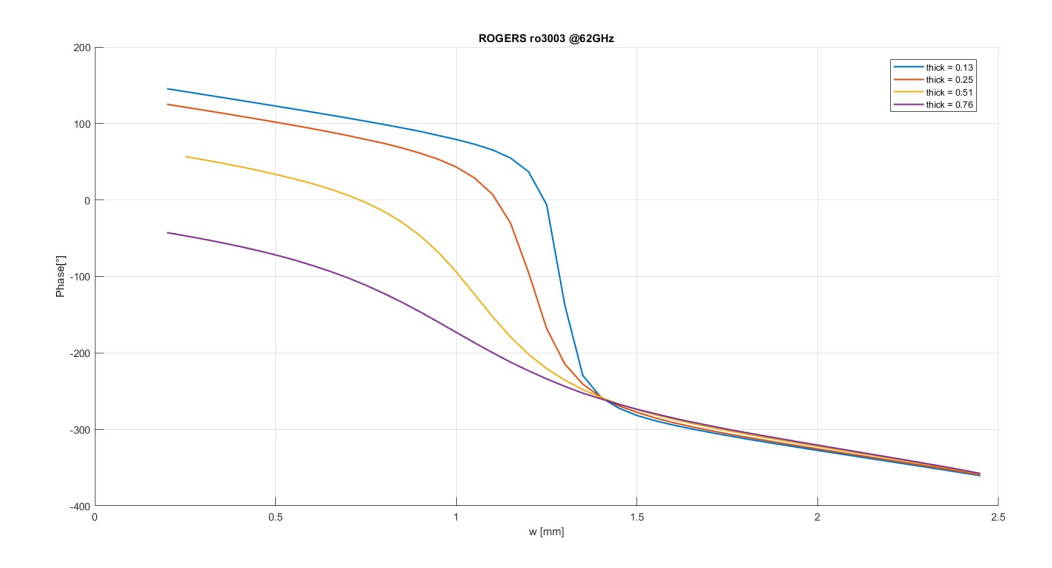


Figure 2.2.4: Phase response of the unit cell under normal incidence at 62 GHz for different substrate thicknesses.

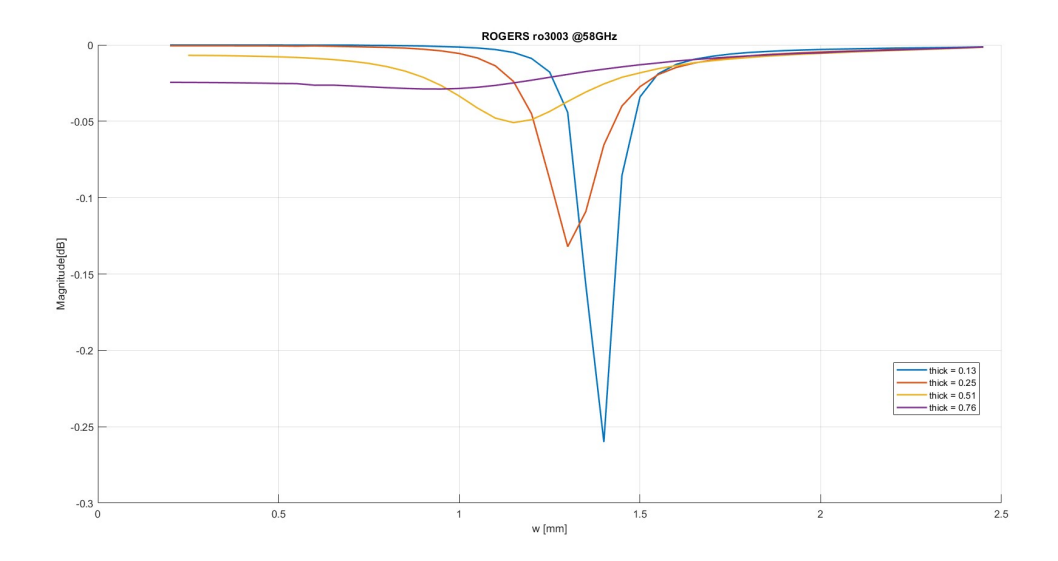


Figure 2.2.5: Magnitude of the reflection coefficient of the unit cell under normal incidence at 58 GHz for different substrate thicknesses.

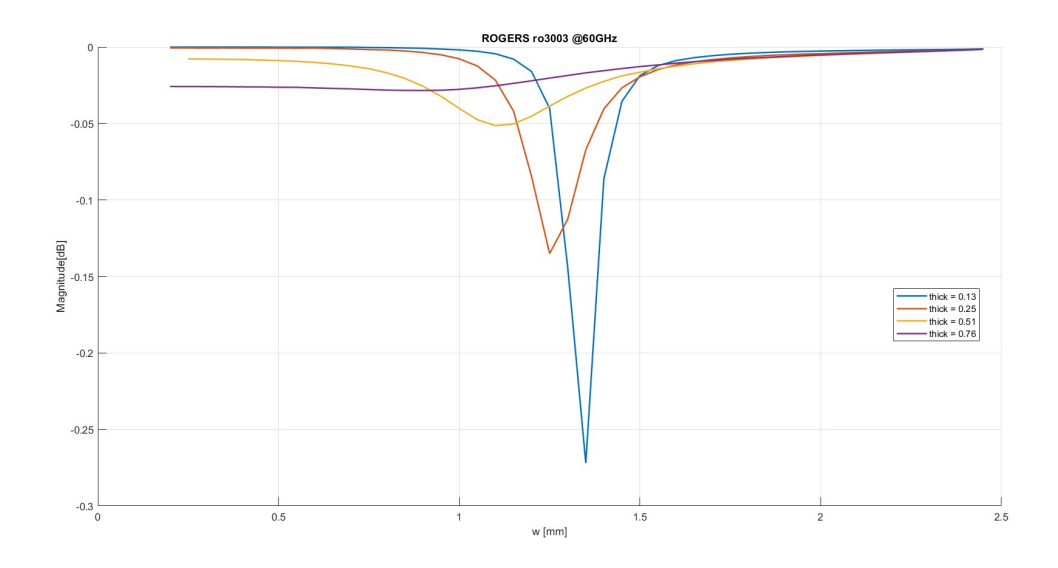


Figure 2.2.6: Magnitude of the reflection coefficient of the unit cell under normal incidence at 60 GHz for different substrate thicknesses.

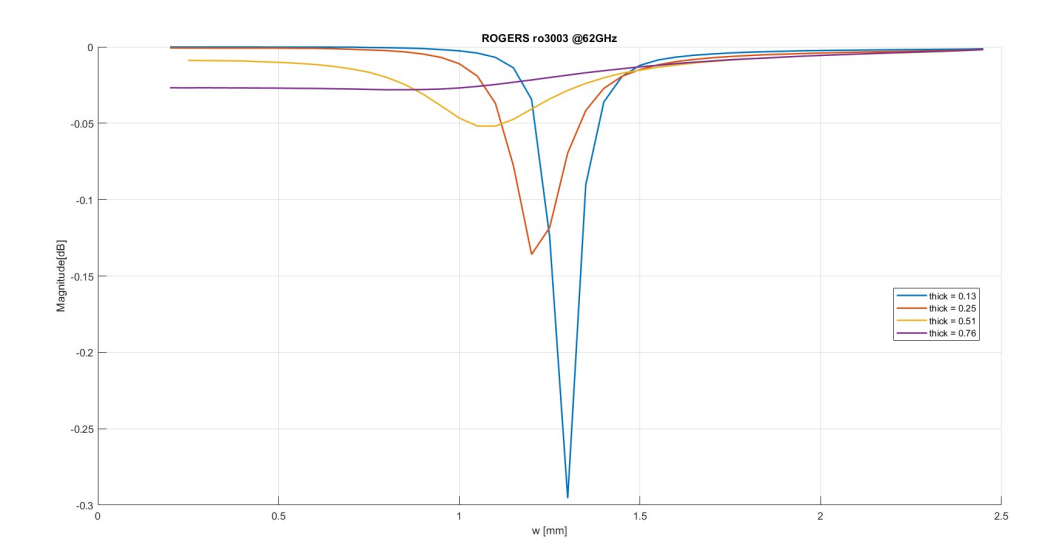


Figure 2.2.7: Magnitude of the reflection coefficient of the unit cell under normal incidence at 62 GHz for different substrate thicknesses.

From the obtained results it can be observed that the reflection phase does not always vary in a smooth and controlled way with respect to the patch dimension. In particular, the regions where the phase exhibits steep slope are undesirable for practical design, since even a small variation in the patch size or fabrication tolerances would result in a large and unpredictable phase shift, leading to instability in the overall response of the surface.

Similarly, the magnitude plots highlight the presence of multiple spikes associated with resonant phenomena. These resonances correspond to points where the unit cell is strongly mismatched and the reflected field is highly perturbed. Such behaviour is detrimental for the SES operation, as it reduces the efficiency and introduces distortions in the reflected wavefront.

From the analysis of the results, it can be noticed that for the thinner substrates, namely 0.13, mm and 0.25, mm, the obtained phase range largely exceeds 360°. However, this apparent advantage is counterbalanced by the presence of very steep variations in the phase curve, which make the response highly sensitive to small changes in the patch width and therefore unstable in practical implementations.

In addition, the reflection magnitude for these thicknesses exhibits more pronounced resonant spikes, indicating stronger mismatches and higher losses around specific patch dimensions. This behaviour further compromises the efficiency of the unit cell.

For these reasons, the 0.13, mm and 0.25, mm laminates were discarded as potential candidates for the SES substrate.

On the other hand, the substrates with thicknesses of 0.51, mm and 0.76, mm exhibit a much more suitable behaviour. In particular, the 0.51, mm laminate provides a complete 360° phase coverage, while the 0.76, mm laminate achieves a range of approximately 300°. In both cases, the phase response shows a smooth and gradual variation with respect to the patch width, ensuring better stability and predictability of the unit cell behaviour.

Moreover, the reflection magnitude remains stable and free of significant resonant spikes, which indicates low losses and a reliable electromagnetic response. For these reasons, the 0.51, mm and 0.76, mm laminates were selected as the most promising candidates.

2.2.2 Analysis for oblique incidence

After identifying 0.51, mm and 0.76, mm as the most promising substrate thicknesses, a further analysis was performed to evaluate their robustness under oblique incidence conditions. The reflection coefficient, both in terms of magnitude and phase, was extracted for incidence angles ranging from 0° to 50°, at the frequencies of 58, 60, and 62 GHz. The resulting curves are reported below.

Results Thickness 0.51mm

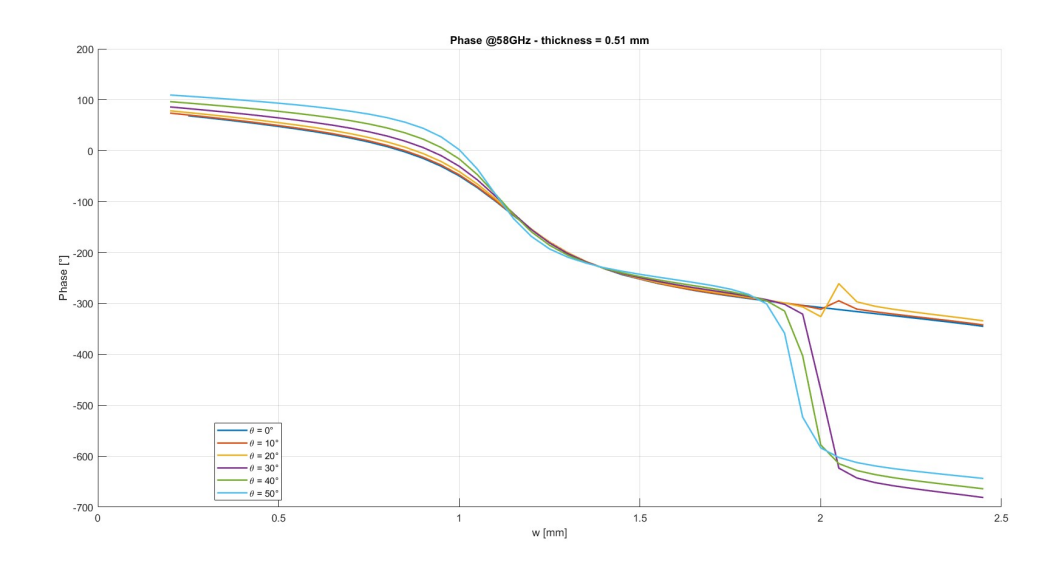


Figure 2.2.8: Phase response of the unit cell under oblique incidence at 58 GHz for 0.51mm substrate thicknesses.

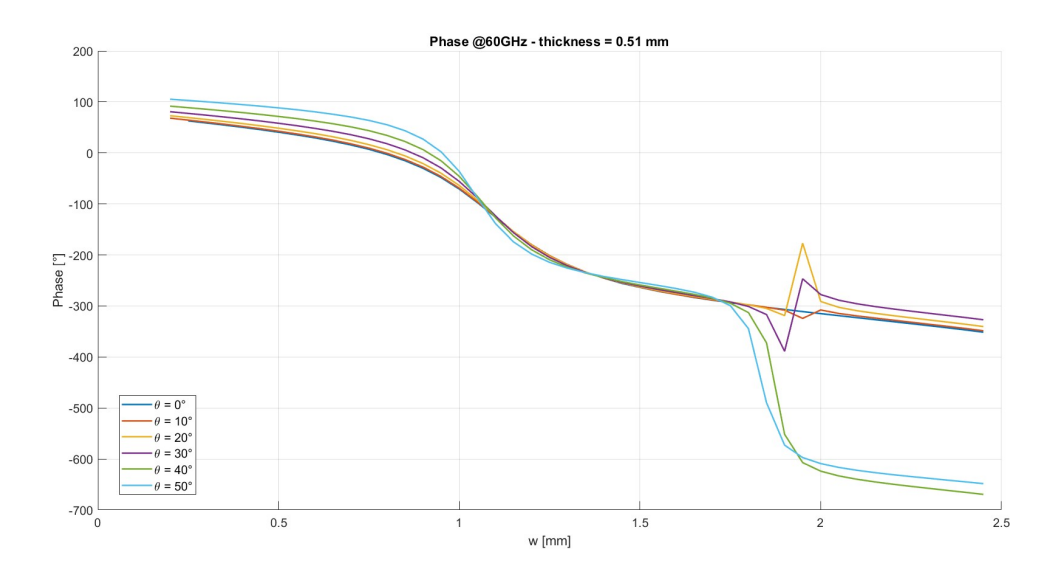


Figure 2.2.9: Phase response of the unit cell under oblique incidence at 60 GHz for 0.51mm substrate thicknesses.

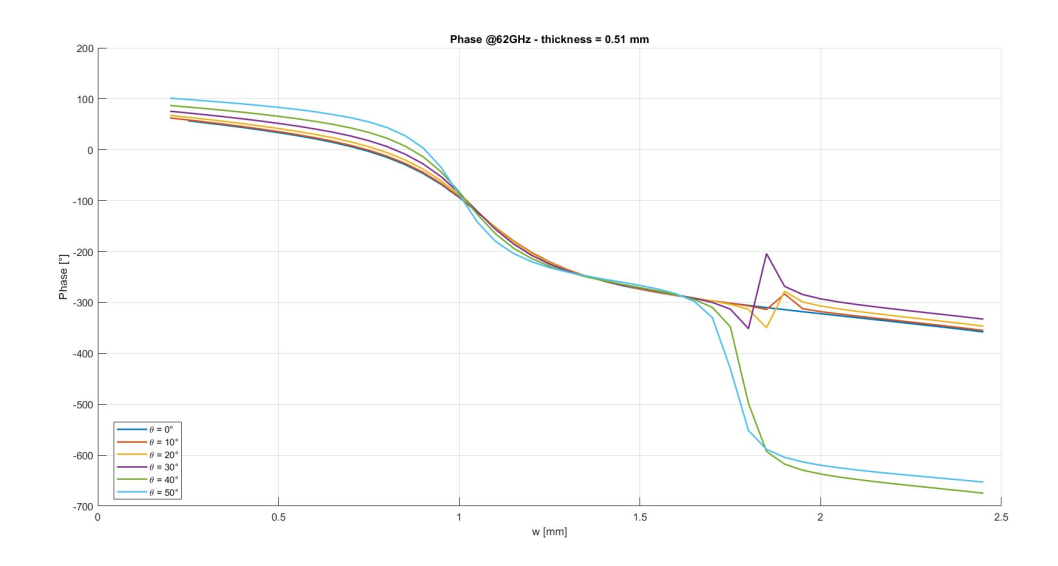


Figure 2.2.10: Phase response of the unit cell under oblique incidence at 62 GHz for 0.51mm substrate thicknesses.

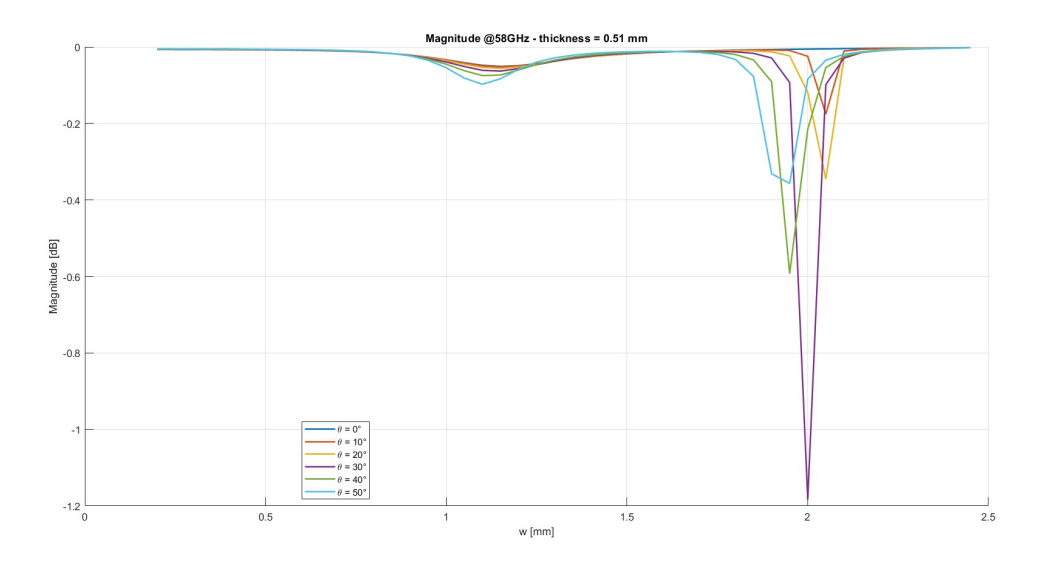


Figure 2.2.11: Magnitude of the reflection coefficient of the unit cell under oblique incidence at 58 GHz for 0.51mm substrate thicknesses.

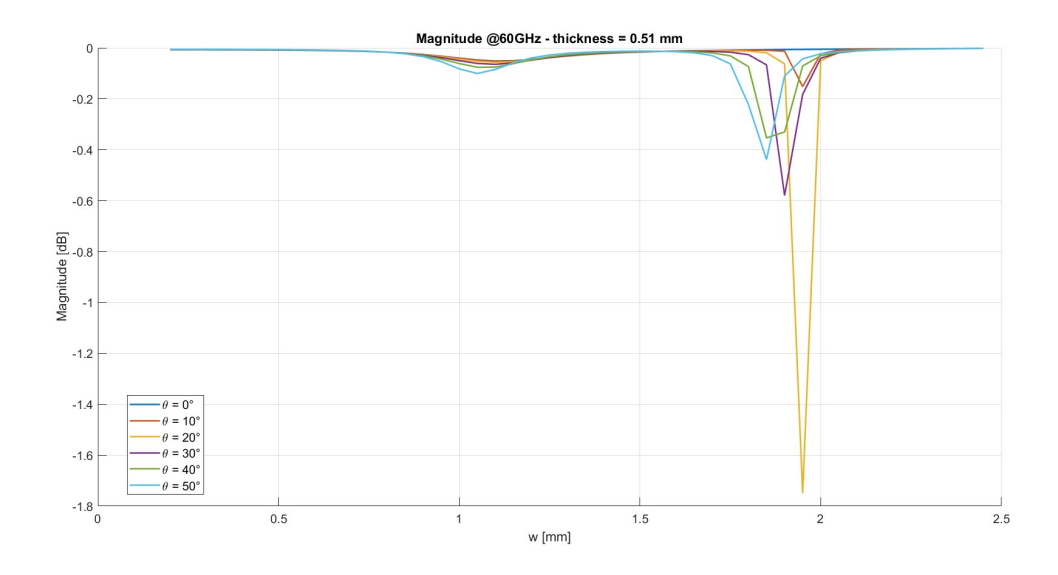


Figure 2.2.12: Magnitude of the reflection coefficient of the unit cell under oblique incidence at 60 GHz for 0.51mm substrate thicknesses.

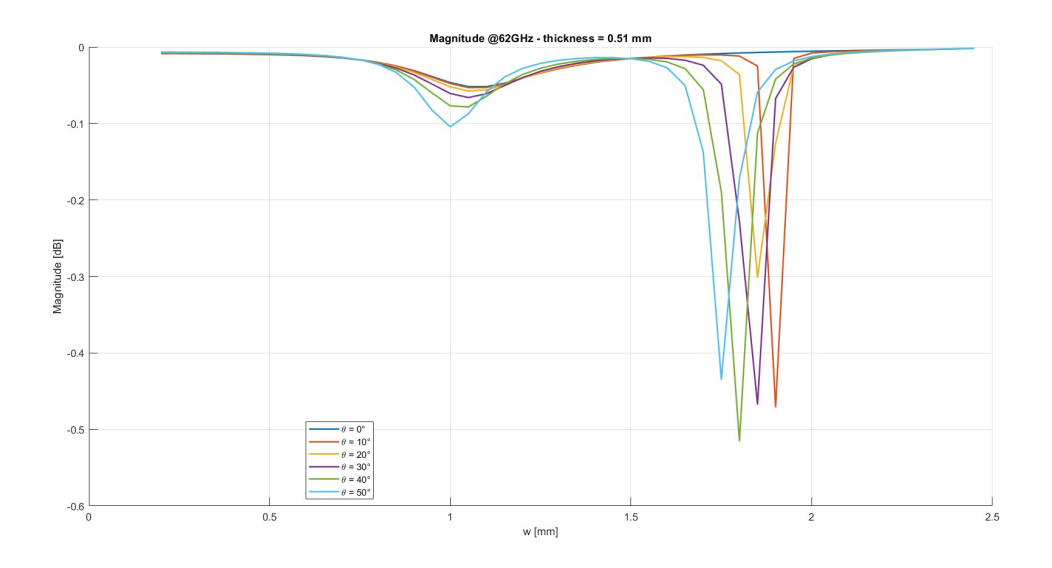


Figure 2.2.13: Magnitude of the reflection coefficient of the unit cell under oblique incidence at 62 GHz for 0.51mm substrate thicknesses.

Results Thickness 0.76mm

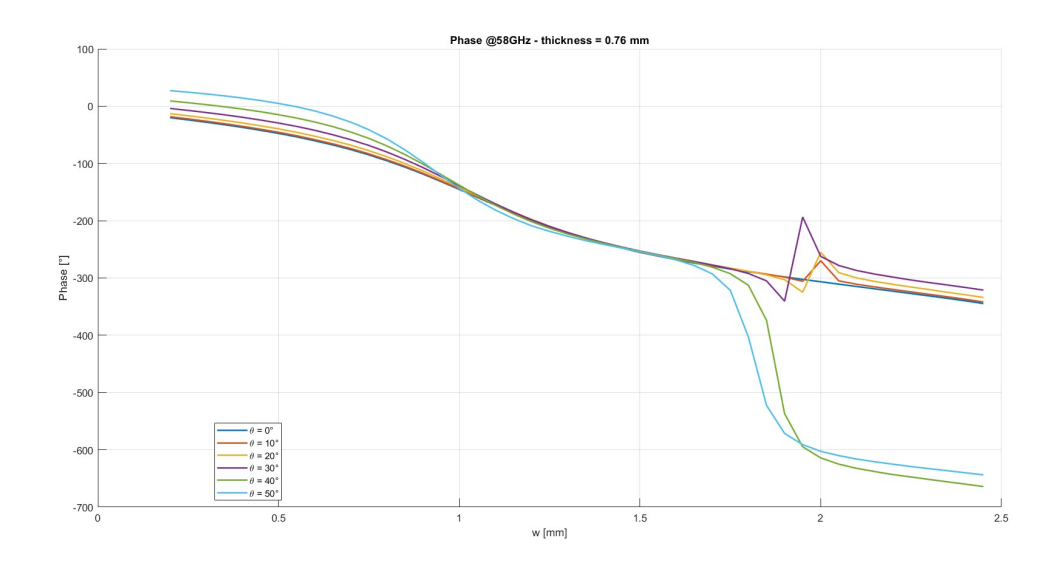


Figure 2.2.14: Phase response of the unit cell under oblique incidence at 58 GHz for 0.76mm substrate thicknesses.

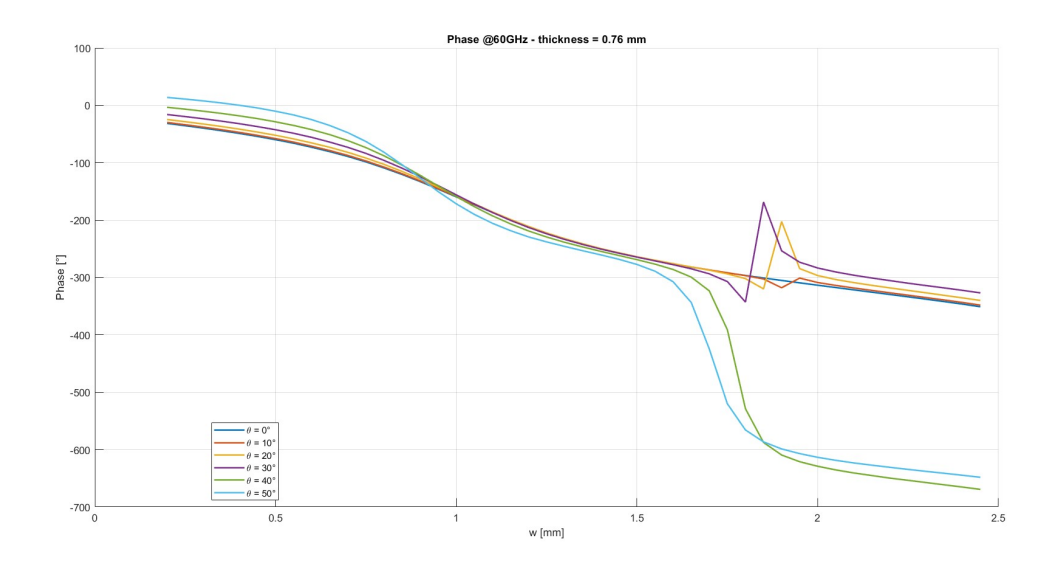


Figure 2.2.15: Phase response of the unit cell under oblique incidence at 60 GHz for 0.76mm substrate thicknesses.

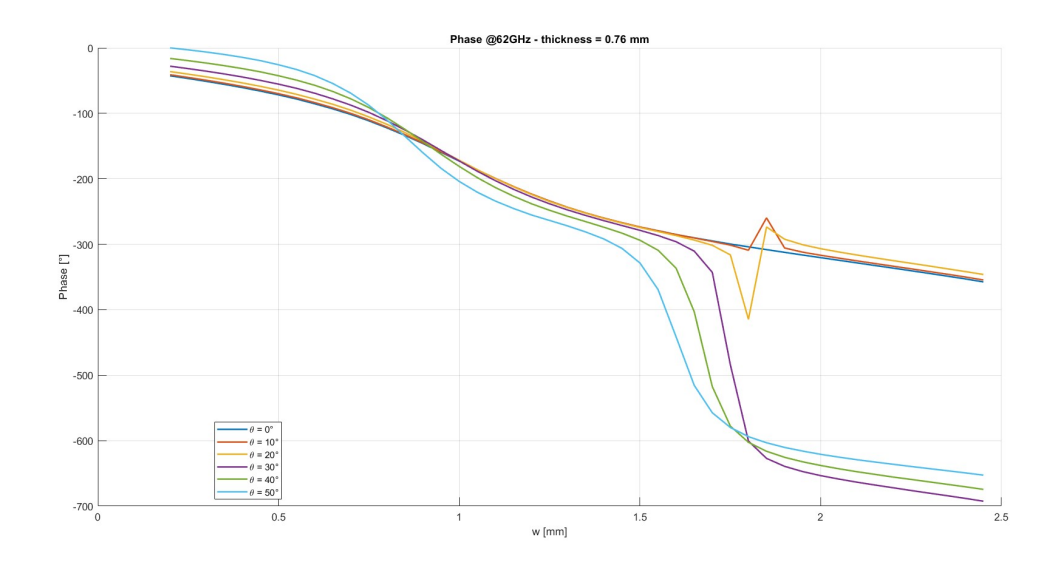


Figure 2.2.16: Phase response of the unit cell under oblique incidence at 62 GHz for 0.76mm substrate thicknesses.

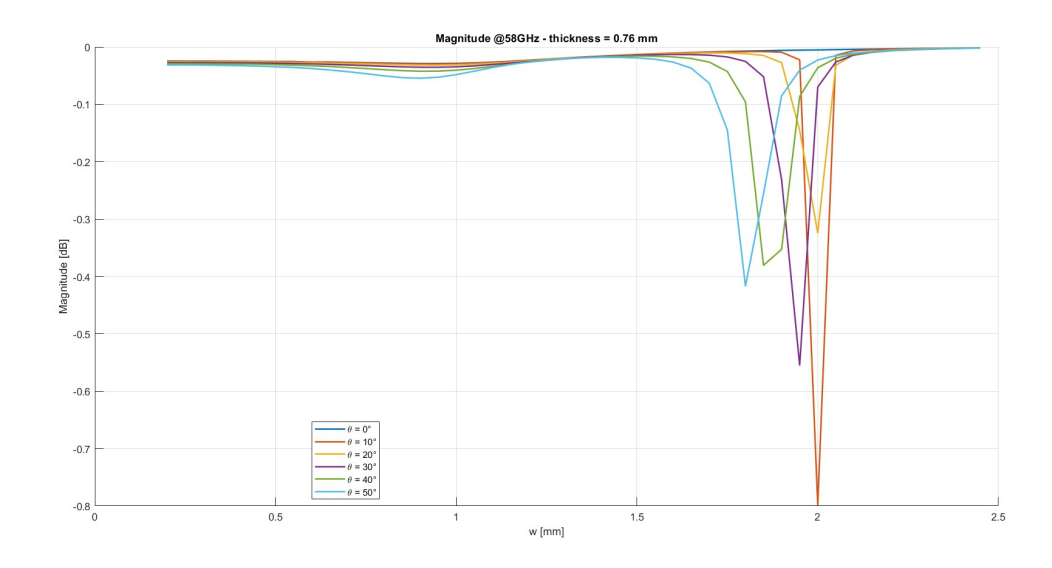


Figure 2.2.17: Magnitude of the reflection coefficient of the unit cell under oblique incidence at 58 GHz for 0.76mm substrate thicknesses.

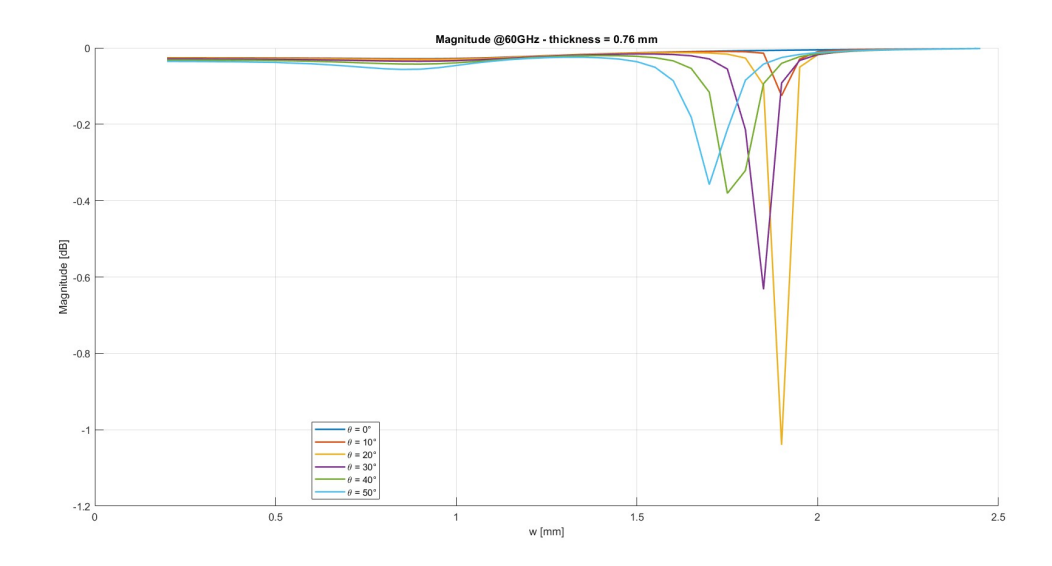


Figure 2.2.18: Magnitude of the reflection coefficient of the unit cell under oblique incidence at 60 GHz for 0.76mm substrate thicknesses.

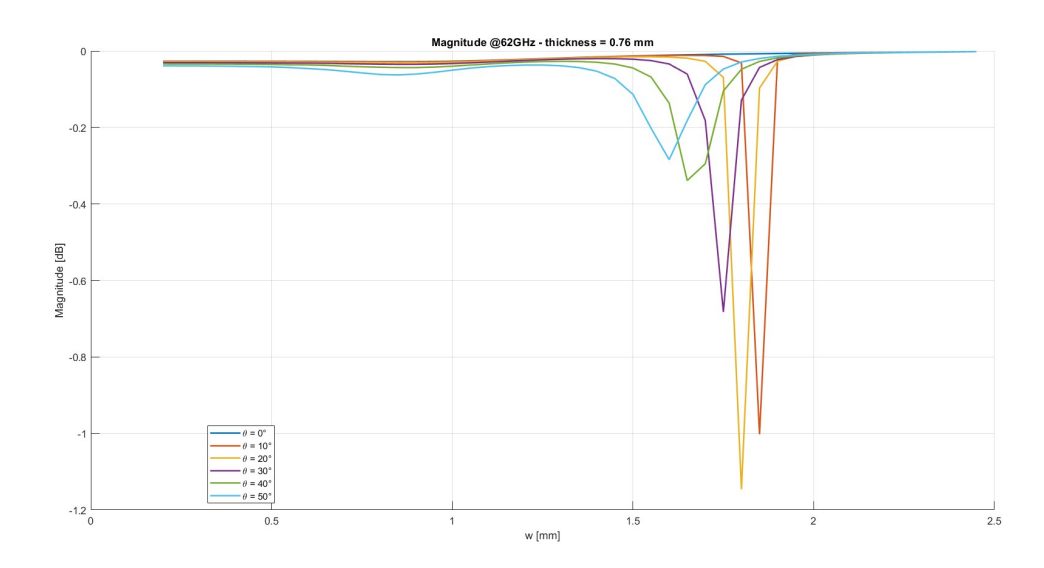


Figure 2.2.19: Magnitude of the reflection coefficient of the unit cell under oblique incidence at 62 GHz for 0.76mm substrate thicknesses.

Compared to the normal incidence case, when larger incidence angles are considered the phase response exhibits sharp variations around a patch width of approximately 1.75, mm, which reduces the usable phase range of the unit cell.

For the 0.76, mm substrate, these effects are more pronounced: the magnitude response shows stronger resonance spikes, while the phase, especially at higher frequencies, becomes less stable.

Conversely, the 0.51, mm thickness provides a wider and smoother phase range across all the analyzed frequencies, together with less pronounced resonances in the magnitude response.

For these reasons, the 0.51, mm substrate has been identified as the most suitable choice for the subsequent SES design.

Chapter 3

Design of Smart Electromagnetic Skins

Once the single UC is characterized, it is possible to synthetize the complete smart electromagnetic skin.

The main objective is to determine the physical dimensions of the patch element in each unit cell so that the overall surface provides the desired phase distribution when illuminated by an external feed.

The reflection phase curves obtained for the selected substrate thickness in the previous chapter form the basis for the SES design. These curves relate the patch width to the phase shift of the reflected wave. By interpolating them, the required patch width for each unit cell can be determined, ensuring that the target phase profile is accurately reproduced across the array.

Since the phase response is nonlinear and frequency-dependent, the interpolation must be performed carefully to avoid abrupt jumps and maintain a smooth phase variation. Once the patch dimensions are established for all elements, the complete SES layout can be generated and prepared for full-wave simulation or fabrication.

3.1 Required Phase Distribution

The methodology to evaluate the phase shift required for each unit cell is described in [27]. This approach allows calculating the phase distribution that each element must provide to achieve the desired wavefront shaping, taking into account the relative position of the unit cells within the array.

The coordinate system considered for this analysis is shown in the figure below:

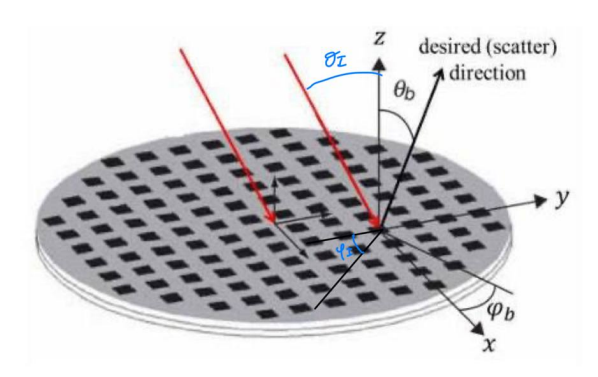


Figure 3.1.1: Coordinate system used for the analysis of the required phase distribution [27]

The progressive phase distribution across the surface, required to direct the reflected beam toward a target direction (θ_b, φ_b) , can be written as:

$$\phi(x_i, y_i) = -k_o \sin \theta_b \cos \varphi_b, x_i - k_o \sin \theta_b \sin \varphi_b, y_i$$
(3.1.1)

where k_0 indicates the free-space propagation constant at frequency f_0 , and (x_i, y_i) denote the coordinates of the *i*-th element.

The total phase of the reflected field at each position is obtained as the sum of the phase of the incoming wave and the additional phase contribution imparted by the unit cell:

$$\phi(x_i, y_i) = k_o d_i + \phi_R(x_i, y_i) \tag{3.1.2}$$

where $\phi_R(x_i, y_i)$ represents the reflection phase associated with the *i*-th element, while d_i is the distance between the source and that element. In the case of a source located in the far-field, as for a SES, the incident field can be modeled with a plane wave, and the term k_0d_i reduces to:

$$k_o d_i = k_o(x_i \sin \theta_I \cos \varphi_I + y_i \sin \theta_I \sin \varphi_I \tag{3.1.3}$$

where (θ_I, φ_I) define the direction of arrival of the incident plane wave (see Fig.3.1.1)

Combining 3.1.1 and 3.1.3 the required phase shift at each element is given by:

$$\phi_R(x_i, y_i) = -k_o x_i [\sin\theta_I \cos\varphi_I + \sin\theta_b \cos\varphi_b] + y_i [\sin\theta_I \sin\varphi_I + \sin\theta_b \sin\varphi_b] \quad (3.1.4)$$

3.1.1 Field on the Reflectarray Elements and Scattered Field

The plane wave field incident on each UC is given by

$$E_n(\theta_I, \varphi_I) = e^{jkr_i\hat{\eta}}$$

where $\hat{\eta}$ corresponds to $\hat{\theta}$ or $\hat{\varphi}$ depending on the polarization of the incoming wave, while (θ_I, φ_I) indicates its actual angle of incidence. If the field across each element is considered uniform and approximated by its value at the element's center, then the term kr_i can be simplified as follows:

$$kr_i = k(x_i \sin \theta_I \cos \varphi_I + y_i \sin \theta_I \sin \varphi_I)$$

The field at each element is transformed into the Cartesian components by the expression

$$\mathbf{E}_{RC} = \begin{bmatrix} E_{Rx} \\ E_{Ry} \\ E_{Rz} \end{bmatrix} = \begin{bmatrix} \sin \theta_I \cos \varphi_I & \cos \theta_I \cos \varphi_I & -\sin \varphi_I \\ \sin \theta_I \sin \varphi_I & \cos \theta_I \sin \varphi_I & \cos \varphi_I \\ \cos \theta_I & -\sin \theta_I & 0 \end{bmatrix} \begin{bmatrix} 0 \\ E_{\theta} \\ E_{\varphi} \end{bmatrix}$$

For simplicity, the subscript i referring to the element index has been omitted. The vector on the right-hand side of the previous equation describes the case of an arbitrarily polarized incident plane wave. This transformation is applied to all the elements of the surface for the actual direction of incidence (θ_I, φ_I) , which may differ from the nominal design direction. The x and y components of \mathbf{E}_{RC} represent the complex amplitudes of the incident electric field on each element.

Subsequently, the scattered field produced by the metasurface in response to the incident wave can be expressed as follows:

$$E_{\theta}(\theta, \varphi) = jk \frac{e^{-jkr}}{2\pi r} \left[\cos \varphi \, \tilde{E}_{Rx}(u, v) + \sin \varphi \, \tilde{E}_{Ry}(u, v) \right]$$

$$E_{\varphi}(\theta,\varphi) = jk \frac{e^{-jkr}}{2\pi r} \left[-\sin\varphi \,\tilde{E}_{Rx}(u,v) + \cos\varphi \,\tilde{E}_{Ry}(u,v) \right] \cos\theta$$

where

$$\tilde{E}_{Rx,y}(u,v) = K_1 p_x p_y \operatorname{sinc}\left(\frac{kup_x}{2}\right) \operatorname{sinc}\left(\frac{kvp_y}{2}\right) \sum_{m=0}^{N_x-1} \sum_{n=0}^{N_y-1} E_{x/y}^{m,n}(m,n) e^{jk(ump_x+vnp_y)}$$

and

$$K_1 = e^{-jkr/2[j\lambda(u_x-1)p_x(v_y-1)p_y]}$$

$$u = \sin \theta \cos \varphi, \qquad v = \sin \theta \sin \varphi$$

 N_x and N_y are the number of elements along the x and y axes, respectively. p_x and p_y are the periodic spacings of the elements in the x and y axes, respectively. The Bistatic Scattering Cross-Section (BSCS) of the metasurface is given by

$$\sigma_{\eta\psi}(\theta_I, \varphi_I, \theta_b, \varphi_b) = \lim_{R \to \infty} 4\pi r^2 \left| \frac{E_{\psi}^b}{E_{\eta}^I} \right|$$

Here, η and ψ refer to the polarizations of the incident and scattered fields, respectively, while they are also associated with the corresponding incident and scattered directions. By substituting the expressions introduced above, the scattered field can be obtained as

$$\sigma_{\psi\theta}(\theta_I, \varphi_I, \theta_b, \varphi_b) = \frac{4\pi}{\lambda^2} \left[\cos \varphi_b \, \tilde{E}_{Rx}(u_b, v_b) + \sin \varphi_b \, \tilde{E}_{Ry}(u_b, v_b) \right]^2$$

$$\sigma_{\varphi\varphi}(\theta_I, \varphi_I, \theta_b, \varphi_b) = \frac{4\pi}{\lambda^2} \left[-\sin \varphi_b \, \tilde{E}_{Rx}(u_b, v_b) + \cos \varphi_b \, \tilde{E}_{Ry}(u_b, v_b) \right]^2 \cos^2 \theta_b$$

For the Monostatic Scattering Cross-Section (MSCS), the scattered angles coincide with the incident angles, i.e., $\theta_b = \theta_I$ and $\varphi_b = \varphi_I$. It is important to note that this derivation neglects mutual coupling between the elements and diffraction effects from the edges of the finite metasurface.

3.2 Mapping the Required Phase to Patch Dimensions

Once the required phase distribution $\phi_R(x_i, y_i)$ has been determined for the entire aperture, the next step consists in translating this profile into the physical geometry of each unit cell. This translation relies on the reflection phase curves obtained during the electromagnetic characterization of the unit cell, as discussed in the previous chapter. Such curves describe the relationship between the patch width W and the reflection phase at different frequencies and incidence angles.

For the chosen substrate thickness of 0.51 mm, which has shown the most stable behavior in terms of both magnitude and phase, the reflection phase at 60 GHz was selected as the reference. The goal is therefore to associate each required phase shift $\phi_R(x_i, y_i)$ with the corresponding patch width W. Since the dependence of the phase on W is nonlinear, a direct analytical inversion is not possible; instead, an interpolation procedure is applied to retrieve the correct patch size. In this way, the mapping process ensures that each element of the SES provides the phase contribution required by the design.

This approach makes it possible to construct a complete map of patch dimensions across the SES surface. The resulting layout is then used to generate the array geometry in the electromagnetic solver, enabling full-wave simulations of the overall structure. The workflow of this design stage can be summarized as follows:

- 1. Compute the required phase profile $\phi_R(x_i, y_i)$ for each element using Eq. (3.1.1)–(3.1.3).
- 2. Select the substrate thickness and operating frequency for which the phase curves are available.
- 3. Interpolate the reflection phase vs. patch width curves to identify the patch dimension corresponding to each required phase.
- 4. Assemble the complete SES layout by assigning the calculated patch width to every unit cell in the array.

3.3 Full-Wave Simulation and Validation

Once the SES layout has been fully defined, the next step is to validate its performance through full-wave electromagnetic simulations. The complete array was modeled in CST Microwave Studio by assembling the unit cells with the interpolated patch widths derived in the previous section. The simulation was carried out by illuminating the surface with a plane wave at the operating frequency of 60, GHz, under open boundary conditions to reproduce free-space propagation.

The analysis focused on verifying that the reflected wave is redirected toward the desired direction (θ_b, φ_b) , in accordance with the theoretical phase distribution. In particular, the simulated radiation patterns were used to evaluate the beam pointing capability, the directivity of the main lobe, and the presence of side lobes arising from the discretization of the aperture. Furthermore, the frequency response of the SES was examined to assess its stability in a narrow band around the design frequency.

$3.3.1 \quad 10 \text{x} 10 \text{ SES design}$

In this section, the design methodology is applied to a practical case study.

Before designing the 24×24 SES, a smaller prototype composed of 10×10 unit cells was first analyzed. This preliminary simulation was carried out to validate the design methodology and verify the correct beam steering behavior of the surface. By starting with a reduced array, it was possible to quickly assess the effectiveness of the phase mapping approach and the expected reflection characteristics before scaling up to a larger aperture.

In this section a smart electromagnetic skin composed of an array of 10×10 unit cells is considered. It corresponds to a size of $25mm \times 25mm = 5\lambda \times 5\lambda$ at the design frequency $f_0 = 60 \,\text{GHz}$ The structure is illuminated by a normally incident plane wave, i.e. with $(\theta_I = 0^\circ, \varphi_I = 0^\circ)$. The design objective is to synthesize a phase distribution across the array that redirects the reflected beam toward a target angle of $\theta_b = 30^\circ$, while maintaining $\varphi_b = 0^\circ$.

Under these conditions, the required phase shift for each unit cell can be calculated

using Eq.3.1.4. **Specifications**

• Working band: 60GHz

• Cell size: $\frac{\lambda}{2}$

• Array dimension: 10×10

• Direction of arrival of the plane wave: $\theta_I=0^\circ,\,\varphi_I=0^\circ$

 \bullet Desired direction of the reflected beam: $\theta_b=30^\circ,\,\varphi_b=0^\circ$

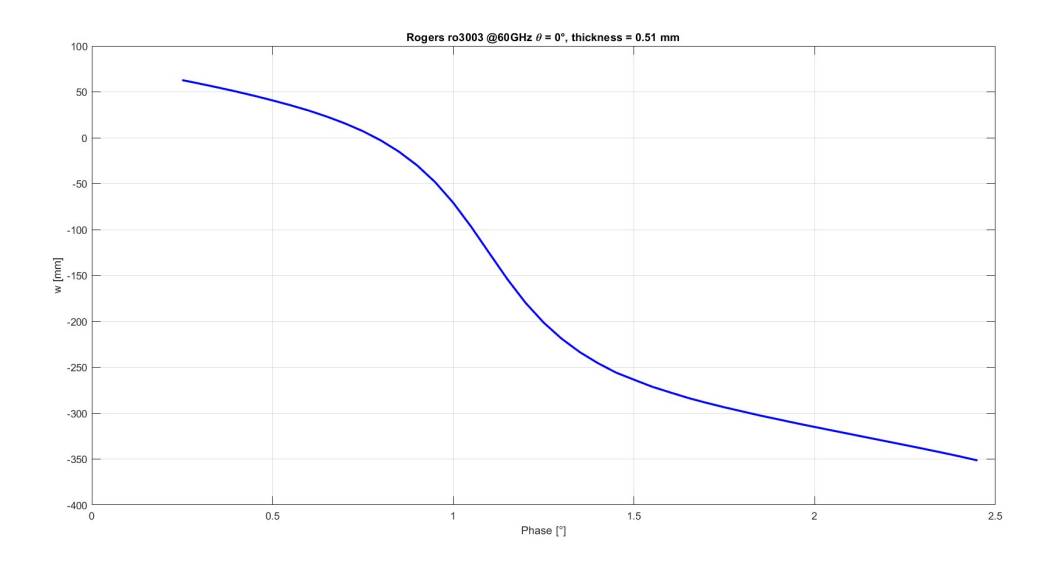


Figure 3.3.1: Phase curve used for the design

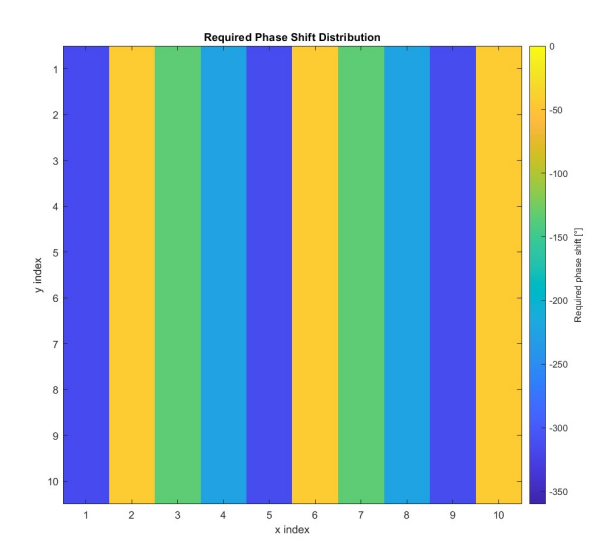


Figure 3.3.2: Required phase distribution

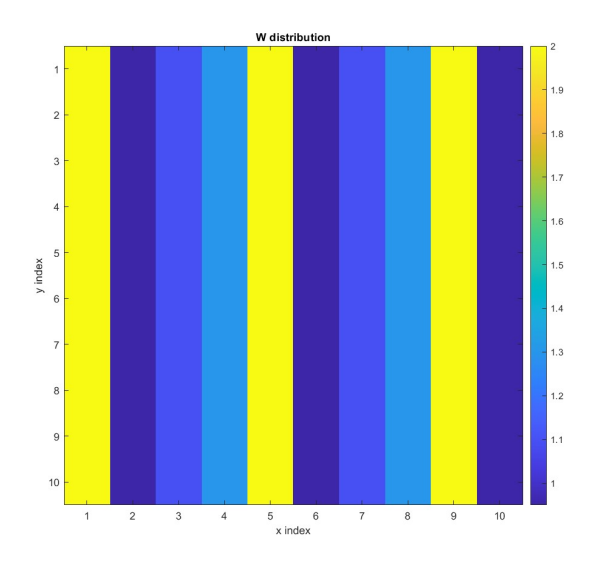
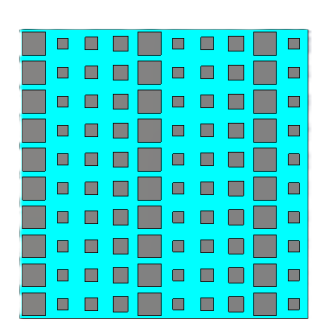


Figure 3.3.3: Patch width distribution

The design workflow is summarized in Figs. 3.3.1–3.3.3, showing how the target phase distribution is mapped into the corresponding patch width values through interpolation of the reflection phase curve. Once the required patch widths were calculated for all elements, the resulting layout was exported as a DXF file. This file was then imported into CST Studio Suite to generate the SES geometry, enabling full-wave simulation of the complete array with the exact physical dimensions.





For simplicity, only the 3D far-field pattern at 60 GHz is shown here to illustrate that the design works as intended.

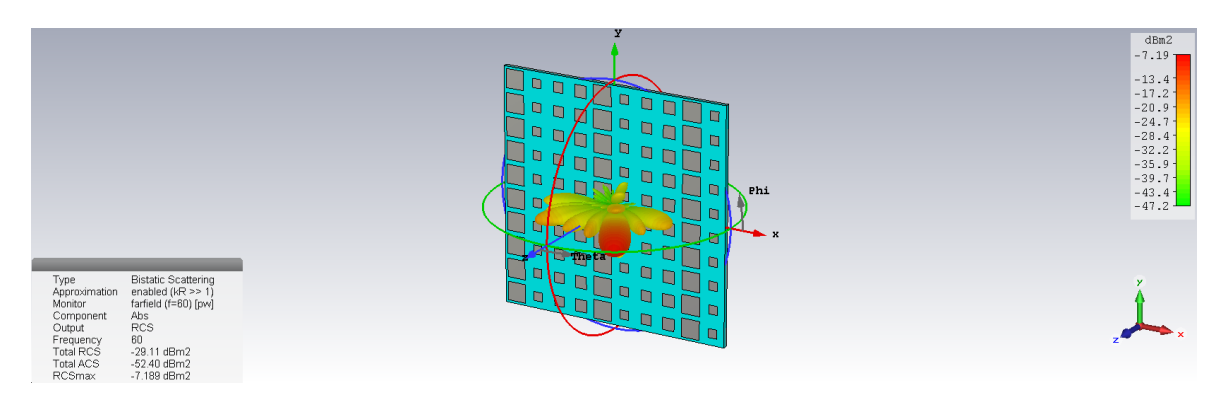


Figure 3.3.5: 3D far-field pattern at 60 GHz for the 10×10 SES

3.3.2 24x24 SES design

The methodology applied to the 10×10 array is now extended to a larger SES composed of 24×24 unit cells, corresponding to an aperture of $60 \text{ mm} \times 60 \text{ mm} = 12\lambda \times 12\lambda$ at $f_0 = 60 \text{ GHz}$. The surface is illuminated by a normally incident plane wave $(\theta_I = 0^{\circ}, \varphi_I = 0^{\circ})$, and the reflected beam is designed to point toward $\theta_b = 30^{\circ}$, $\varphi_b = 0^{\circ}$.

The layout and simulation workflow follow the same procedure outlined in Section 3.3.1 for the smaller surfaces, with the only difference being the increased number of elements.

Specifications

• Working band: 58GHz - 62 GHz (the design has been done at the central frequency 60GHz)

• Cell size: $\frac{\lambda}{2}$

• Array dimension: 24×24

• Direction of arrival of the plane wave: $\theta_I=0^\circ,\,\varphi_I=0^\circ$

• Desired direction of the reflected beam: $\theta_b=30^\circ,\,\varphi_b=0^\circ$

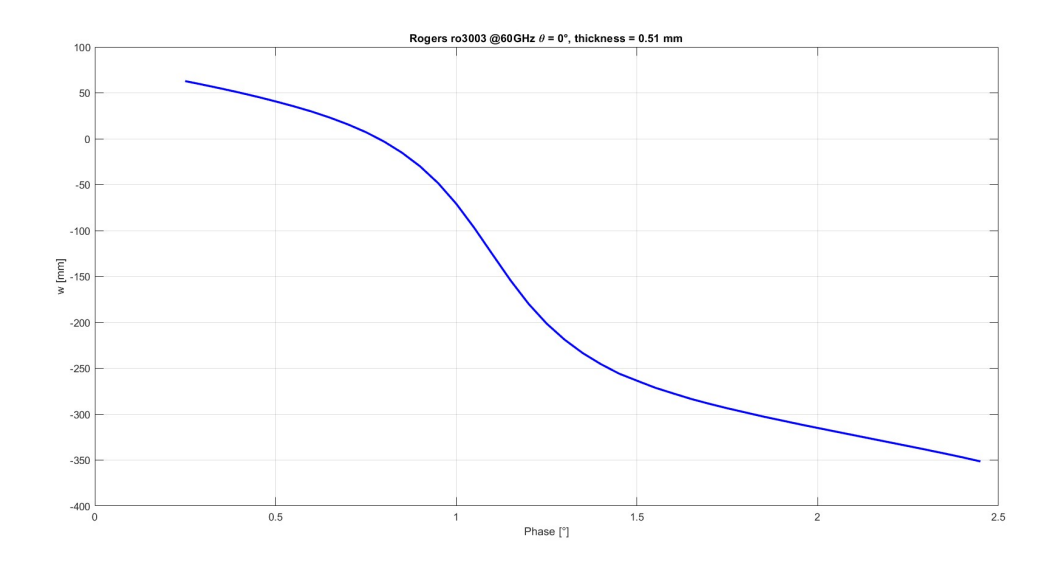


Figure 3.3.6: Phase curve used for the design

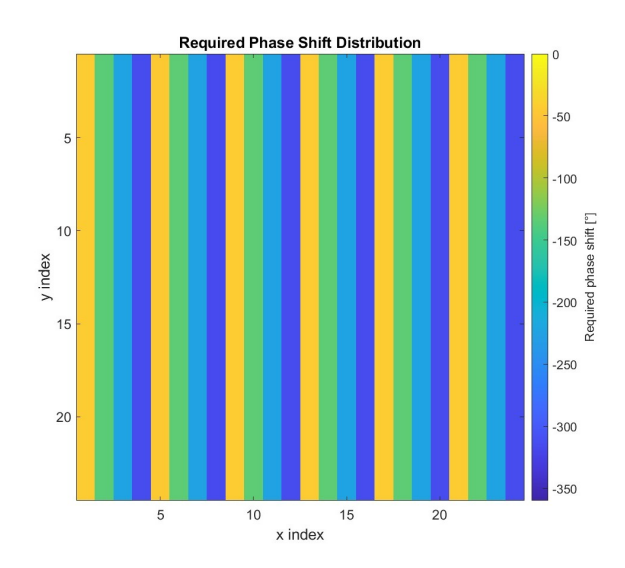


Figure 3.3.7: Required phase distribution

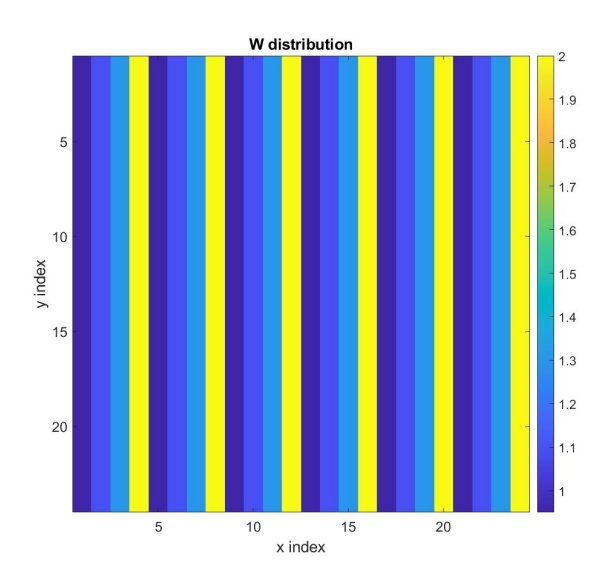


Figure 3.3.8: Patch width distribution

Based on the mapping procedure described in the previous section, the final SES layout for the 24×24 array was obtained, as shown in Fig. 3.3.8.

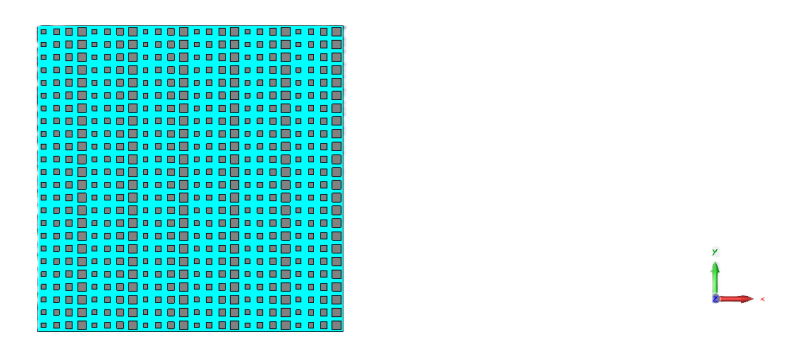


Figure 3.3.9: SES layout 24x24

In the following, the far-field results are presented, visualized both as three-dimensional (3D) radiation patterns and as Cartesian cuts along the principal planes.

It is important to note that the field observed behind the SES corresponds to the

incident plane wave.

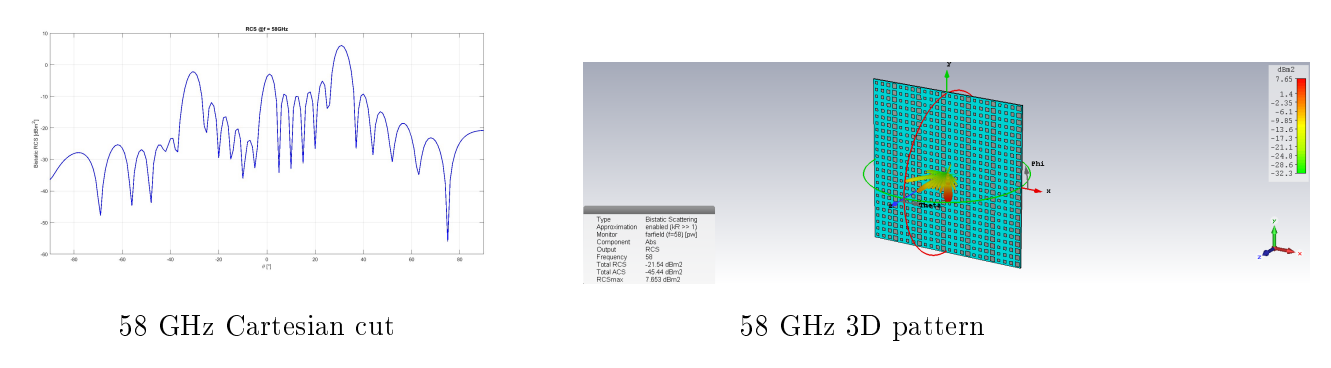


Figure 3.3.10: Farfield results at 58 GHz: Cartesian cut (left) and 3D pattern (right).

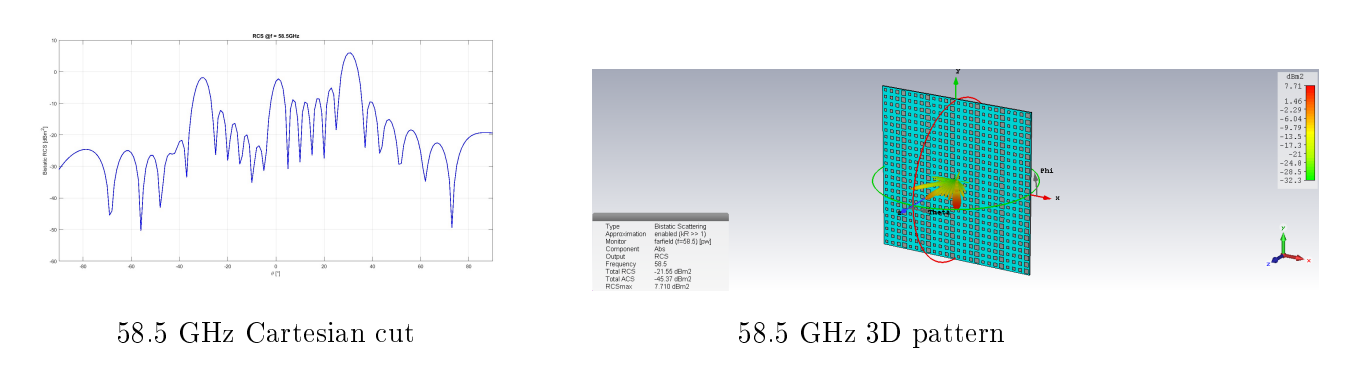


Figure 3.3.11: Farfield results at 58.5 GHz: Cartesian cut (left) and 3D pattern (right).

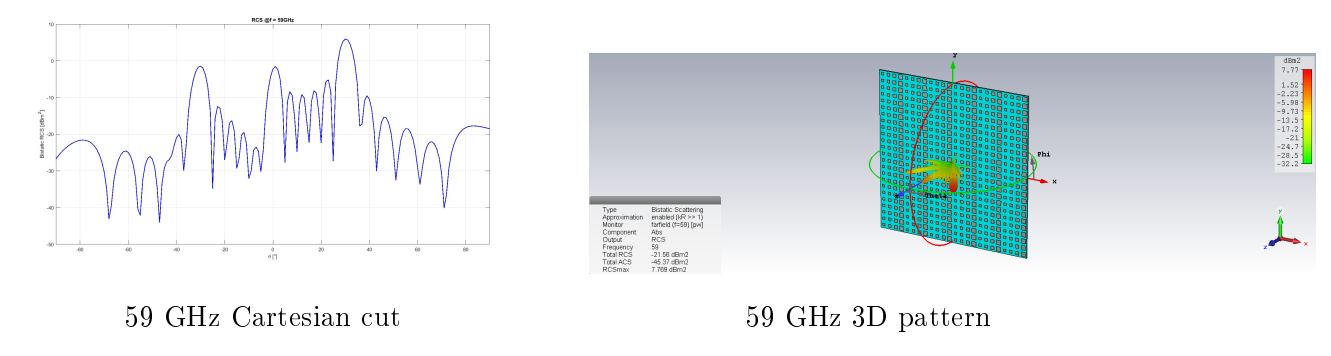


Figure 3.3.12: Farfield results at 59 GHz: Cartesian cut (left) and 3D pattern (right).

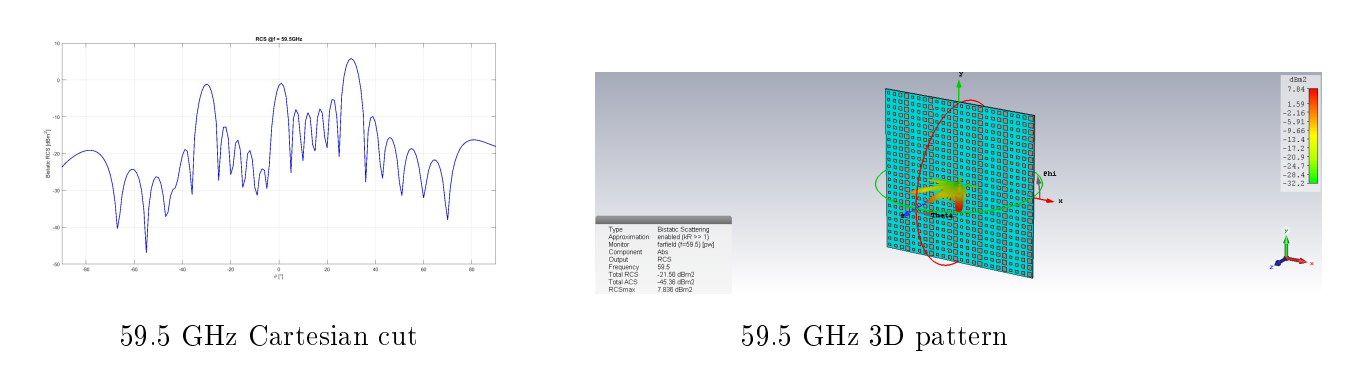


Figure 3.3.13: Farfield results at 59.5 GHz: Cartesian cut (left) and 3D pattern (right).

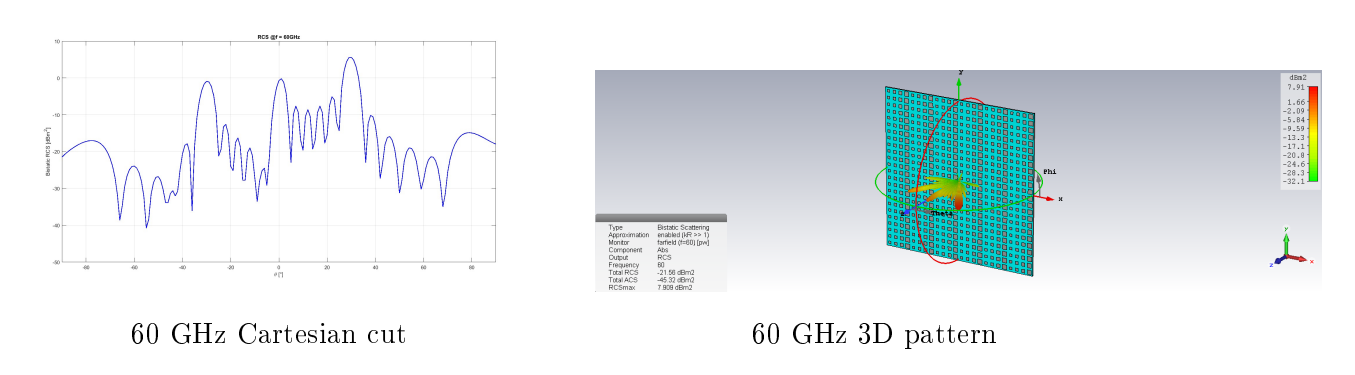


Figure 3.3.14: Farfield results at 60 GHz: Cartesian cut (left) and 3D pattern (right).

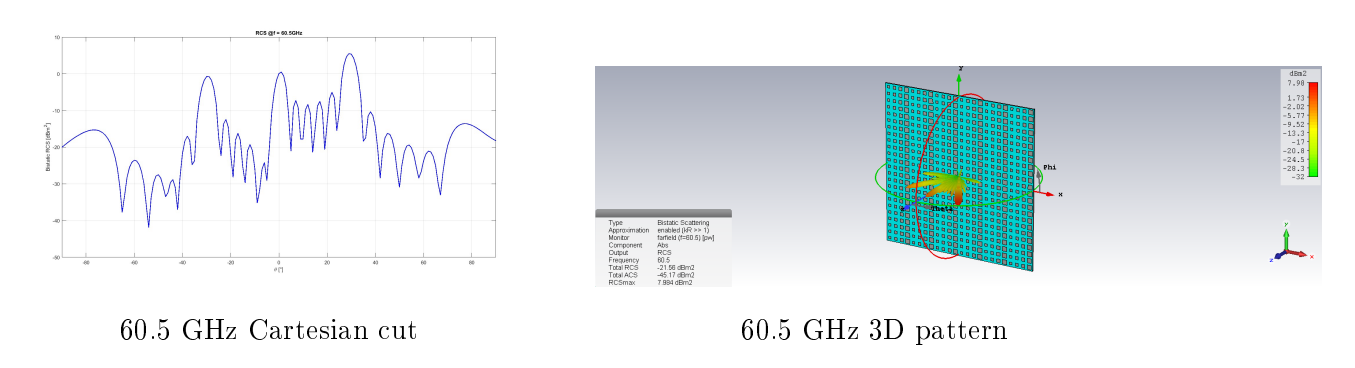


Figure 3.3.15: Farfield results at 60.5 GHz: Cartesian cut (left) and 3D pattern (right).

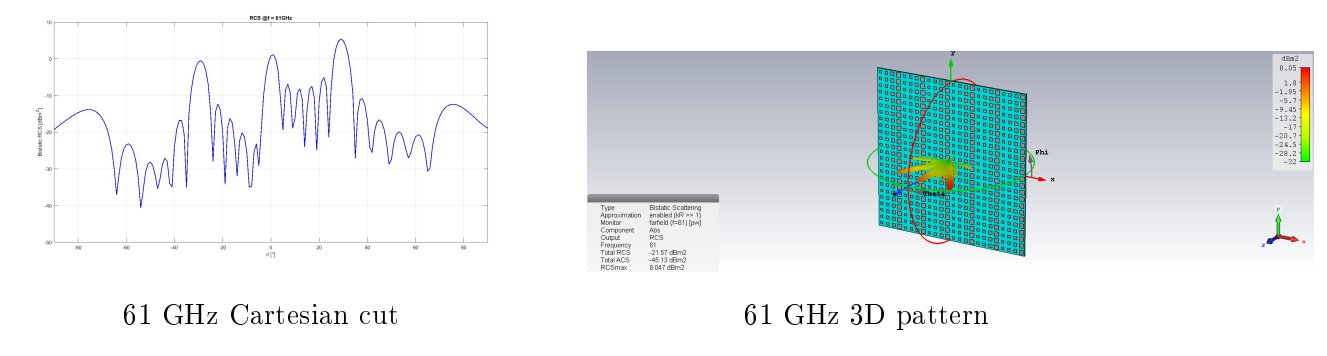


Figure 3.3.16: Farfield results at 61 GHz: Cartesian cut (left) and 3D pattern (right).



Figure 3.3.17: Farfield results at 61.5 GHz: Cartesian cut (left) and 3D pattern (right).

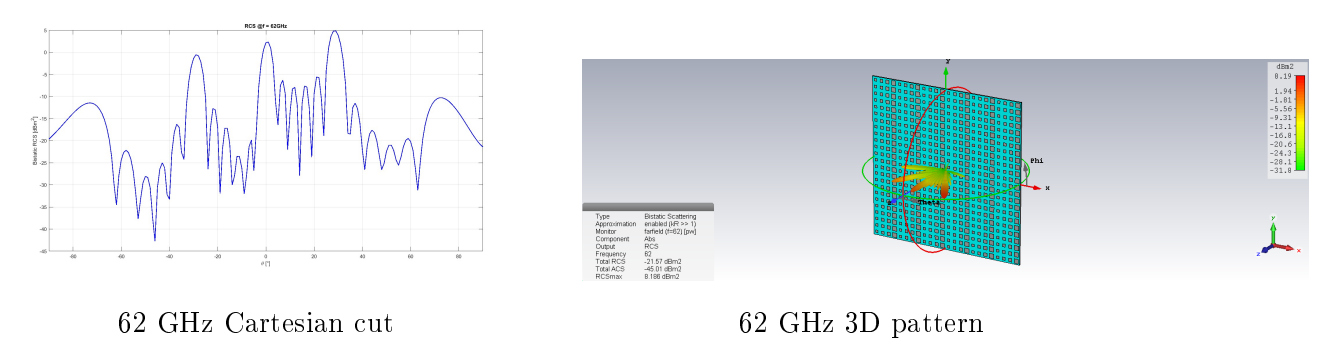


Figure 3.3.18: Farfield results at 62 GHz: Cartesian cut (left) and 3D pattern (right).

3.3.3 Results

As the frequency increases from 58 GHz to 62 GHz, some clear trends can be observed in the reflected field patterns. In particular, the power of the side lobes becomes more pronounced at higher frequencies, meaning that part of the reflected energy is no longer fully concentrated in the desired direction. At 62 GHz, this effect is even more evident: the three main lobes — corresponding to the desired reflection and two

secondary ones — reach similar power levels, showing a clear degradation of the beam focusing capability.

These behaviors are illustrated in Fig. 3.3.19, where the patterns at 58,59,60, 61 and 62 GHz are plotted together. The figure confirms that, as the frequency increases, the reflected energy tends to spread over a wider angular range, with stronger side lobes and a less defined main beam.

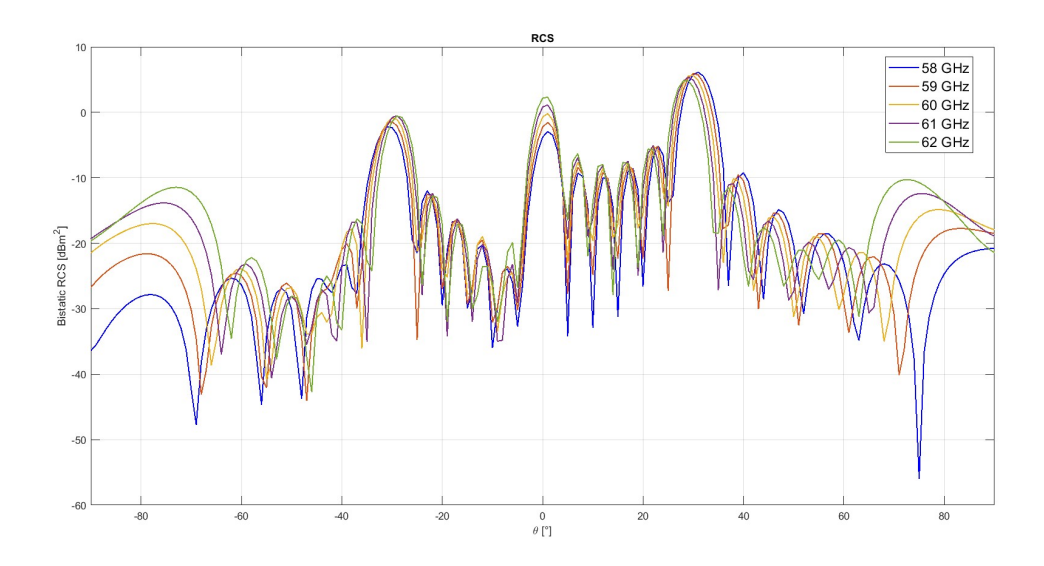


Figure 3.3.19: Comparison of the reflected field patterns at 58GHz,59GHz, 60GHz, 61GHz and 62GHz. The curves confirm that side lobes increase in magnitude and number as frequency increases, with almost comparable levels observed at 62GHz

Among the reflected lobes:

- The principal lobe at $\theta_b = 30^\circ$ represents the intended beam direction defined in the design.
- A secondary lobe is a specular reflection of the incident plane wave.
- Another secondary lobe is a specular reflection of the desired beam direction

The obtained results confirm that the designed SES can achieve beam redirection in agreement with the theoretical model, thereby validating the effectiveness of the adopted design procedure. At the same time, they highlight the frequency-dependent behavior of the SES, showing that higher operating frequencies increase side-lobe levels

and generate undesired reflections, which must be considered in practical implementations.

Chapter 4

Realistic Indoor Scenario

In this chapter, a realistic indoor scenario is considered to evaluate the effectiveness of SESs. The aim is to verify the performance of communication and localization systems at mm-Wave frequencies based on the deployment of multiple SESs. The indoor environment represents a challenging propagation context, where walls and obstacles introduce blind regions and limit direct Line-of-Sight(LoS) coverage. By strategically positioning several SESs, it is possible to manipulate the electromagnetic wavefront, enabling controlled reflections and coverage enhancement in the Non-Line-of-Sight(NLoS) areas.

More recently, the use of SESs has also been investigated for the design of passive localization systems, integrated with communication functionalities. The main advantage of passive localization is that it does not require the target to carry any active device. This not only helps to reduce costs but also ensures a higher level of privacy. If prior knowledge of the angular response of the RIS or SES is available, this information can be exploited to support the localization of an active terminal. In practice, by collecting the transmitted power associated with different RISs or SESs, and assuming that the receiver is able to distinguish the signals coming from different angular directions, it becomes possible to identify the sector from which the terminal is transmitting.

4.1 Reference Scenario

In [28], the reference scenario was analyzed. The reference scenario is shown in Fig. 4.1.1. The setup consists of an indoor laboratory with two rooms separated by a partial wall. A transmitter was placed in one room, which creates a shadowed area in the other. By deploying multiple SESs, the electromagnetic environment can be modified to extend coverage and overcome this limitation.

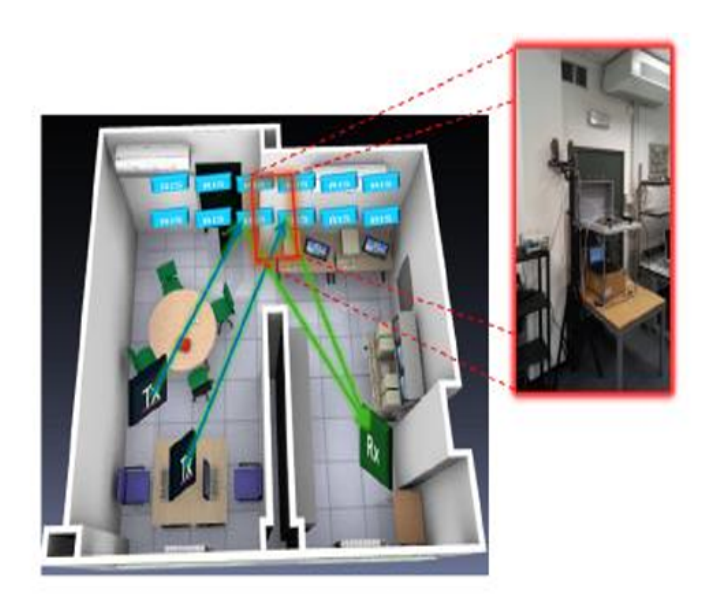


Figure 4.1.1: Realistic indoor environment with multiple SESs

Initially, a preliminary study was carried out to assess the received power distribution and to optimize the placement of the SESs, aiming at minimizing undesired interference between them, commonly referred to as cross-talk. In this context, cross-talk refers to the unintended interaction between multiple SESs, where the reflection from one surface can interfere with the beam produced by another, potentially degrading the overall signal quality and the intended coverage in the target region.

To carry out this analysis, a 2×8 patch array antenna was employed, capable of performing beam steering between -54° and $+54^{\circ}$ in azimuth, while in elevation the beam could be directed at -18° , 0° , or $+18^{\circ}$. The hardware setup previously described

was reproduced in MATLAB through ray-tracing simulations based on a propagation model accounting for up to two reflections. The beam weights were imported from the hardware configuration in order to generate realistic radiation patterns.

To evaluate the performance of the different configurations, the spillover power was analyzed by configuring the transmitter with the five optimal beams required to illuminate the five SESs placed at fixed positions in the environment. For each SES, the optimal beam was chosen by selecting the one that maximized the received power, after testing all the preconfigured beams available on the transmitter.

The analysis results and the best SES placement configuration are shown in the following figures. It is possible to clearly see how each SES is illuminated by its intended beam, as well as the spillover effects on the other surfaces. Among the tested configurations, the W-shaped arrangement proved to be the most effective (Fig. 4.1.2), ensuring optimal illumination of each SES. The corresponding spillover power distribution is reported in Fig. 4.1.3, highlighting the limited interference between adjacent SESs.

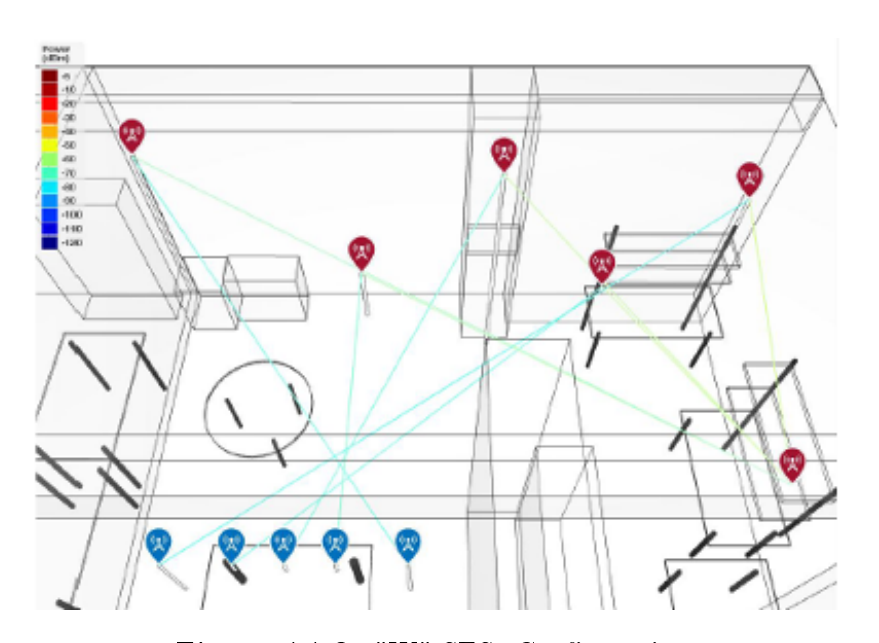


Figure 4.1.2: "W" SESs Configuration

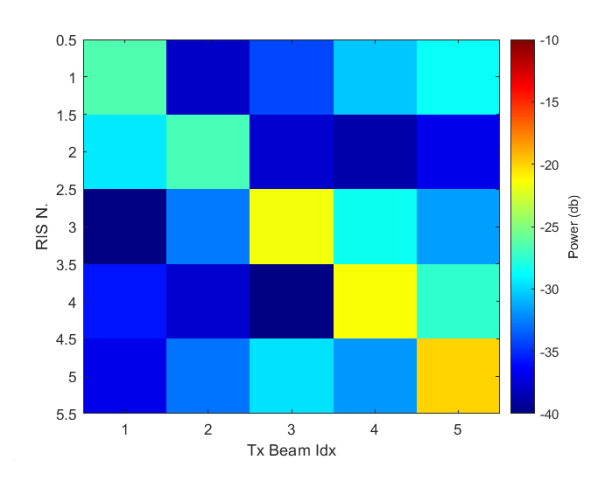


Figure 4.1.3: Spillover power for the "W" SESs configuration

For this reason, in the following analysis the W-shaped placement will be considered as the reference configuration characterizing the pointing direction of the reflected field. To make the setup clearer, the following table reports the Angles of Departure (AoD) and the corresponding Angles of Arrival (AoA), i.e the angles defining the incident direction, at each SES for the W-shaped configuration. These values provide a complete overview of how the beams are oriented within the scenario and highlight the specific directions used to illuminate each surface.

Table 4.1.1: Angles of arrival and departure (azimuth, elevation) the configuration SESs

| | Angle of Arrival [°] | | Angle of Departure [°] | |
|---------|----------------------|-----------|------------------------|-----------|
| SES | Azimuth | Elevation | Azimuth | Elevation |
| SES 1 | -26 | 5 | 39 | -20 |
| SES 2 | -38 | -12 | -91 | 0 |
| SES 3 | -48 | 8 | -124 | -23 |
| SES 4 | -70 | -18 | -140 | 0 |
| SES 5 | -93 | 9 | -151 | -12 |
| SES 6 | -26 | 6 | -62 | -14 |
| SES 7 | -48 | 12 | -113 | -15 |
| SES 8 | -70 | -15 | -131 | 1 |

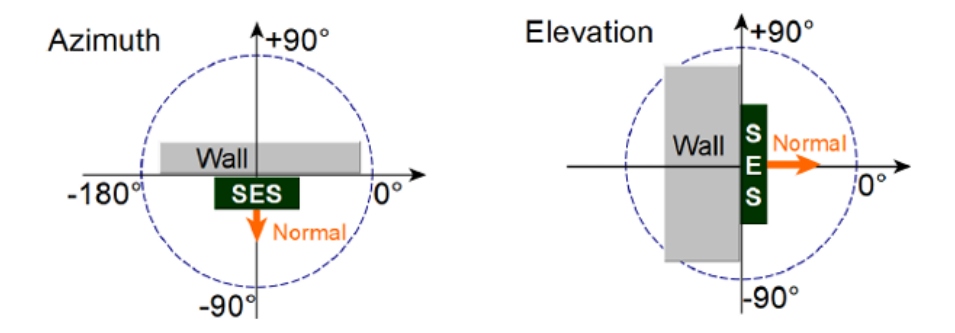


Figure 4.1.4: Angle Convention used for the Azimuth and Elevation angles

It is worth noting that the reference system adopted in Table 4.1.1 differs from the conventional spherical coordinate system but it used the azimuth and elevation angles defined in 4.1.4.

4.2 Modeling and Simulation of the SESs

The SESs of the W configuration have been designed and numerically analysed. For each surface, the complete design workflow is presented: starting from the phase response curve, proceeding to the layout design, and finally reporting the far-field radiation results. To keep the analysis focused on the intrinsic behaviour of the SESs, the simulations have been performed under plane-wave excitation. The direction of arrival of a plane wave can be represented through its propagation vector \mathbf{k} . In Cartesian coordinates, the components of the unit propagation vector can be calculated from the spherical angles θ and ϕ as follows:

$$k_x = \sin \theta \cos \phi,$$

$$k_y = \sin \theta \sin \phi,$$

$$k_z = \cos \theta.$$

Using these expressions, the Cartesian components of the propagation vector can be directly inserted in CST to define the plane-wave excitation according to the desired incidence angles.

4.2.1 SES 1

Specifications

• Working frequency: 60GHz

• Cell size: $\frac{\lambda}{2}$

• Array dimension: 20×20

• Substrate thickness: 0.51mm

• Direction of arrival of the plane wave: $\theta_I=64^\circ,\,\varphi_I=5^\circ$

• Desired direction of the reflected beam: $\theta_b=39^\circ,\,\varphi_b=-20^\circ$

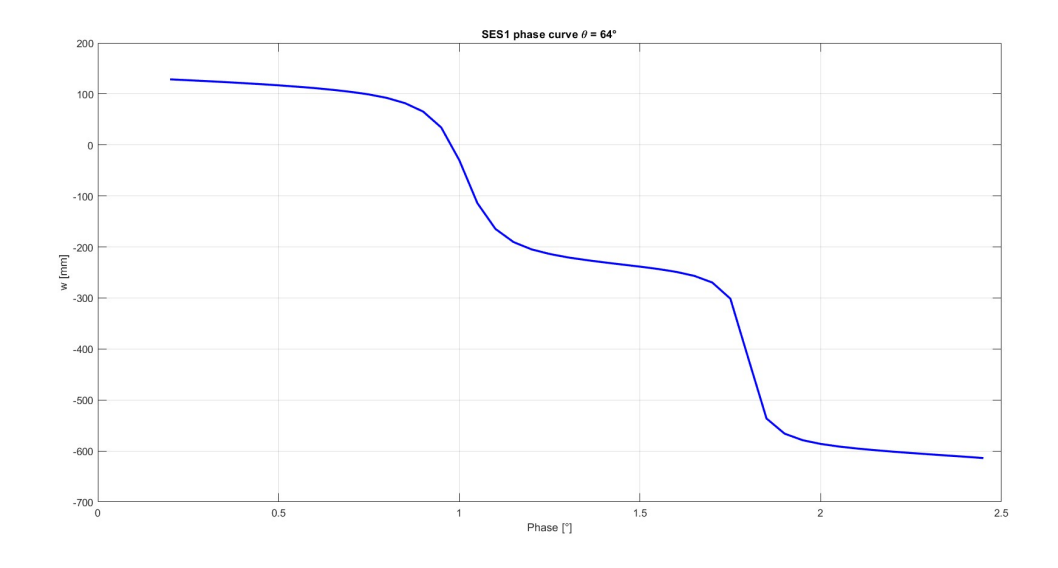


Figure 4.2.1: Phase curve used for the SES 1 design

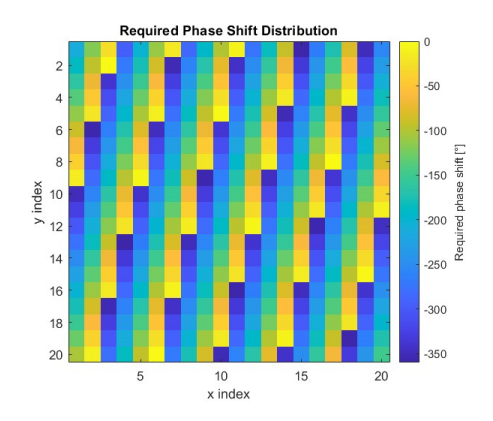


Figure 4.2.2: SES 1 Required phase distribution

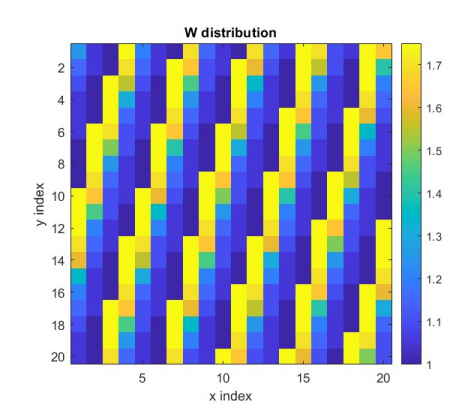


Figure 4.2.3: SES 1 Patch width distribution

The patch width distribution is used to generate the layout, which is then exported to CST Microwave Studio as a DXF file for full-wave simulation.

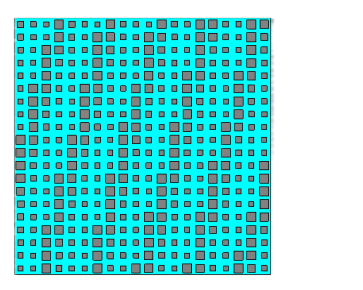


Figure 4.2.4: SES 1 layout

The results are presented in terms of the 3D radiation pattern, providing a global view of the reflected beam, and the 2D cuts of the Radar Cross Section (RCS), which allow a clearer analysis of the main lobe direction and side lobe levels.

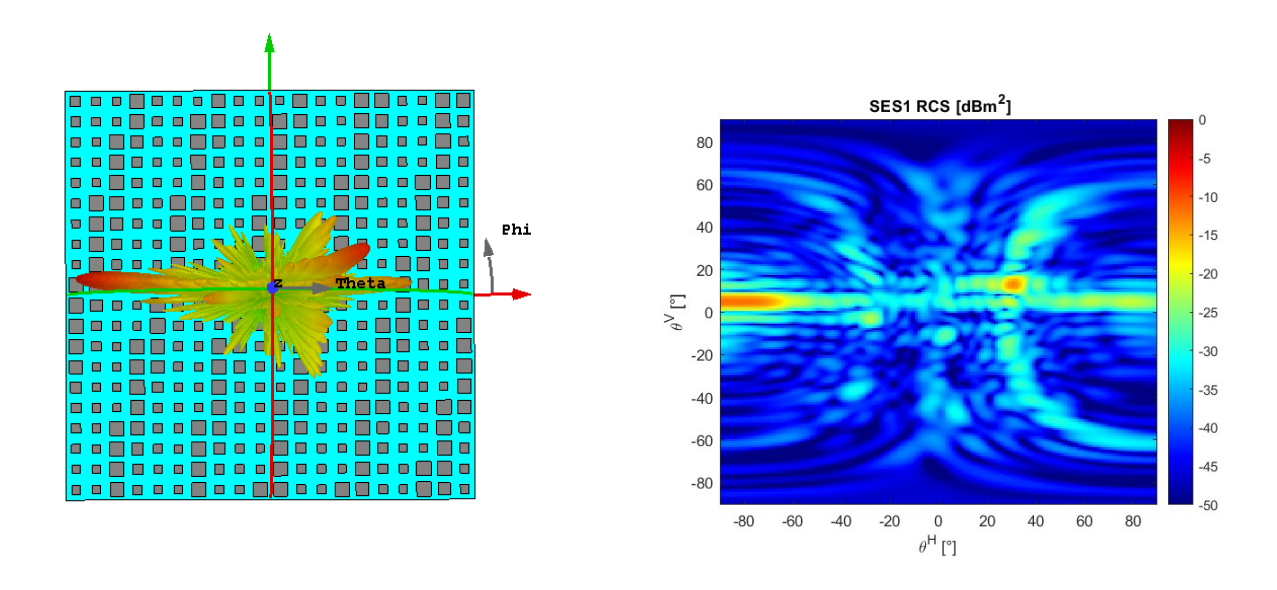


Figure 4.2.5: 3D far-field radiation pattern (left) and RCS map (right) of SES1.

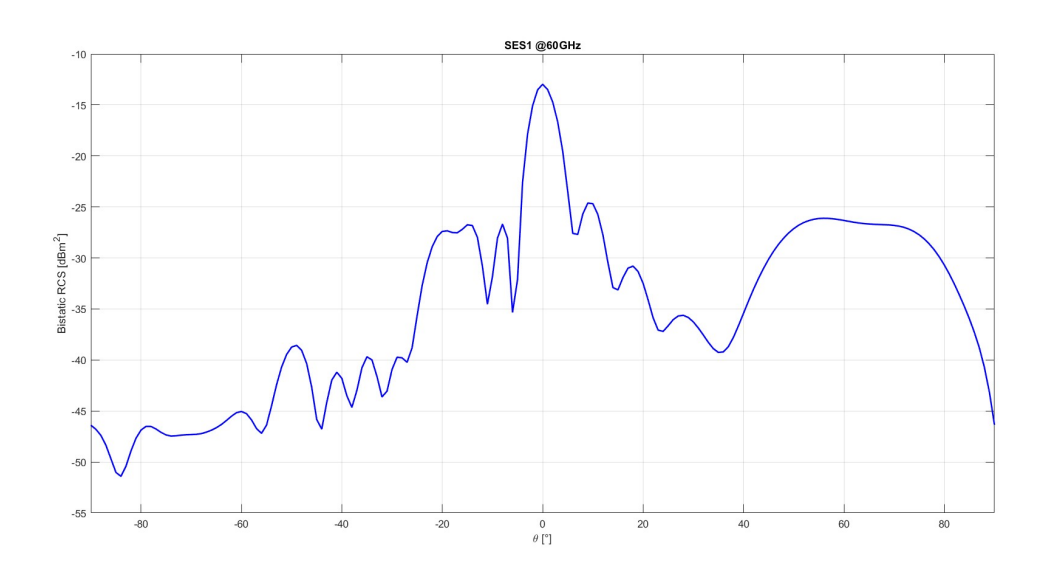


Figure 4.2.6: 2D RCS cuts of SES 1 far-field response

The 2D far-field cut has been extracted by aligning the reference system with the main lobe direction, i.e., by rotating the coordinate system so that the z-axis points along the maximum of the reflected beam. This choice allows for a clearer representation of the RCS levels around the main lobe and provides a direct comparison of side lobes with respect to the desired beam direction.

Looking at the SES1 layout, the distribution of patch widths varies smoothly according to the required phase profile. This variation confirms that the phase distribution has been properly translated into the physical geometry, without abrupt discontinuities

that could otherwise introduce additional scattering.

However, the far-field results show that the reflected beam does not perfectly match

the desired direction. This mismatch is likely due to the incidence angle of the in-

coming plane wave, which reduces the efficiency of the surface in pointing the beam.

Specifically, the reflected beam is observed at $\theta = 31^{\circ}$ instead of the target $\theta_b = 39^{\circ}$,

and at $\varphi = 13.5^{\circ}$ instead of the expected $\varphi_b = -20^{\circ}$. The relatively steep incidence of

the incoming plane wave (θ_I large and ϕ_I non-zero), combined with the wide angles

of the desired reflected beam, makes it challenging for the SES to uniformly compen-

sate the phase across the array and to redirect the beam accurately. As a result, the

beam steering does not perfectly reach the desired direction. Also the finite size of the

SES array introduces discretization effects, which inherently limit the precision of the

beam shaping and can lead to a shift in both azimuth and elevation of the main lobe.

Moreover, the reflected power is relatively low, with the main lobe reaching approxi-

mately -12dB, while the side lobes range from -25dB and lower, as highlighted in the

2D RCS cut. Another relevant effect is the presence of the specular reflection, which

remains significant, whereas it should ideally be strongly suppressed to maximize the

redirection efficiency.

Overall, SES 1 highlights the limitations imposed by very steep incidence angles: while

the design procedure is consistent, the surface struggles to efficiently steer the incoming

wave, leading to reduced gain, misalignment, and unwanted scattering.

4.2.2SES 2

Specifications

• Working frequency: 60GHz

• Cell size: $\frac{\lambda}{2}$

• Array dimension: 20×20

• Substrate thickness: 0.51mm

50

- Direction of arrival of the plane wave: $\theta_I=52^\circ,\,\varphi_I=-12^\circ$
- Desired direction of the reflected beam: $\theta_b = -1^{\circ}$, $\varphi_b = 0^{\circ}$

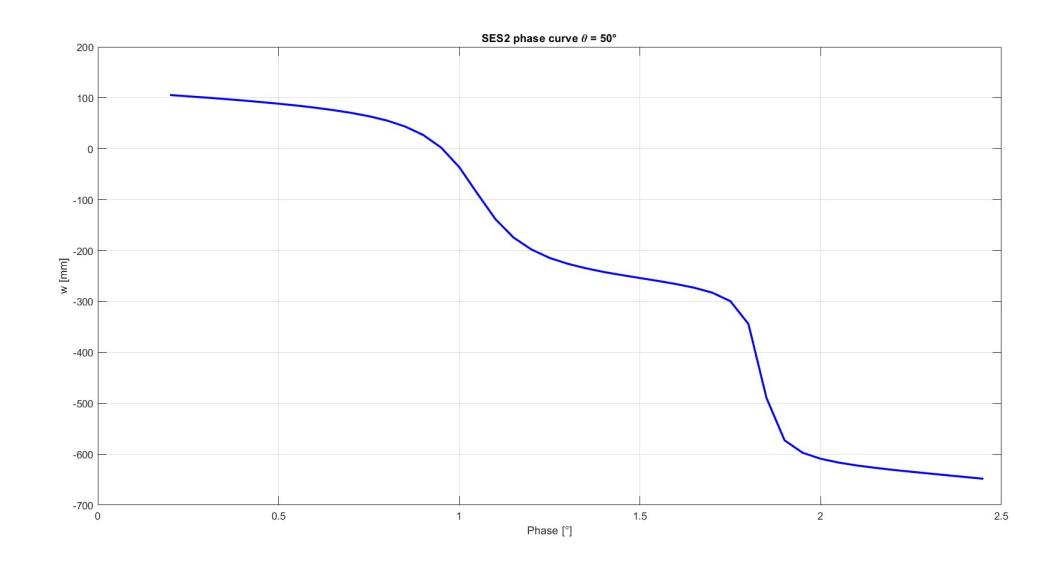


Figure 4.2.7: Phase curve used for the SES 2 design

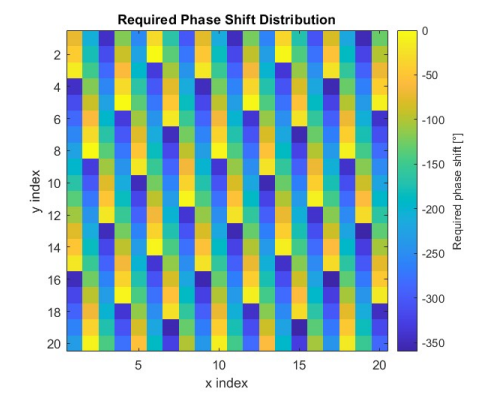


Figure 4.2.8: SES 2 Required phase distribution

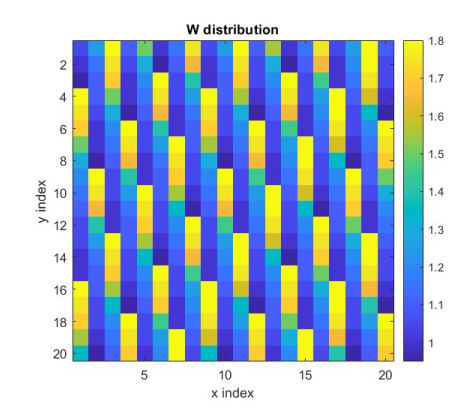


Figure 4.2.9: SES 2 Patch width distribution

The patch width distribution was used to create the SES 2 layout, which was subsequently imported into CST Microwave Studio as a DXF file for full-wave simulation.

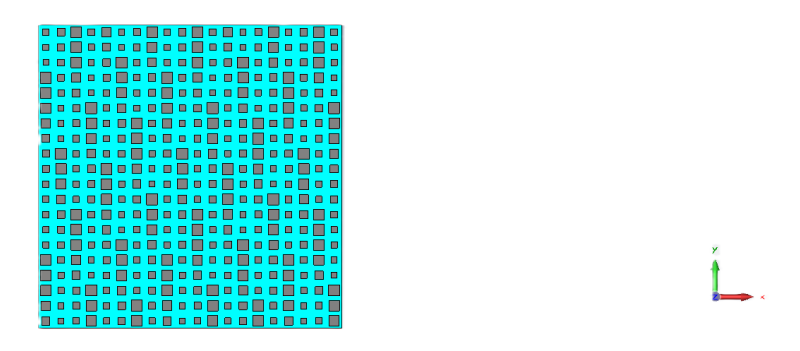


Figure 4.2.10: SES 2 layout

The simulation results are shown through the 3D far-field radiation pattern, providing an overall view of the reflected beam, and the 2D RCS cuts, which allow for a detailed assessment of the main lobe orientation and the levels of side lobes.

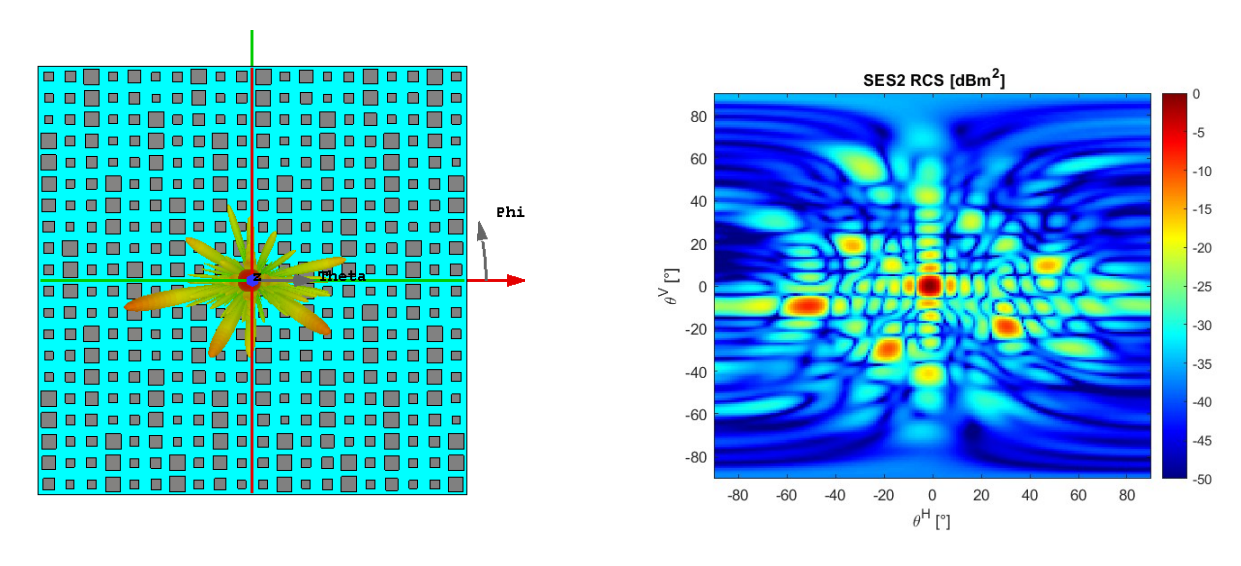


Figure 4.2.11: 3D far-field radiation pattern (left) and RCS map (right) of SES2.

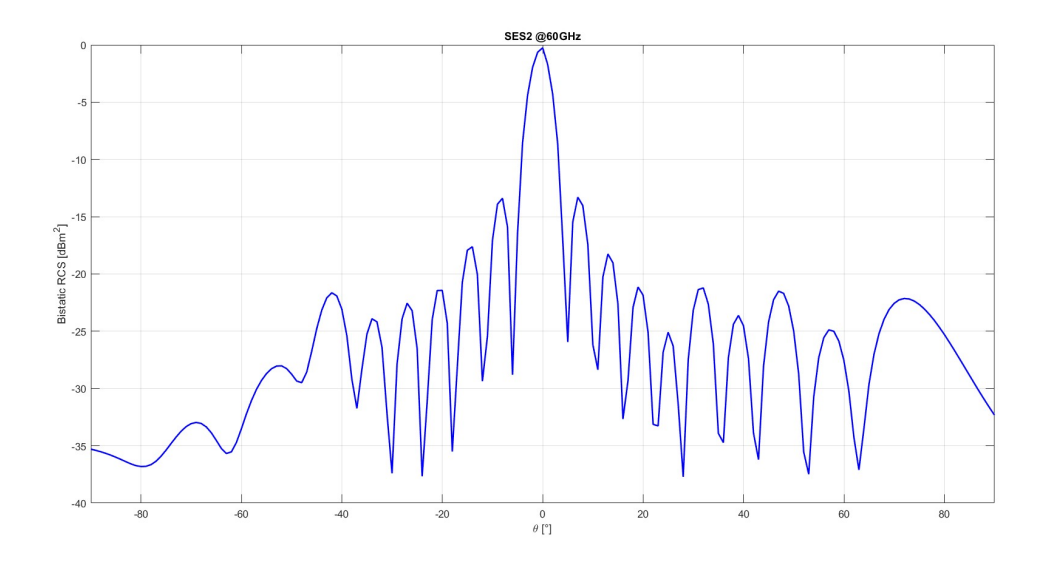


Figure 4.2.12: 2D RCS cuts of SES 2 far-field response

From the far-field results of SES 2, it can be observed that the reflected beam is properly redirected towards the desired direction, confirming the effectiveness of the design. The main lobe reaches a maximum level of approximately 0 dB, while the side lobes are about -12dB, ensuring a clear distinction between the desired reflection and unwanted scattering. Compared to SES 1, this configuration demonstrates a more accurate beam steering and higher efficiency in terms of reflected power.

Looking at the layout, the patch width distribution shows coherence with the required phase distribution. This smooth variation confirms that the phase distribution has been properly translated into the physical geometry, without abrupt discontinuities that could otherwise introduce additional scattering.

4.2.3 SES 3

Specifications

• Working frequency: 60GHz

• Cell size: $\frac{\lambda}{2}$

• Array dimension: 20×20

• Substrate thickness: 0.51mm

- Direction of arrival of the plane wave: $\theta_I = 42^{\circ}$, $\varphi_I = 8^{\circ}$
- Desired direction of the reflected beam: $\theta_b = -34^{\circ}$, $\varphi_b = -23^{\circ}$

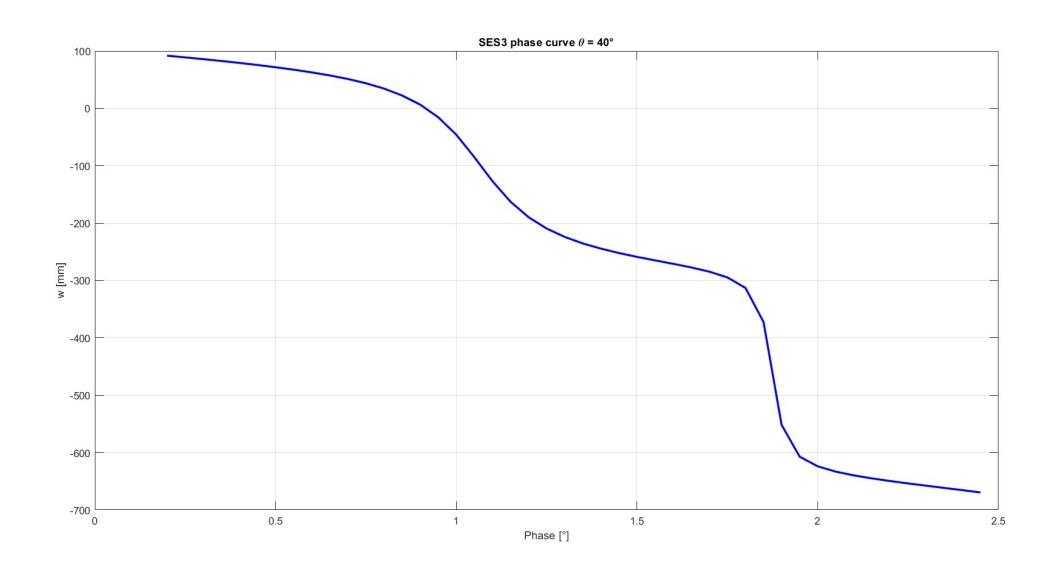


Figure 4.2.13: Phase curve used for the SES 3 design

The phase curve adopted for SES 3 was exploited up to a patch width of w = 1.9 mm. Beyond this value, the curve becomes excessively steep, which would have increased the sensitivity to discretization and could have led to inaccuracies or errors in the layout generation.

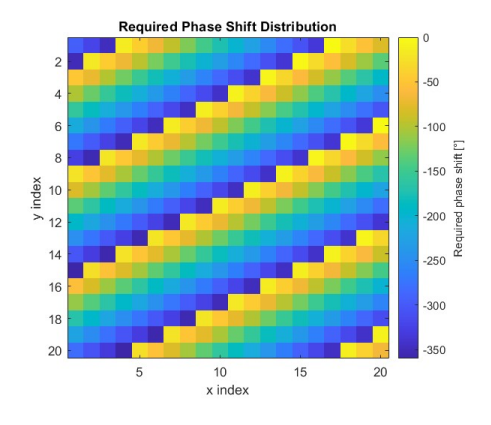


Figure 4.2.14: SES 3 Required phase distribution

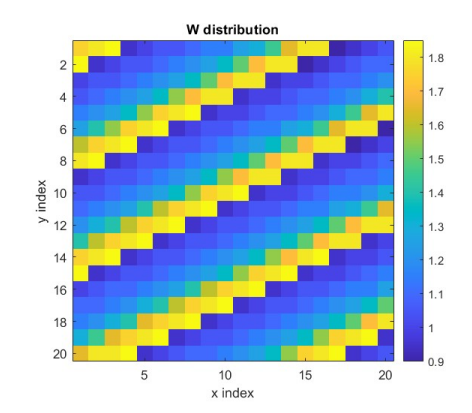


Figure 4.2.15: SES 3 Patch width distribution

From the computed width variation, the SES 3 layout was constructed and implemented in CST for subsequent full-wave simulations.

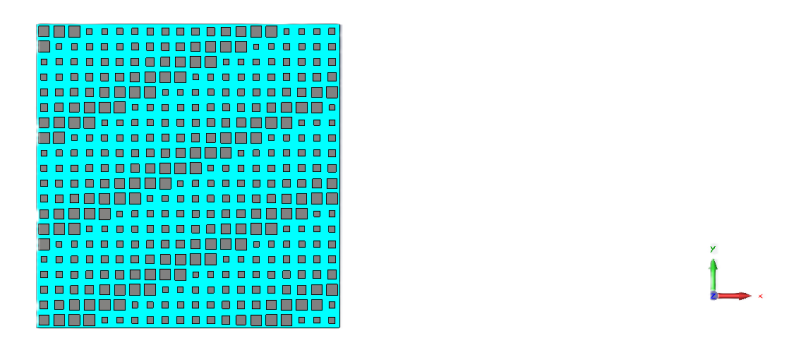


Figure 4.2.16: SES 3 layout

The results are illustrated through both 3D far-field plots, which highlight the overall beam redirection, and 2D RCS sections, useful for quantifying the main and secondary lobes.

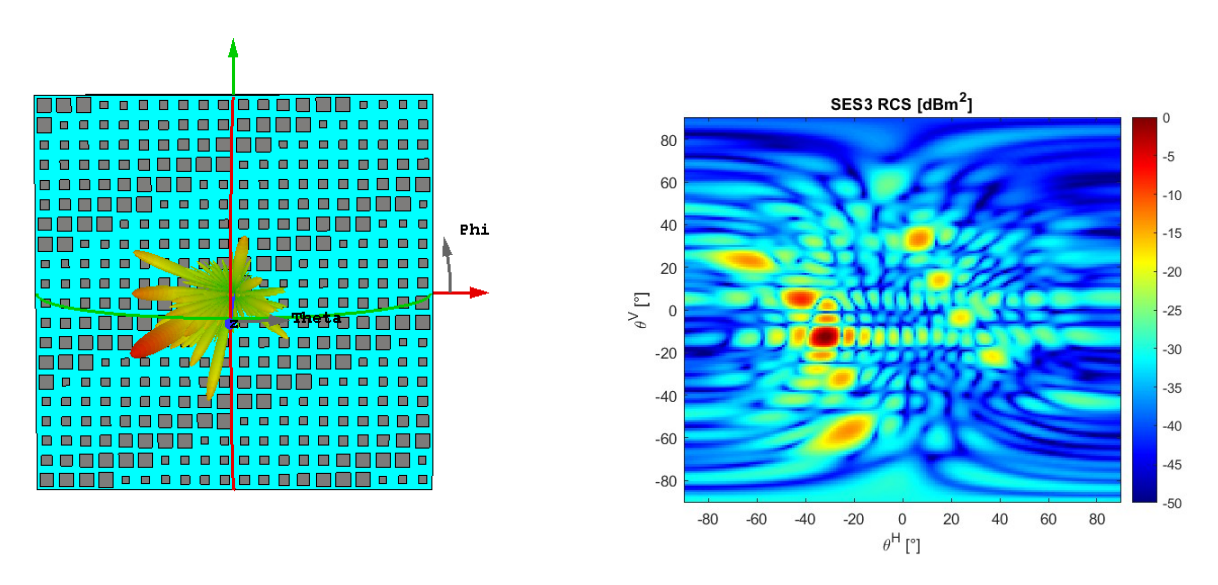


Figure 4.2.17: 3D far-field radiation pattern (left) and RCS map (right) of SES3.

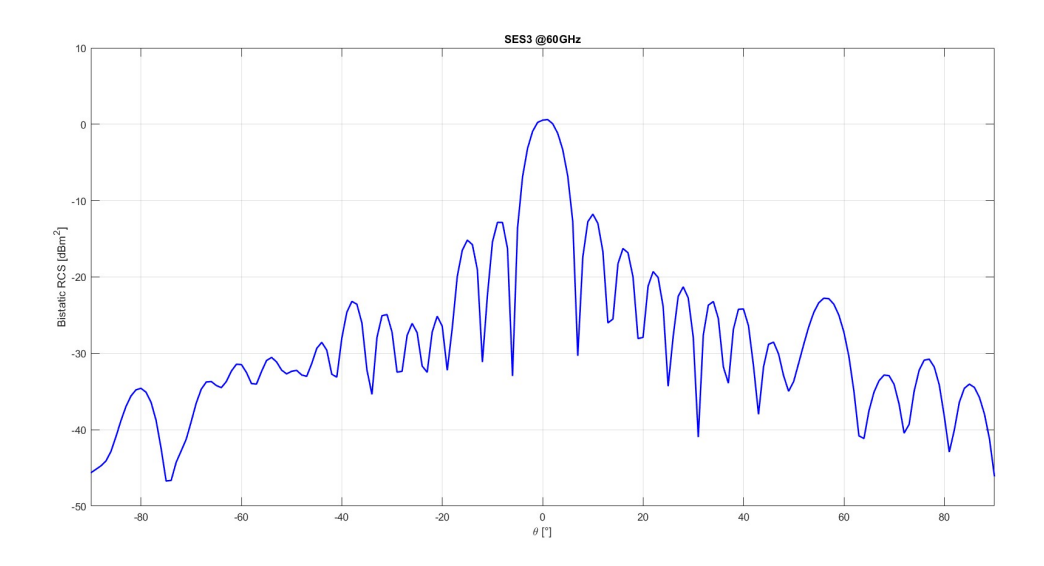


Figure 4.2.18: 2D RCS cuts of SES 3 far-field response

The far-field analysis of SES 3 highlights that the reflected beam is accurately steered towards the intended direction, demonstrating the validity of the design approach. The main lobe exhibits a peak value close to 1dB, whereas the side lobes remain suppressed around -12dB, which guarantees a good separation between the desired reflection and spurious components.

4.2.4 SES 4

Specifications

• Working frequency: 60GHz

• Cell size: $\frac{\lambda}{2}$

• Array dimension: 20×20

• Substrate thickness: 0.51mm

• Direction of arrival of the plane wave: $\theta_I=20^\circ,\,\varphi_I=-18^\circ$

• Desired direction of the reflected beam: $\theta_b = -50^{\circ}$, $\varphi_b = 0^{\circ}$

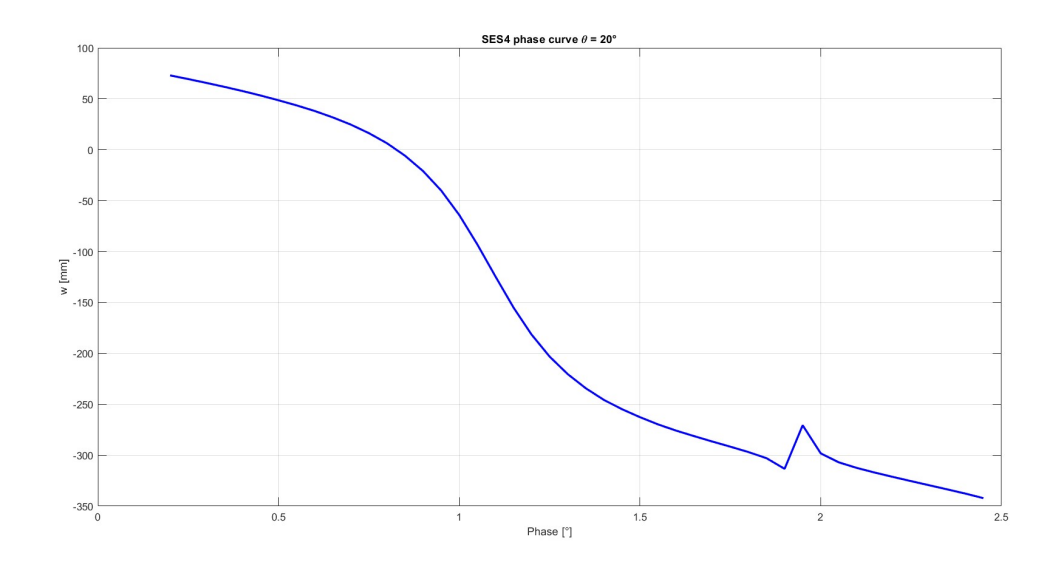


Figure 4.2.19: Phase curve used for the SES 4 design

For SES 4, the phase curve exhibits a spike near w = 1.95 mm. To avoid potential instabilities during the layout generation, the design was limited to a maximum patch width of 1.9 mm, ensuring a smoother and more reliable implementation.

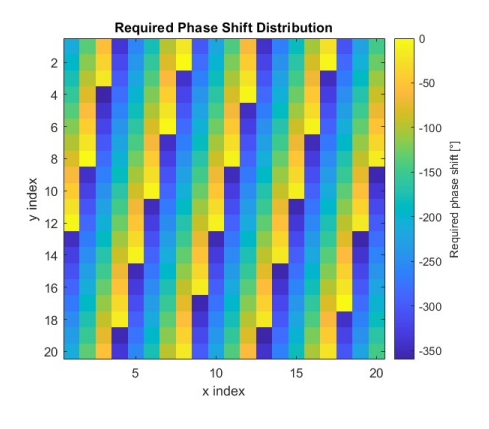


Figure 4.2.20: SES 4 Required phase distribution

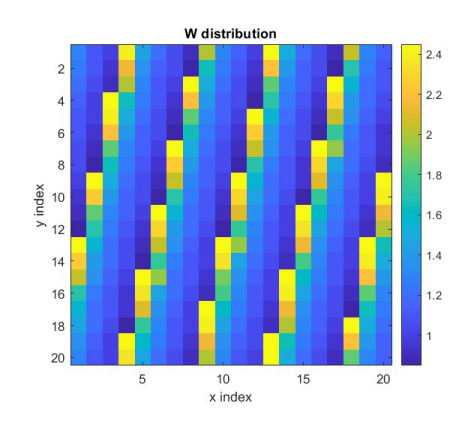


Figure 4.2.21: SES 4 Patch width distribution

The layout corresponding to SES 4 was derived from the width distribution and then modeled in CST Microwave Studio through a DXF import for electromagnetic simulation.

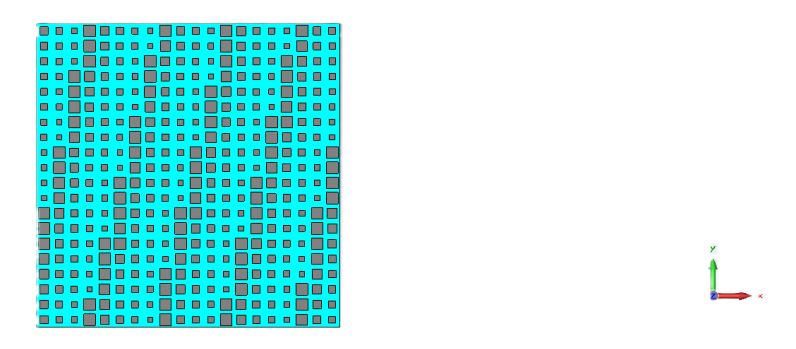


Figure 4.2.22: SES 4 layout

To assess the electromagnetic behavior, both 3D far-field maps and 2D RCS cuts are presented, offering complementary perspectives on the reflected beam and scattering levels.

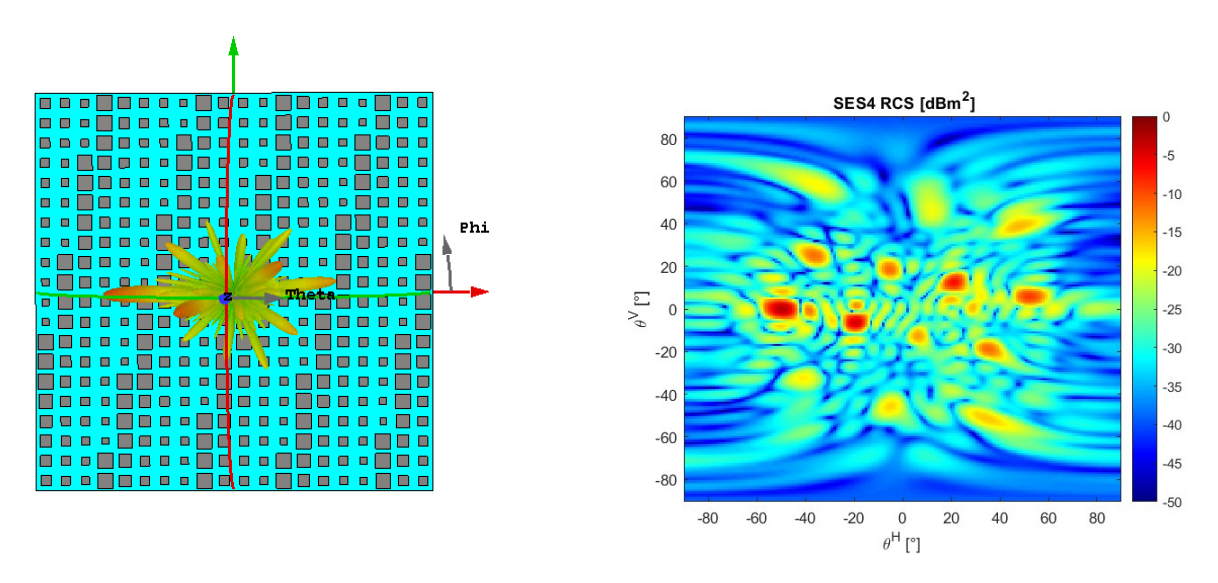


Figure 4.2.23: 3D far-field radiation pattern (left) and RCS map (right) of SES4.

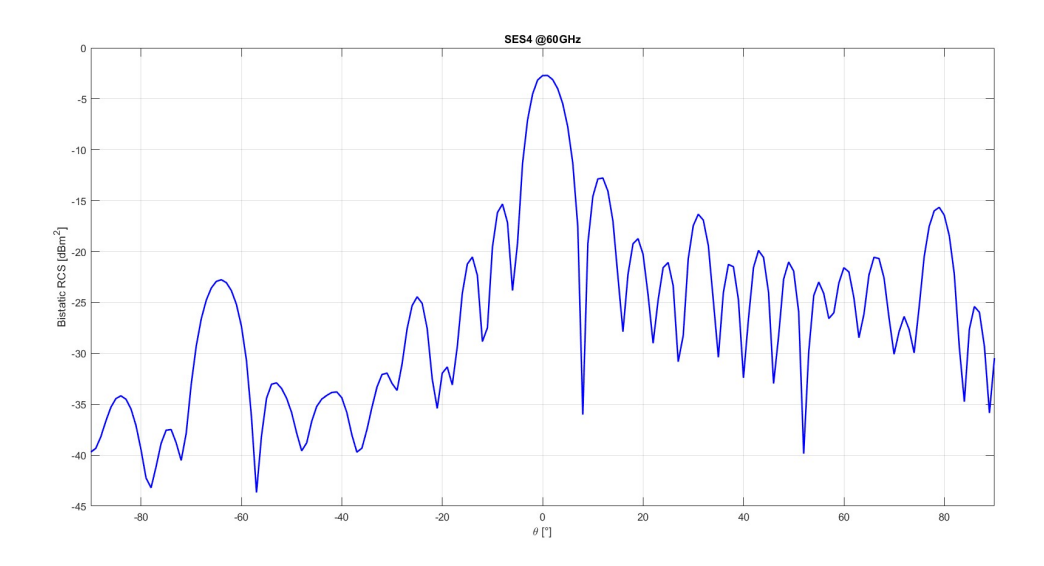


Figure 4.2.24: 2D RCS cuts of SES 4 far-field response

From the far-field results of SES 4, it can be observed that the main lobe is properly steered towards the desired direction. However, compared to previous surfaces, a larger number of side lobes appear, with a power difference of approximately 10 dB relative to the main lobe (main lobe at about -3 dB, side lobes around -13 dB).

The increase in side lobes is mainly due to the truncation of the phase curve at w=1.9 mm. By limiting the phase variation, the SES cannot perfectly reproduce the desired phase profile across the array, which causes part of the energy to spread into undesired directions. As a result, the main lobe power decreases compared to the other SESs, while the side lobes rise, reducing the contrast between the main reflection and the scattered energy. This behavior can be problematic for localization applications, where a clearly dominant main lobe is required. If the side lobes are comparable in power to the main reflection, it becomes more difficult to unambiguously identify the intended illuminated region, potentially reducing the accuracy of the localization system.

4.2.5 SES 5

Specifications

• Working frequency: 60GHz

• Cell size: $\frac{\lambda}{2}$

• Array dimension: 20×20

• Substrate thickness: 0.51mm

• Direction of arrival of the plane wave: $\theta_I = -3^{\circ}, \ \varphi_I = 9^{\circ}$

• Desired direction of the reflected beam: $\theta_b = -61^\circ, \, \varphi_b = -12^\circ$

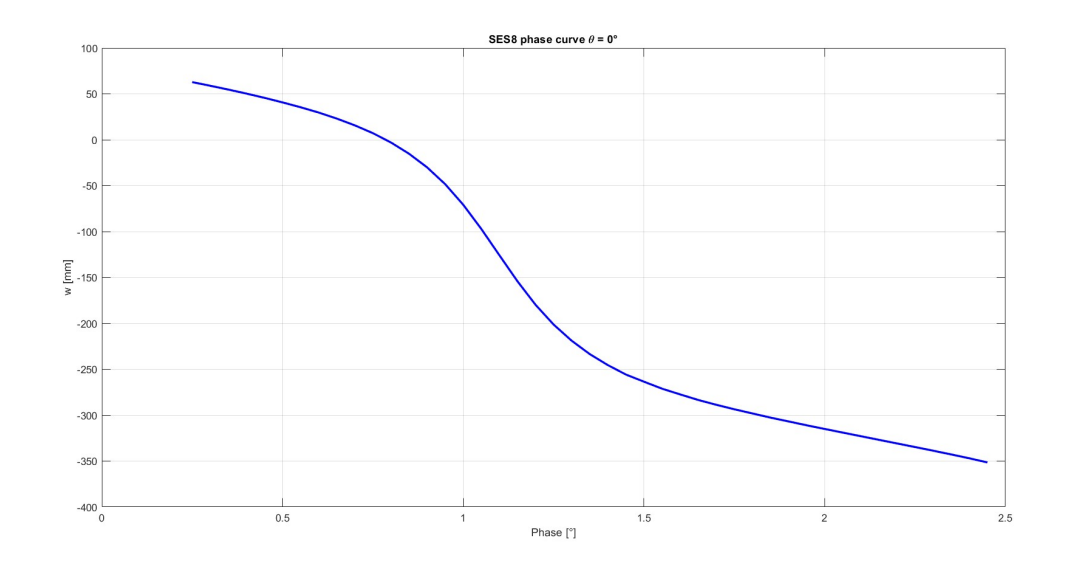


Figure 4.2.25: Phase curve used for the SES 5 design

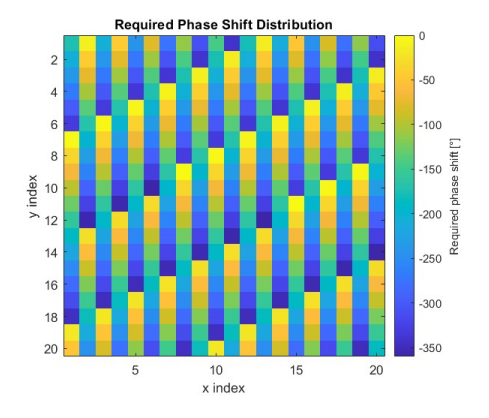


Figure 4.2.26: SES 5 Required phase distribution

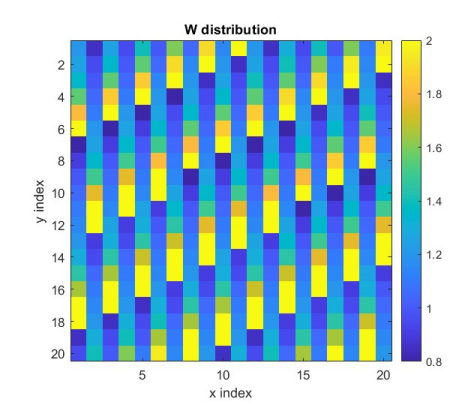


Figure 4.2.27: SES 5 Patch width distribution

The SES 5 layout was obtained from the calculated patch width distribution and subsequently implemented in CST Microwave Studio by importing it as a DXF file for full-wave analysis.

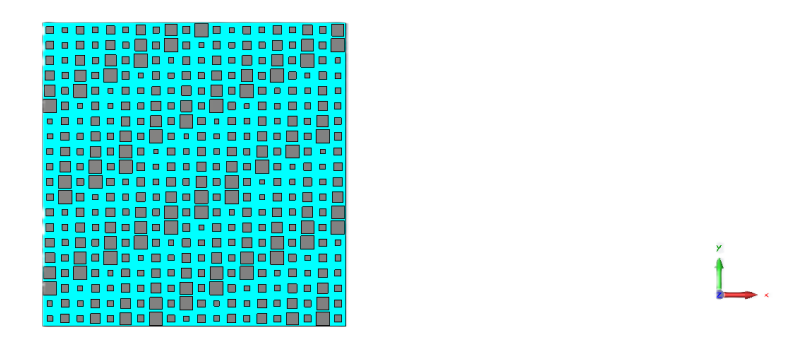


Figure 4.2.28: SES 5 layout

The electromagnetic performance is evaluated through 3D far-field patterns and 2D RCS cuts, providing a comprehensive view of the reflected beam and the associated scattering characteristics.

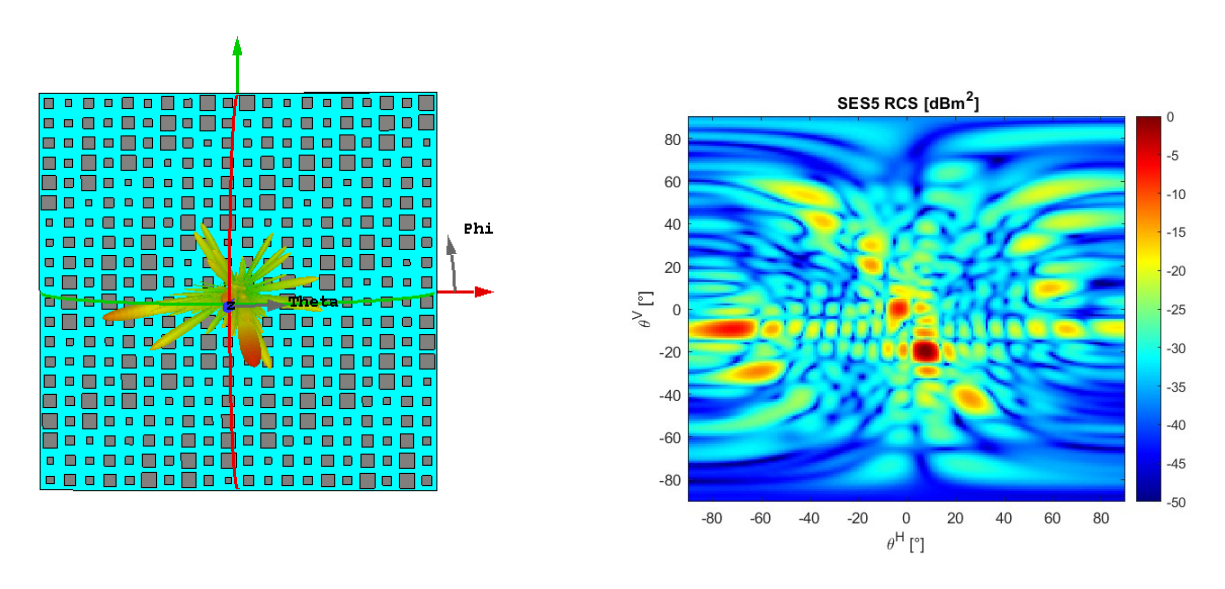


Figure 4.2.29: 3D far-field radiation pattern (left) and RCS map (right) of SES5.

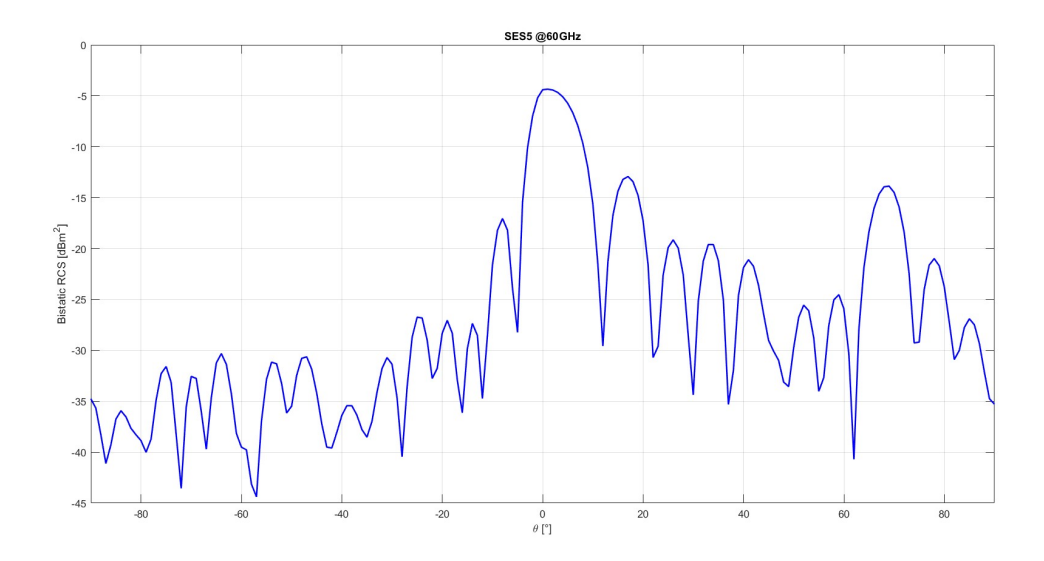


Figure 4.2.30: 2D RCS cuts of SES 5 far-field response

For SES 5, the reflected beam points in the desired direction, but a noticeable specular component along the incident plane wave is also present. This is likely because the reflection angle is very wide ($\theta_b = -62^{\circ}$), making it harder for the surface to focus all the energy into the intended beam. Consequently, the RCS in the specular direction reaches about -5 dB, lower than the main lobes of the other SESs, showing how some energy spreads due to the extreme steering.

4.2.6 SES 6

Specifications

• Working frequency: 60GHz

• Cell size: $\frac{\lambda}{2}$

• Array dimension: 20×20

• Substrate thickness: 0.51mm

• Direction of arrival of the plane wave: $\theta_I=64^\circ,\,\varphi_I=6^\circ$

• Desired direction of the reflected beam: $\theta_b = 28^{\circ}, \, \varphi_b = -14^{\circ}$

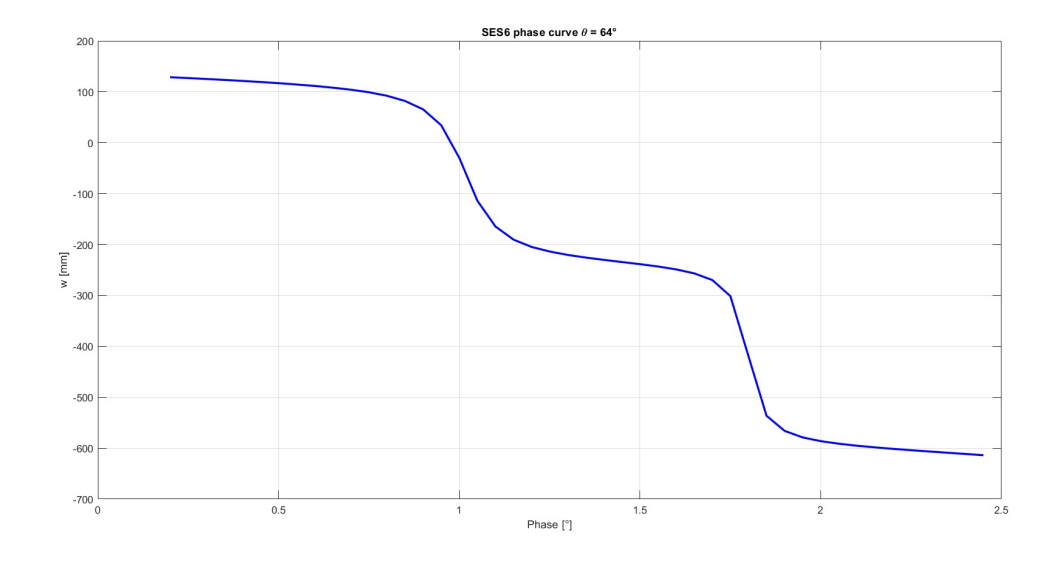


Figure 4.2.31: Phase curve used for the SES 6 design

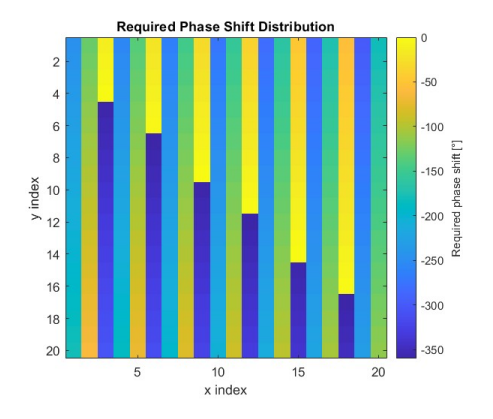


Figure 4.2.32: SES 6 Required phase distribution

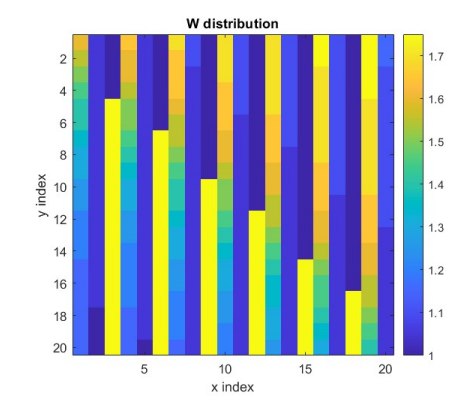


Figure 4.2.33: SES 6 Patch width distribution

The patch width distribution was translated into the SES 6 layout, which was then imported into CST Microwave Studio as a DXF file for full-wave simulations.

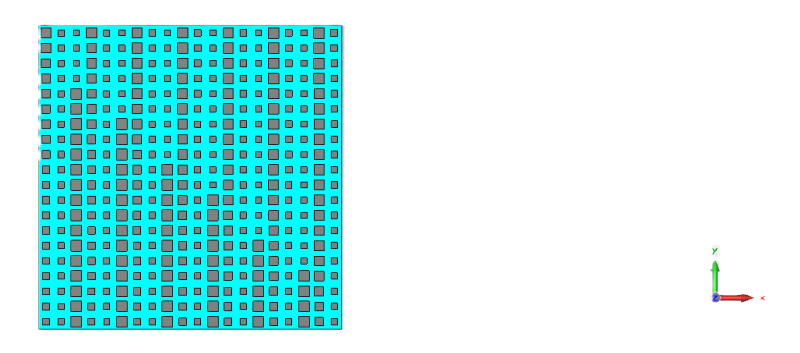


Figure 4.2.34: SES 6 layout

The simulation outputs include the 3D far-field radiation pattern, offering a comprehensive visualization of the reflected beam, along with 2D RCS cuts that enable a precise evaluation of the main lobe direction and the magnitude of the side lobes.

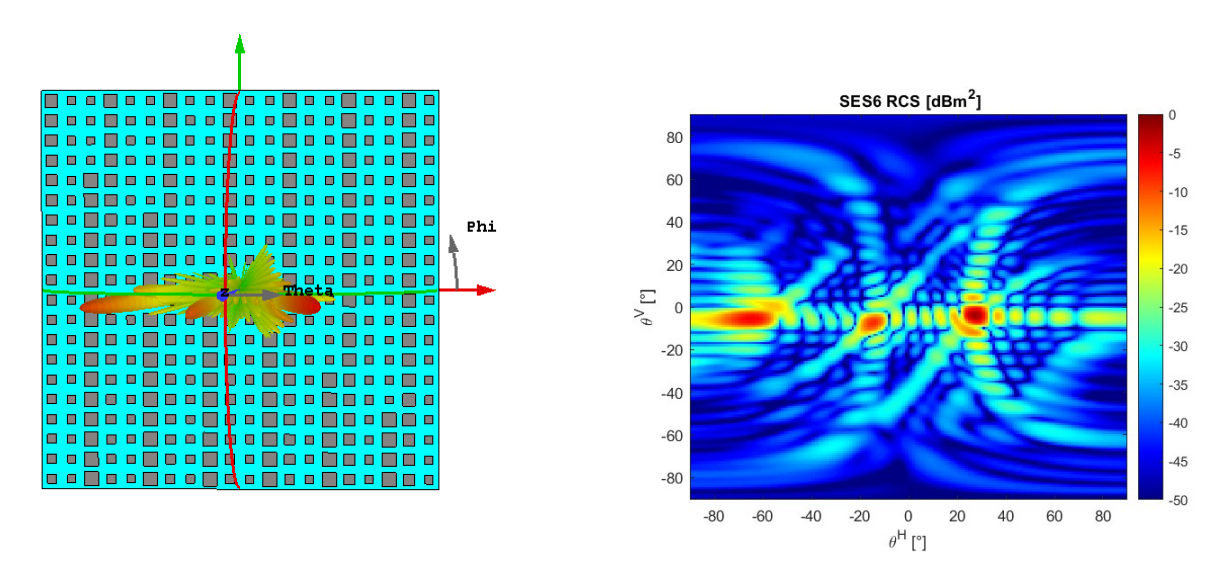


Figure 4.2.35: 3D far-field radiation pattern (left) and RCS map (right) of SES6.

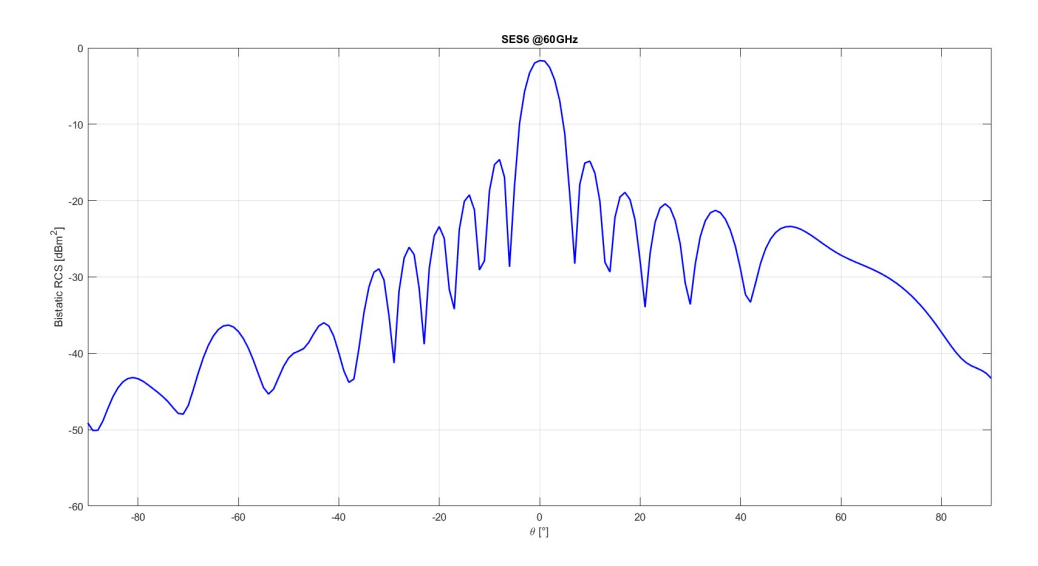


Figure 4.2.36: 2D RCS cuts of SES 6 far-field response

In this case as well, the main lobe is correctly directed towards the desired angle, reaching approximately -1 dB, while the side lobes are around -17 dB. The specular reflection corresponding to the incident plane wave is more pronounced, and an additional lobe symmetric to the main lobe is also visible. Unlike SES 1, where a similar incidence angle caused some inefficiencies, here the incidence differs enough that no significant issues are observed in the beam steering performance.

4.2.7 SES 7

Specifications

• Working frequency: 60GHz

• Cell size: $\frac{\lambda}{2}$

• Array dimension: 20×20

• Substrate thickness: 0.51mm

• Direction of arrival of the plane wave: $\theta_I=42^\circ,\,\varphi_I=12^\circ$

• Desired direction of the reflected beam: $\theta_b = -23^{\circ}$, $\varphi_b = -15^{\circ}$

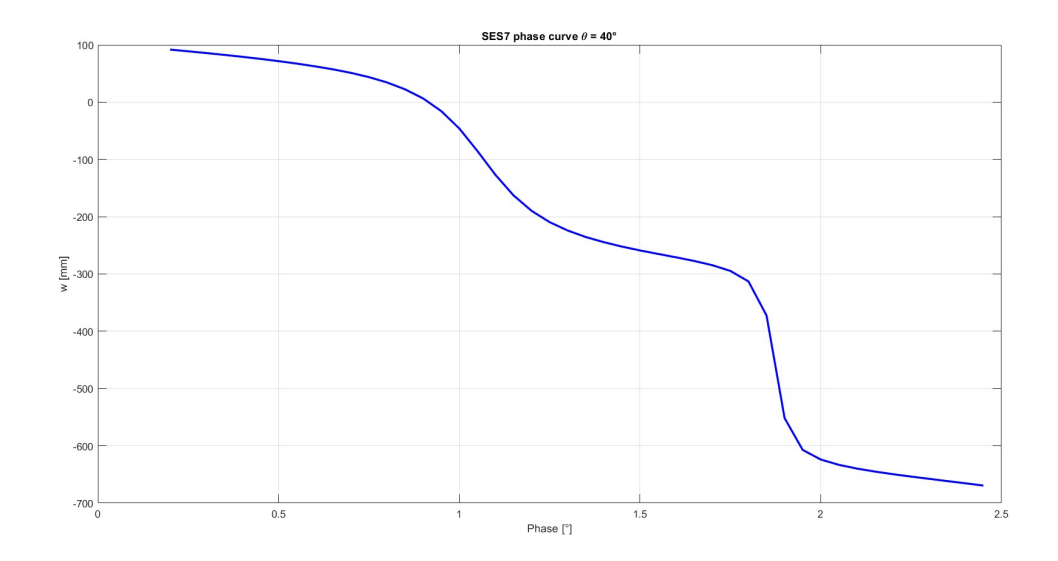


Figure 4.2.37: Phase curve used for the SES 7 design

For SES 7, the same phase curve used for SES 3 was applied, limiting the patch width to w=1.9 mm. Beyond this point, the curve becomes too steep, which would have increased sensitivity to discretization and could have caused errors or inaccuracies in the layout design.

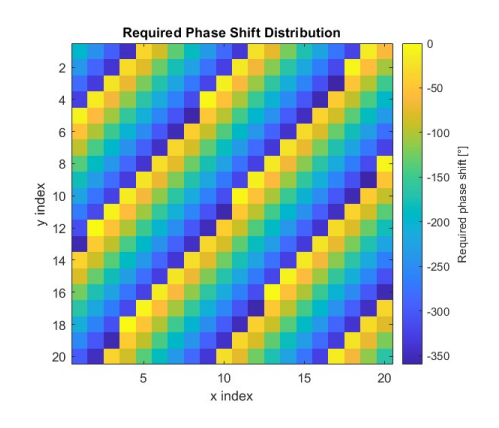


Figure 4.2.38: SES 7 Required phase distribution

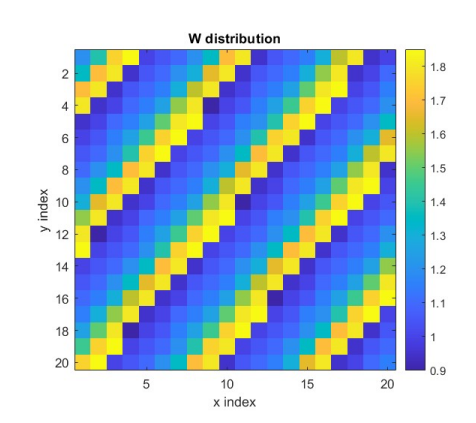


Figure 4.2.39: SES 7 Patch width distribution

The SES 7 layout was generated from the patch width distribution and then imported into CST Microwave Studio as a DXF file for full-wave simulations.

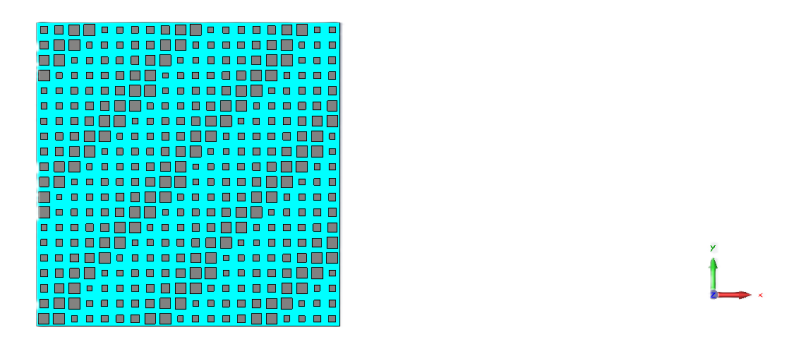


Figure 4.2.40: SES 7 layout

The outcomes are presented with a 3D far-field radiation pattern, offering a complete visualization of the reflected beam, along with 2D RCS cuts to closely examine the main lobe direction and the intensity of the side lobes.

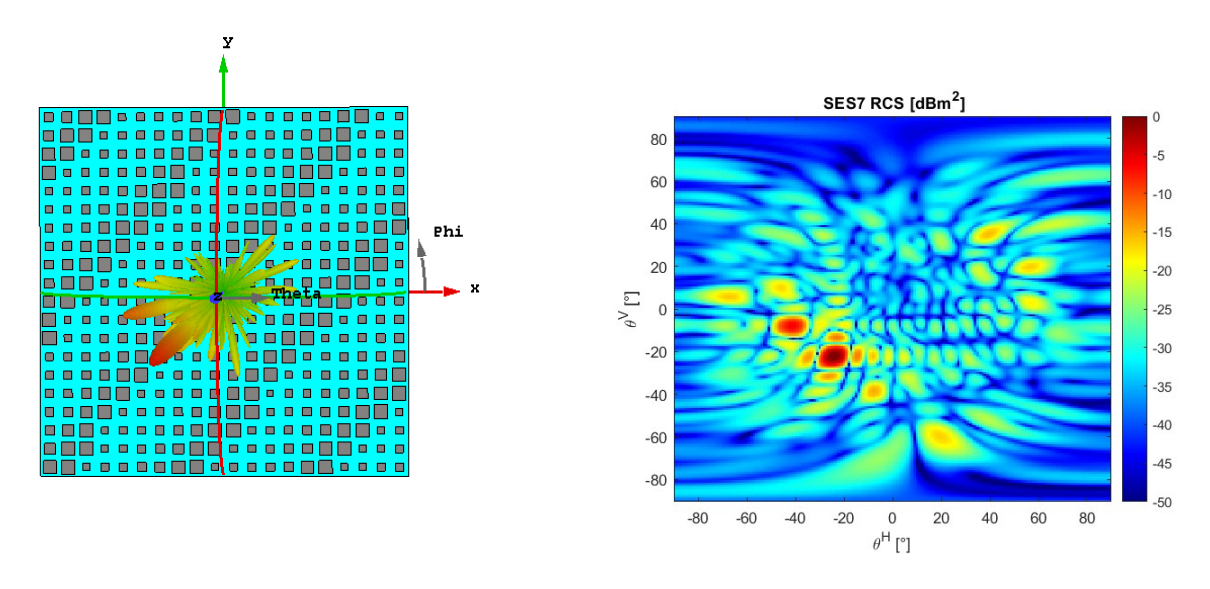


Figure 4.2.41: 3D far-field radiation pattern (left) and RCS map (right) of SES7.

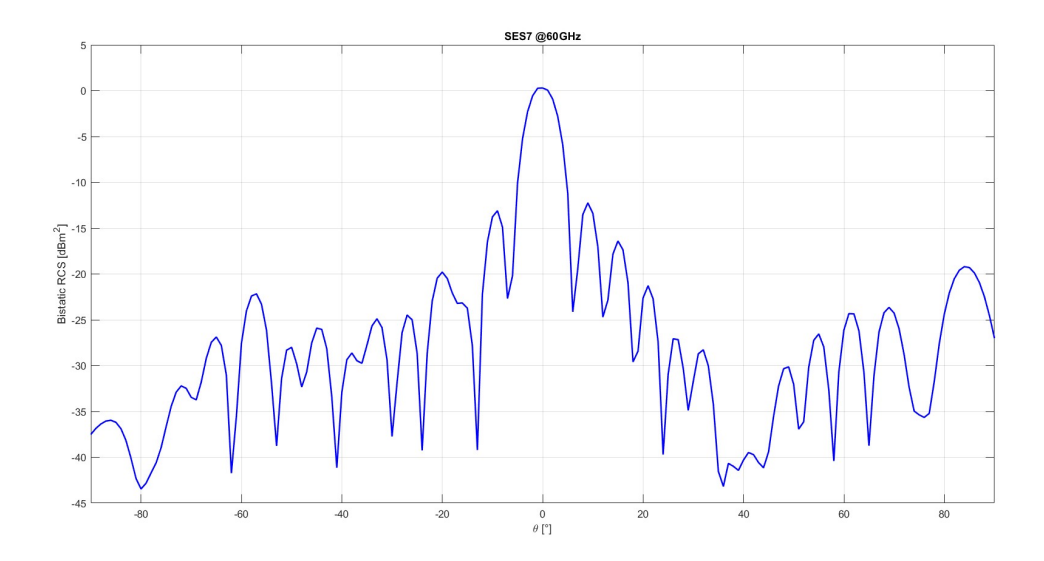


Figure 4.2.42: 2D RCS cuts of SES 7 far-field response

From the simulation results, it can be observed that the main lobe of SES 7 reaches approximately 0 dB, while the side lobes are around -13 dB. The reflected beam is correctly directed towards the desired angle. As in previous cases, a weaker lobe appears in the direction specular to the incident plane wave.

4.2.8 SES 8

Specifications

• Working frequency: 60GHz

• Cell size: $\frac{\lambda}{2}$

• Array dimension: 20×20

• Substrate thickness: 0.51mm

 \bullet Direction of arrival of the plane wave: $\theta_I=20^\circ,\,\varphi_I=-15^\circ$

• Desired direction of the reflected beam: $\theta_b = -41^{\circ}, \, \varphi_b = 1^{\circ}$

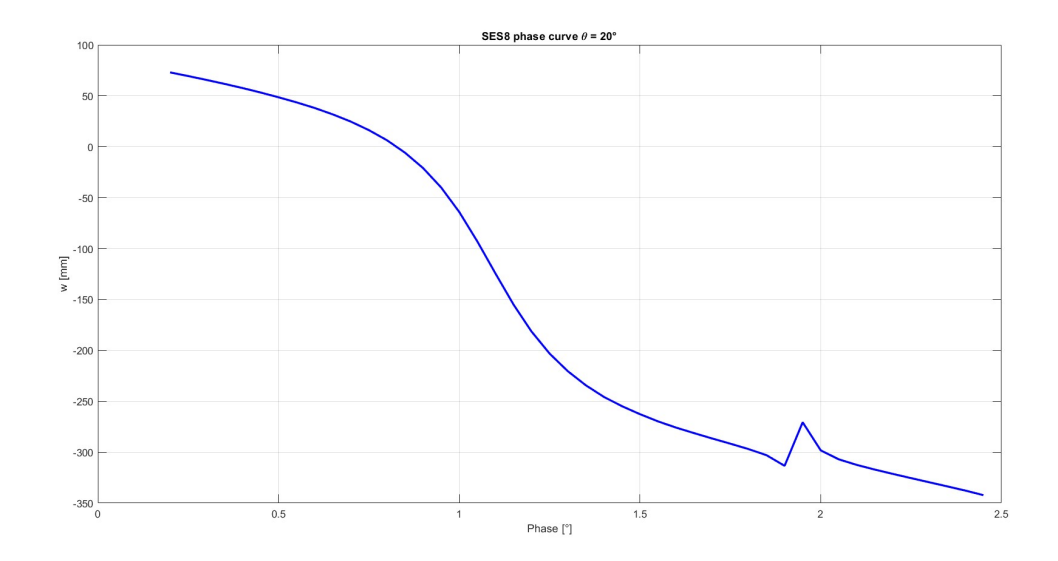


Figure 4.2.43: Phase curve used for the SES 8 design

SES 8 uses the same phase curve as SES 4, so the same considerations apply: the patch width was limited to a maximum of 1.9 mm to avoid instabilities during layout generation and to ensure a smooth and reliable implementation.

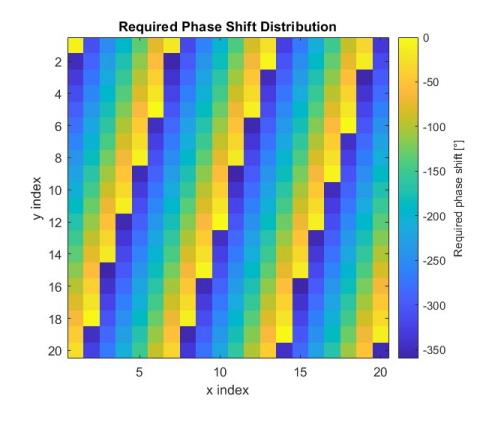


Figure 4.2.44: SES 8 Required phase distribution

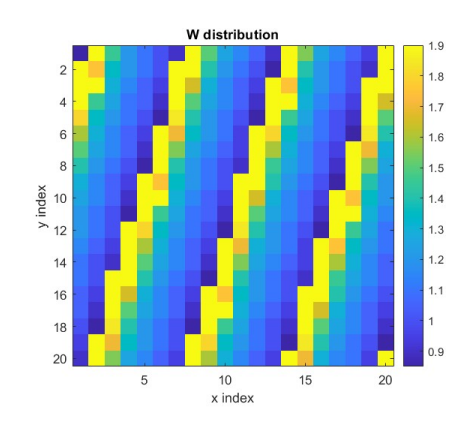


Figure 4.2.45: SES 8 Patch width distribution

The patch width distribution was used to create the SES 8 layout, which was subsequently imported into CST Microwave Studio as a DXF file for full-wave simulation.

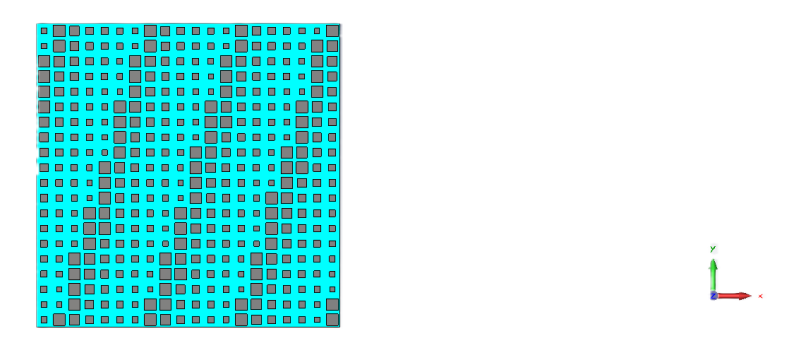


Figure 4.2.46: SES 8 layout

The simulation results are shown through the 3D far-field radiation pattern, providing an overall view of the reflected beam, and the 2D RCS cuts, which allow for a detailed assessment of the main lobe orientation and the levels of side lobes.

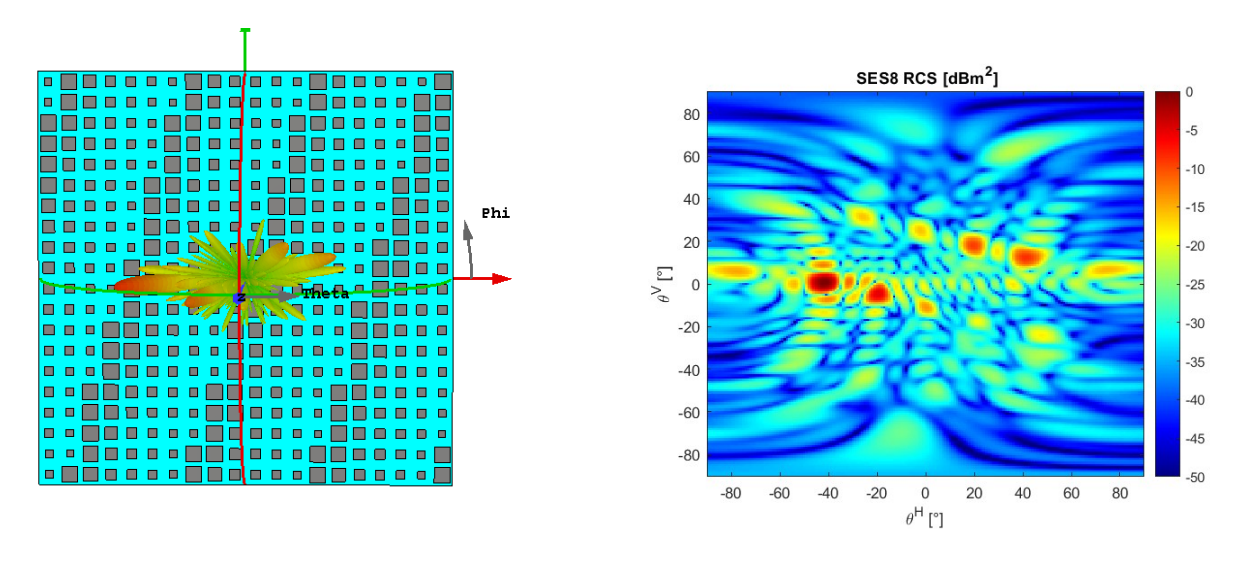


Figure 4.2.47: 3D far-field radiation pattern (left) and RCS map (right) of SES8.

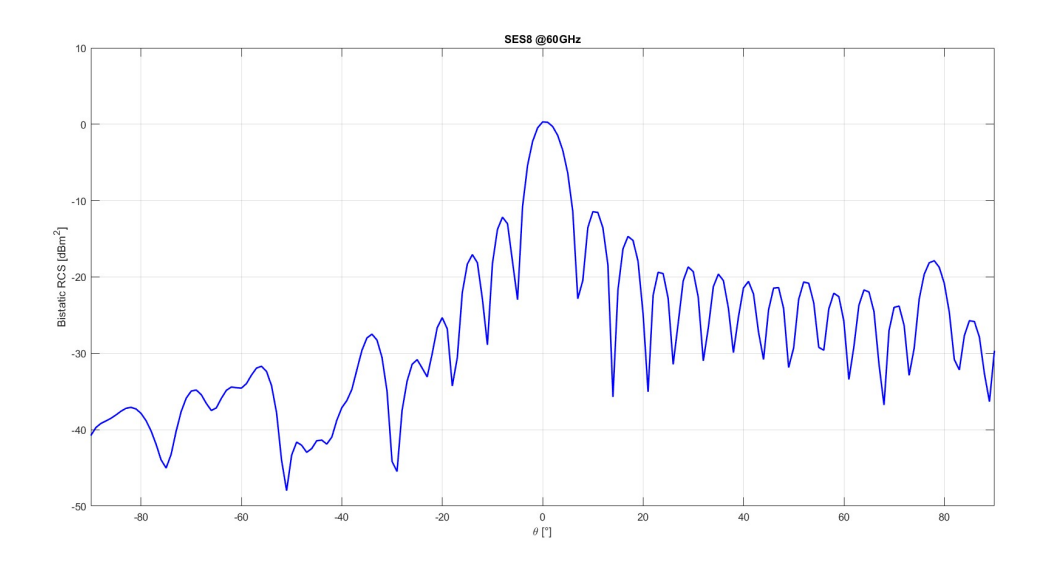


Figure 4.2.48: 2D RCS cuts of SES 8 far-field response

As with the previous surfaces, SES 8 successfully redirects the beam towards the desired direction. The layout exhibits the usual repetitive pattern, and the main lobe reaches approximately 0 dB, with side lobes around -13 dB. The specular lobe is still present but weaker compared to the main reflection.

4.3 Frequency Response of SESs

After analysing the SESs at the design frequency of 60 GHz, each surface is simulated across the frequency band 58–62 GHz to evaluate its behaviour. This allows assessing the robustness of the reflection performance and the effect of frequency variations on the main lobe direction, side lobes, and specular reflections. The following analysis compares the stability of each SES by observing changes in main lobe power, side lobe levels, and specular reflection.

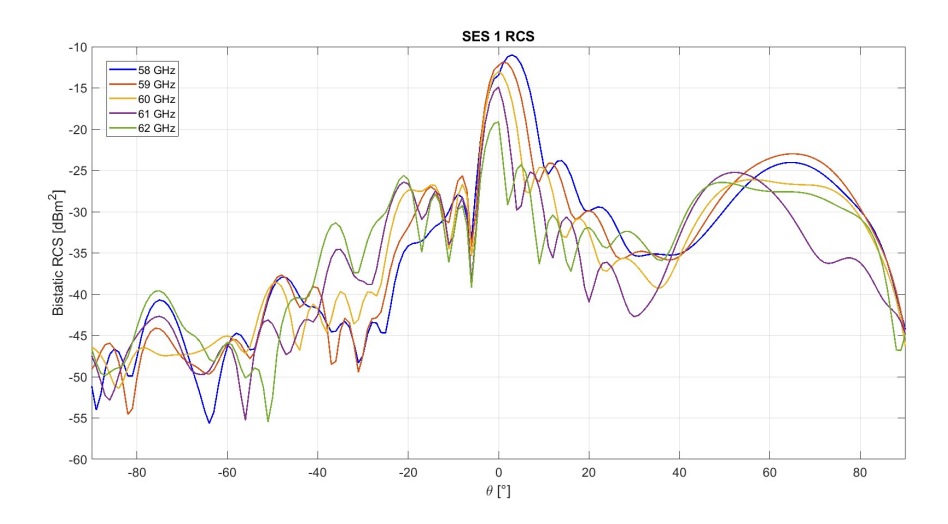


Figure 4.3.1: RCS cut of SES1 for multiple frequencies around the design value of 60GHz.

For SES1, at the lower frequency (58GHz) the main lobe slightly deviates from the target direction; at higher frequencies (59–62GHz) it aligns with the intended direction but gradually decreases in power. Side lobes become more pronounced, and the specular reflection increases significantly.

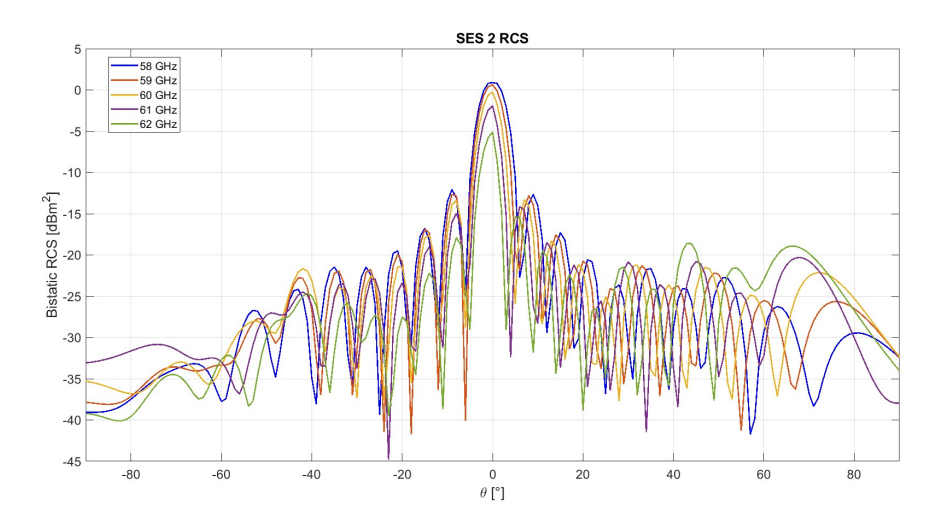


Figure 4.3.2: RCS cut of SES2 for multiple frequencies around the design value of 60GHz.

For SES2, the main lobe decreases in power as frequency increases, and side lobes grow more pronounced. However, the pointing direction of the main lobe remains essentially unchanged, indicating better robustness to frequency variations compared to SES1.

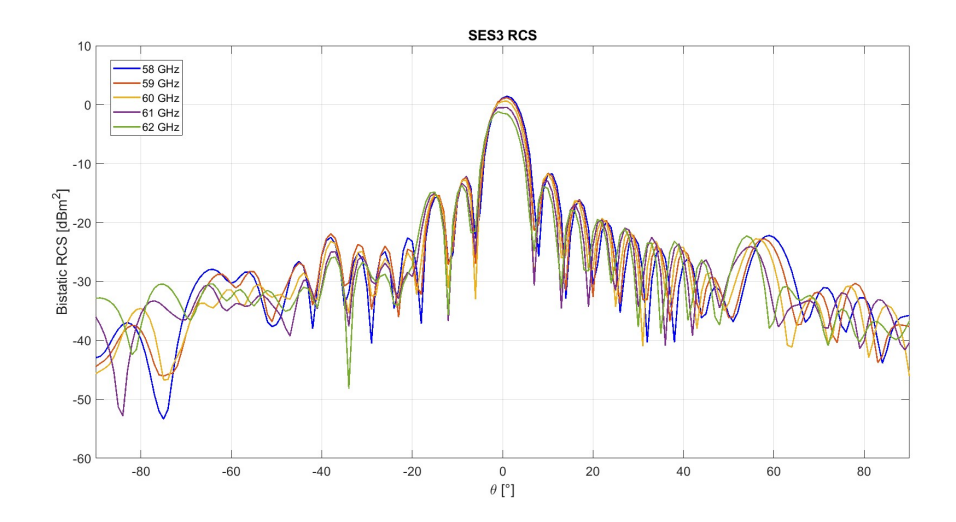


Figure 4.3.3: RCS cut of SES3 for multiple frequencies around the design value of 60GHz.

SES3 shows only a minimal reduction of the main lobe across the frequency range, while the side lobes remain nearly constant in amplitude. The main lobe pointing direction is stable, indicating an essentially robust response from 58GHz to 62GHz.

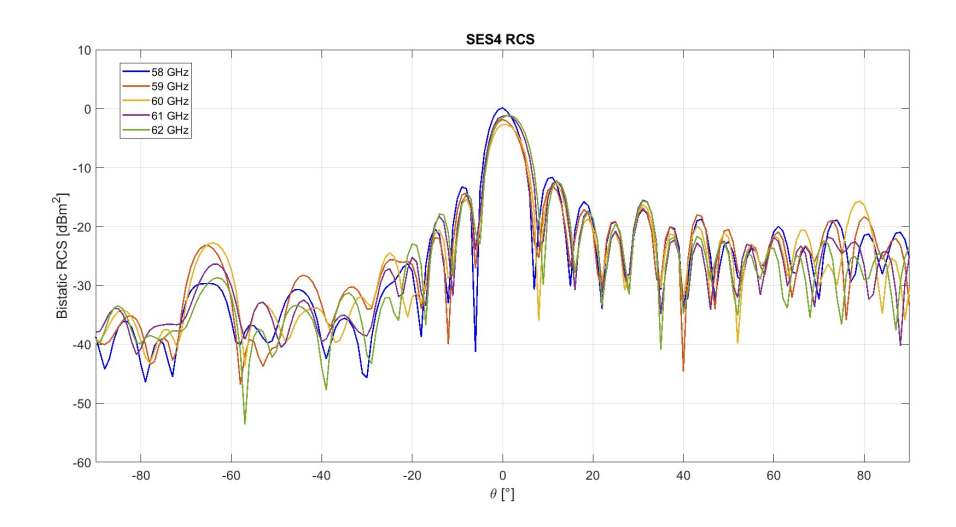


Figure 4.3.4: RCS cut of SES4 for multiple frequencies around the design value of 60GHz.

SES4 exhibits similar behaviour to SES3: the main lobe decreases only slightly in power, side lobes remain almost unchanged, and the main lobe direction stays stable. The reflection performance is robust across the analysed frequency range.

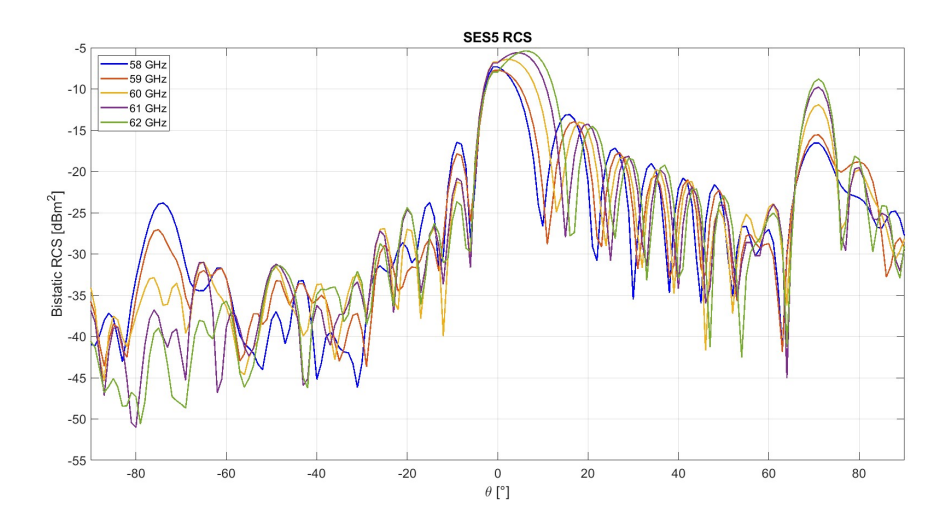


Figure 4.3.5: RCS cut of SES5 for multiple frequencies around the design value of 60GHz.

For SES5, as frequency increases from 58GHz to 62GHz, the main lobe slightly grows in amplitude instead of decreasing, while side lobes become nearly comparable to the main lobe. Additionally, the main lobe direction shifts with frequency. Combined with the already significant specular component, this behaviour indicates that the energy distribution is strongly influenced by the reflection angle, leading to less efficient beam focusing and more pronounced scattering.

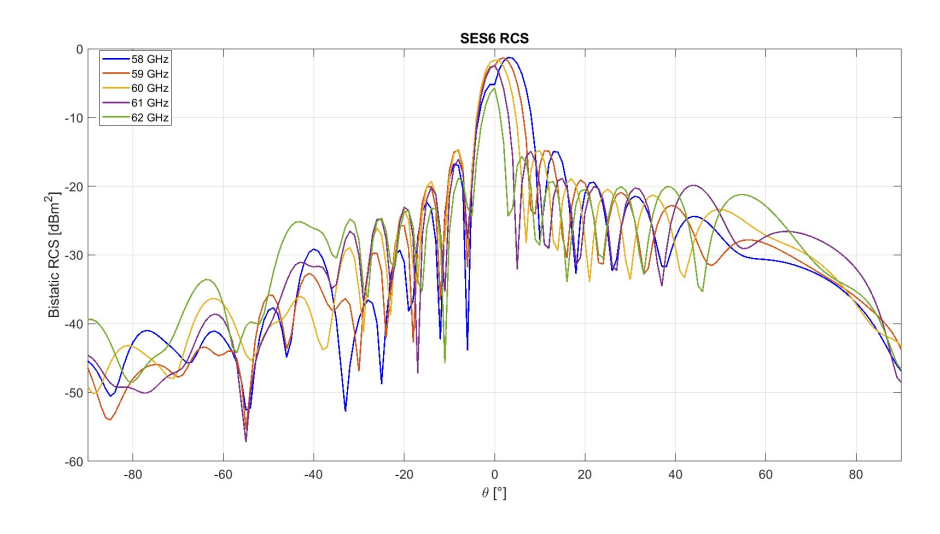


Figure 4.3.6: RCS cut of SES6 for multiple frequencies around the design value of 60GHz.

SES6 behaves similarly to SES1: at lower frequencies (58–59GHz) the main lobe slightly deviates from the target direction, while at higher frequencies (61–62GHz)

it aligns with the intended direction but gradually decreases in amplitude. Side lobes grow more pronounced, and the specular reflection increases significantly.

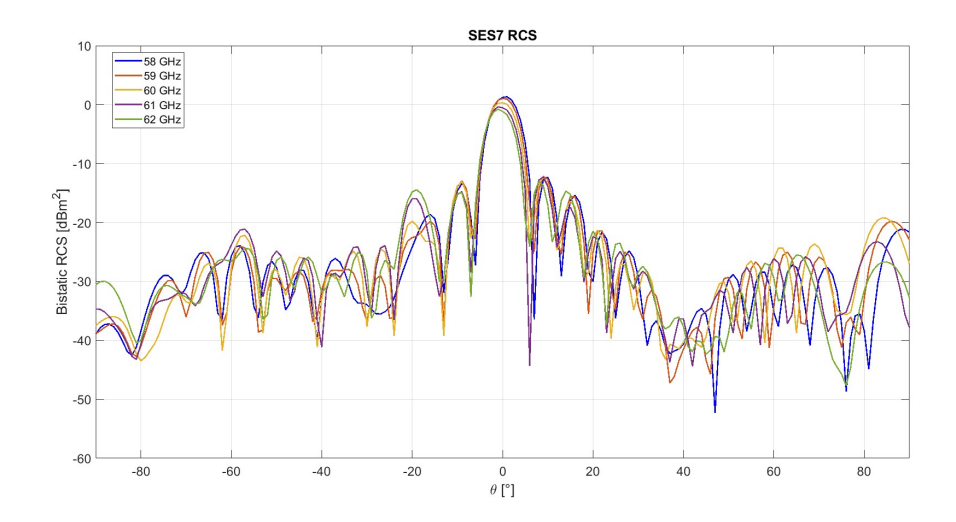


Figure 4.3.7: RCS cut of SES7 for multiple frequencies around the design value of 60GHz.

SES7 shows minimal main lobe reduction across the frequency range, with side lobes remaining nearly constant. The main lobe direction is stable, indicating an essentially robust response from 58GHz to 62GHz.

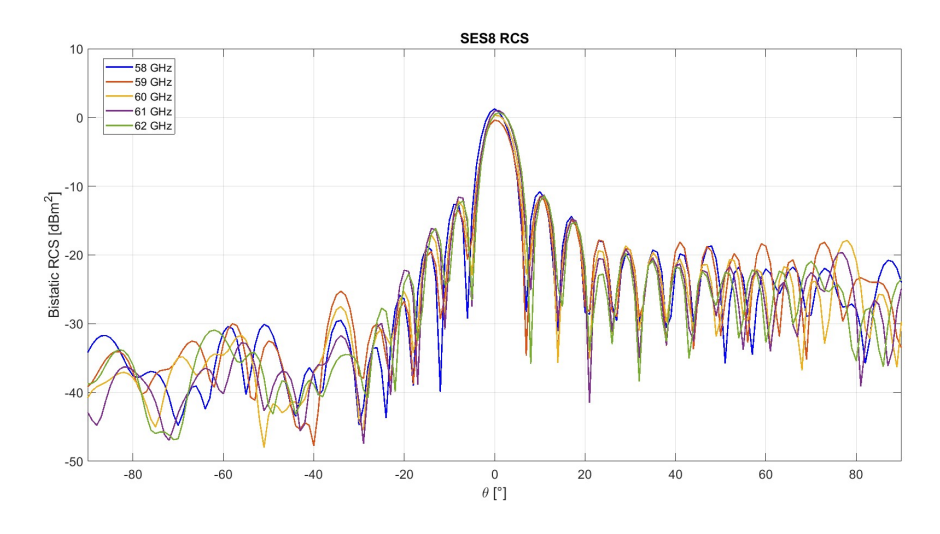


Figure 4.3.8: RCS cut of SES8 for multiple frequencies around the design value of 60GHz.

SES8 behaves similarly to SES7: the main lobe amplitude changes very little, side lobes remain nearly constant, and the main lobe pointing direction is stable, showing

a robust response across the analysed frequency range.

4.4 Conclusions of the SESs Analysis

In summary, the analysis of the eight SESs within the realistic indoor scenario shows that the designed surfaces can effectively steer incident plane waves toward the desired directions. The far-field simulations confirm that the main lobes are generally well aligned with the target angles, while the side lobes remain sufficiently low, ensuring a clear distinction of the beams, with only minor specular reflections observed.

The layout of the patch distributions has proven effective in translating the phase profiles into physical structures, minimizing unwanted scattering and maintaining predictable radiation behaviour. Differences in performance, such as slightly lower main lobe levels or stronger specular components, are mainly due to extreme steering angles or the truncation of the phase curves, highlighting the limitations due to the small size of the arrays.

Finally, comparing different SES placements in the indoor environment shows that careful positioning, such as the W-shaped configuration, can significantly reduce intersurface interference, improving the overall efficiency of wave redirection and supporting both communication and passive localization functionalities. These results provide a solid foundation for further studies on deploying multiple SESs in complex propagation scenarios.

Chapter 5

Conclusions

This thesis has investigated the design, analysis, and simulation of smart electromagnetic skins for applications at 60 GHz in indoor communication and localization scenarios. After introducing the concept of the smart electromagnetic environment and highlighting the potential of SESs, a systematic approach was developed, starting from the characterization of the unit cell up to the validation of complete surfaces integrated into realistic environments.

The design of the unit cell, based on square patch elements, enabled the analysis of different dielectric substrates and the identification of the most suitable materials to ensure a wide phase range and low losses at mmWave frequencies. Based on this characterization, a procedure for mapping the desired phase distribution into patch geometries was established and applied to realize several SESs configurations. The comparison between arrays of different sizes highlighted the critical role of aperture dimensions in achieving high directivity and reflection efficiency.

The integration of SESs into a realistic indoor scenario confirmed their ability to mitigate the limitations of mmWave propagation. The results also demonstrated the strong dependence of system performance on the placement and orientation of the surfaces, suggesting effective deployment strategies to simultaneously support communication and localization functionalities.

In summary, the main contributions of this work can be outlined as follows:

• Development and validation of a design methodology for passive SESs at 60 GHz.

- Comparison of different dielectric substrates.
- Demonstration, through full-wave simulations, of the SES capability to enhance coverage and improve signal reliability;
- Evaluation of deployment strategies to minimize undesired scattering and mutual interference among multiple surfaces.

Although the results are promising, some limitations remain. The study focused on passive surfaces, whose finite size can create unwanted lobes and reduce efficiency, especially at extreme reflection angles. Still, the numerical simulations highlighted important directions for future work. Moving forward, it would be useful to carry out full-wave simulations in realistic environments, for example using HFSS, and eventually validate the designs with real-world measurements, bridging the gap between theory and practice.

Appendix A

MATLAB Code for SES Design

This appendix reports the MATLAB scripts developed to support the design of the Smart Electromagnetic Skin. The code allows the extraction of the reflection phase curves from CST Studio Suite simulations, processes the data to evaluate the required phase shift for each unit cell, and calculates the corresponding patch width through interpolation. These scripts provide a systematic and automated approach to map the desired phase distribution onto the physical dimensions of the SES elements, enabling accurate and efficient design of the complete surface.

```
clear all
close all
clc

%% LOAD DATA
data = readtable('FILENAME.txt'); % file containing phase
    values for different theta, thickness, w

w = data.w; % extract the 'w' column
theta = data.theta; % extract the 'theta' column
thickness = data.thickness; % extract the 'thickness' column
phase = data.Value; % extract the 'Value' column (phase)
phi = data.phi; % extract the 'phi' column
```

```
14 % Target values
thickness_target = 0.51; % desired thickness
16 theta_target = 0;
                         % desired theta
17 phi_target =0;
                           % desired phi
18
19 % Filter data for desired thickness and theta
20 dx = (thickness == thickness_target) & (theta == theta_target)
    & (phi == phi_target);
21
 w_{plot} = w(idx);
                        % select 'w' values corresponding to the
22
     filter
phase_plot = phase(idx); % select phase values corresponding to
     the filter
24
25 % Phase unwrapping
phase_unwrap_rad = unwrap(deg2rad(phase_plot)); % unwrap phase
    in radians
 unwrapped phase back to degrees
28
 % Interpolation function
interp_fun = @(phi) interp1(phase_unwrap_deg, w_plot, phi, '
    nearest', 'extrap');
_{31} | % creates a function to map phase to corresponding 'w' value
    using nearest neighbor interpolation
32
33 % Plot filtered phase curve
34 figure;
plot(w_plot, phase_unwrap_deg, 'b-', 'LineWidth', 2); % plot
    phase vs w
xlabel('Phase [deg]');
                                                       % label x
    -axis
```

```
ylabel('w [mm]');
                                                          % label y-
     axis
ss title(['Rogers ro3003 @60GHz \theta = ' num2str(theta_target) '
     deg, thickness = ' num2str(thickness_target) ' mm']);
39 % set the title with target theta and thickness
40 grid on;
                                                           % enable
     grid
 %% ARRAY PARAMETERS
4.3
                             % number of elements per side
_{44}|N = 10;
_{45} f = 60e9;
                             % operating frequency in Hz
_{46} c = 3e8;
                             % speed of light in m/s
|a_7| lambda = c/f:
                             % wavelength
d = 0.5 * lambda;
                             % element spacing
_{49} k0 = 2*pi/lambda;
                             % wave number
50
|x| = ((1:N) - (N+1)/2) * d; % x coordinates centered around 0
_{52}|y = x;
                              % y coordinates (same as x)
 [X, Y] = meshgrid(x, y); % create 2D grid of element positions
55 % Arrival and beam angles
theta_i = deg2rad(0); % incident azimuth in radians
                             % incident elevation in radians
57 phi_i = deg2rad(0);
58 theta_b = deg2rad(30);
                             % beam azimuth in radians
  phi_b = deg2rad(0);  % beam elevation in radians
60
61 % Required phase
phi_R = -k0 * ( X*(sin(theta_b)*cos(phi_b) + sin(theta_i)*cos(
     phi_i)) ...
63 + Y*(sin(theta_b)*sin(phi_b) + sin(theta_i)*sin(phi_i)) );
_{64}| % computes the required phase at each element for beam steering
```

```
65
66 phi_R_deg = mod(rad2deg(phi_R), 360) - 360;
_{67} | % convert phase to degrees and wrap between -360 and 0
69 % Plot required phase
70 figure;
71 imagesc(phi_R_deg);
                                       % display phase distribution
     as image
72 cb = colorbar;
                                       % add colorbar
cb.Label.String = 'Required phase shift [deg]'; % label colorbar
74 caxis([-360 0]);
                                       % set color axis limits
title('Required Phase Shift Distribution'); % set title
76
77 %% W MAP
78
v_map = interp_fun(phi_R_deg);
80 % plot required w
81 figure;
82 imagesc(1:N, 1:N, w_map);
83 axis equal tight;
84 colorbar;
85 title('W distribution');
86 xlabel('x index'); ylabel('y index');
```

Appendix B

Generation of DXF file

```
_{2}|% Script for exporting the patch width distribution to CST
3 % by generating a DXF file representing the SES layout.
 6 % Name of the DXF file to be generated
 tmpScriptFile = 'FILENAME.dxf';
9 % Define the cell spacing (converted to millimeters)
dx = d*1e3; % Element spacing along x-direction [mm]
dy = d*1e3; % Element spacing along y-direction [mm]
12
13 % Create a new temporary CST script file
14 fid = fopen(tmpScriptFile, 'wt');
16 % Matrix containing the patch width distribution
|W_m| = (w_map);
18 [Nx, Ny] = size(W_mn); % Number of elements along x and y
20 % Write DXF header
dxfHeader(fid);
22
```

```
23 % Loop over the array elements to generate the geometry
24 | for i = 1:Nx
     for j = 1:Ny
 % Compute coordinates of the element center
          X = (i - 1/2 - Ny/2) * dy; % Center position along y-
27
             axis
          Y = (j - 1/2 - Nx/2) * dx; % Center position along x-
28
             axis
29
 % Retrieve the patch width from the distribution matrix
          W = W_mn(j,i);
                                         % Patch width [mm]
31
 % Draw a square patch with side length W at position (Y, X)
          dxfRectangle(fid, [Y, X], W, W);
34
      end
35
 end
37
38 % Close DXF file
39 dxfClose(fid);
```

B.1 Function dxfRectangle

```
X1 = Center(1) - Width/2;
12 \times 2 = Center(1) + Width/2;
13
14 Y1 = Center(2) + Height/2;
Y2 = Center(2) - Height/2;
1.6
17
18 fprintf(fid, '0\n');
19 fprintf(fid, 'SOLID\n');
20 % Write vertex (X1,Y1)
21 fprintf(fid, '10\n');
22 fprintf(fid, '%f\n', X1);
fprintf(fid, '20\n');
fprintf(fid, '%f\n', Y1);
25
26 % Write vertex (X1,Y2)
27 fprintf(fid, '11\n');
fprintf(fid, '%f\n', X1);
29 fprintf(fid, '21\n');
30 fprintf(fid, '%f\n', Y2);
32 % Write vertex (X2,Y1)
fprintf(fid, '12\n');
34 fprintf(fid, '%f\n', X2);
35 fprintf(fid, '22\n');
36 fprintf(fid, '%f\n',Y1);
37
38 % Write vertex (X2,Y2)
39 fprintf(fid, '13\n');
40 fprintf (fid, '%f\n', X2);
41 fprintf(fid, '23\n');
42 fprintf(fid, '%f\n', Y2);
```

B.2 Function dxfHeader

B.3 Function dxfClose

Bibliography

- [1] https://www.theengineer.co.uk/content/news/intelligent-surfaces-development-could-solve-indoor-positioning-problem/
- [2] M. Salucci et al., "The Smart EM Environment Paradigm From the Idea Towards the Implementation," 2023 17th European Conference on Antennas and Propagation (EuCAP), Florence, Italy, 2023, pp. 1-4
- [3] M. Di Renzo, M. Debbah, D.-T. Phan-Huy, A. Zappone, M.-S. Alouini, C. Yuen, V. Sciancalepore, G. C. Alexandropoulos, J. Hoydis, H. Gacanin, J. de Rosny, A. Bounceur, G. Lerosey, and M. Fink, "Smart radio environments empowered by reconfigurable AI meta-surfaces: An idea whose time has come," EURASIP J. Wireless Commun. Netw., vol. 2019, p. 129, May 2019.
- [4] R. Flamini et al., "Toward a Heterogeneous Smart Electromagnetic Environment for Millimeter-Wave Communications: An Industrial Viewpoint," in IEEE Transactions on Antennas and Propagation, vol. 70, no. 10, pp. 8898-8910, Oct. 2022
- [5] D. Erricolo, A. Rozhkova and A.C. Stutts, "Towards Smart Electromagnetic Environments," Proc. 2021 Computing, Communications, and IoT Applications (Com-ComAp), Shenzhen, China, 2021.
- [6] G. Oliveri, et al., "Building a Smart EM Environment AI-Enhanced Aperiodic Micro-Scale Design of Passive EM Skins," IEEE Trans. Antennas Propag., vol. 70, pp. 8757–8770, 2022.

- [7] Y. Zhu et al., "A Varactor-Based Reconfigurable Intelligent Surface Concept for 5G/6G mm-Wave Applications," 2024 18th European Conference on Antennas and Propagation (EuCAP), Glasgow, United Kingdom, 2024, pp. 1-5.
- [8] Y. Youn et al., "Liquid-Crystal-Driven Reconfigurable Intelligent Surface With Cognitive Sensors for Self-Sustainable Operation," in IEEE Transactions on Antennas and Propagation, vol. 71, no. 12, pp. 9415-9423, Dec. 2023
- [9] I. Marasco, C. Cantore, G. V. Bianco, G. Bruno, A. D'Orazio and G. Magno, "Transparent Graphene-Based RIS for 6G Communications in the THz Spectrum," in IEEE Open Journal of Antennas and Propagation, vol. 6, no. 1, pp. 193-200, Feb. 2025
- [10] Singh K, Saikia M, Thiyagarajan K, Thalakotuna D, Esselle K, Kodagoda S. Multi-Functional Reconfigurable Intelligent Surfaces for Enhanced Sensing and Communication. Sensors (Basel). 2023 Oct 18
- [11] J. Rains, et al., "High-resolution programmable scattering for wireless coverage enhancement: An indoor field trial campaign," arXiv:2112.11194, 2021.
- [12] A. Benoni, M. Salucci, G. Oliveri, P. Rocca, B. Li and A. Massa, "Planning of EM Skins for Improved Quality-of-Service in Urban Areas," in IEEE Transactions on Antennas and Propagation, vol. 70, no. 10, pp. 8849-8862, Oct. 2022.
- [13] Beccaria, M., Freni, A., Mazzinghi, A., Pirinoli, P., On the features of curved, passive reconfigurable smart electromagnetic skins. Sci Rep 15, 32277 (2025).
- [14] X. Tan, Z. Sun, D. Koutsonikolas, and J. M. Jornet, "Enabling indoor mobile millimeter-wave networks based on smart reflect-arrays," in Proc. IEEE Conf. Comput. Commun. (INFOCOM), Honolulu, HI, USA, Apr. 2018, pp. 270–278
- [15] E. Basar, M. Di Renzo, J. De Rosny, M. Debbah, M. -S. Alouini and R. Zhang, "Wireless Communications Through Reconfigurable Intelligent Surfaces," in IEEE Access, vol. 7, pp. 116753-116773, 2019

- [16] Á. F. Vaquero, E. Martinez-de-Rioja, M. Arrebola, J. A. Encinar and M. Achour, "Smart Electromagnetic Skin to Enhance Near-Field Coverage in mm-Wave 5G Indoor Scenarios," in IEEE Transactions on Antennas and Propagation, vol. 72, no. 5, pp. 4311-4326, May 2024
- [17] G. Marchi, J. Iannacci, V. Mulloni, A. Bagolini and L. Lorenzelli, "High-Resolution Fabrication Procedure for an Optically-Transparent Modular Smart Electromagnetic Skin," 2025 IEEE Wireless Communications and Networking Conference (WCNC), Milan, Italy, 2025, pp. 1-6.
- [18] A. Benoni, F. Capra, M. Salucci, A. Massa, "Toward Real-World Indoor Smart Electromagnetic Environments—A Large-Scale Experimental Demonstration," *IEEE Transactions on Antennas and Propagation*, vol. 71, no. 11, pp. 8450-8463, Nov. 2023.
- [19] G. Oliveri, M. Salucci and A. Massa, "Features and Potentialities of Static Passive EM Skins for NLOS Specular Wireless Links," in IEEE Transactions on Antennas and Propagation, vol. 71, no. 10, pp. 8048-8060, Oct. 2023.
- [20] G. Encinas-Lago, F. Devoti, M. Rossanese, V. Sciancalepore, M. D. Renzo and X. Costa-Pérez, "COLoRIS: Localization-Agnostic Smart Surfaces Enabling Opportunistic ISAC in 6G Networks," in IEEE Transactions on Mobile Computing, vol. 24, no. 8, pp. 6812-6826, Aug. 2025
- [21] A. Benoni, M. Salucci, G. Oliveri, P. Rocca, B. Li, and A. Massa, "Plan ning of EM skins for improved quality-of-service in urban areas," IEEE Trans. Antennas Propag., vol. 70, no. 10, pp. 8849–8862.
- [22] J. Huang and J. A. Encinar, Reflectarray Antennas. Hoboken, NJ, USA: Wiley-Interscience, 2008.
- [23] Ismail, M., Kiyani, A., (2014). Characterization of Printed Reflectarray Elements on Variable Substrate Thicknesses. International Journal of Electrical, Electronic Science and Engineering. 8. 1-5.

- [24] Sanaâ Finich, Naima Amar Touhami, Abdelkrim Farkhsi, Design and Analysis of Different Shapes for Unit-Cell Reflectarray Antenna, Procedia Engineering, Volume 181,2017, Pages 526-530,
- [25] Rogers Corporation. RO3000 Series Circuit Materials Datasheet. [Online]. Available: https://www.rogerscorp.com/documents/ 722/acs/RO3000-Laminate-Data-Sheet-RO3003-RO3006-RO3010.pdf
- [26] J. Kornprobst, K. Wang, G. Hamberger and T. F. Eibert, "A mm-Wave Patch Antenna with Broad Bandwidth and a Wide Angular Range," in IEEE Transactions on Antennas and Propagation, vol. 65, no. 8, pp. 4293-4298, Aug. 2017.
- [27] Chia, Tse Tong. (2016). Prediction of Electromagnetic Scattering from Metasurfaces.
- [28] M. Beccaria, D. Scazzoli, M. Magarini and P. Pirinoli, "Smart Skins in SREs: Improving Communication and Localization Performance," 2025 URSI International Symposium on Electromagnetic Theory (EMTS), Bologna, Italy, 2025, pp. 1-3